Revealing the Role of IGFN1 in Skeletal Muscle

Tobias Cracknell

PhD

University of York

Biology

September 2019

Abstract

The role of the skeletal muscle protein Immunoglobulin-like and fibronectin type III domain containing 1 (IGFN1) has proved elusive. There are several IGFN1 isoforms, none of which contain catalytic domains. Each isoform has a domain composition of immunoglobulin and fibronectin domains, suggesting a structural role in the sarcomere. IGFN1 was first discovered as an interacting partner of the disease-associated protein KY, and the current literature implicates IGFN1 in both atrophy and myoblast fusion.

Here, characterisation of fusion and differentiation indexes. compared to wildtype, of a CRISPR/Cas9-generated, C2C12-derived, IGFN1 knockout cell line revealed fusion and differentiation defects. Furthermore, these cells display increased globular to filamentous actin ratios, indicating decreased actin polymerisation which potentially underlies the fusion defects observed. Crucially, the above phenotypes are ameliorated through expression of the IGF1_V1 isoform.

Next, to identify IGFN1 interaction partners, IGFN1 fragments were purified and pull-down analysis was performed revealing the actin nucleator COBL as a potential interacting partner. This interaction subsequently validated through immunoprecipitation and colocalization. The role of COBL in myoblast fusion was investigated through overexpression experiments and the generation of a C2C12-derived knockout cell line. Initial characterisation points towards a role for COBL in myoblast fusion. Taken together, it is possible that IGFN1 influences actin remodelling, and therefore myoblast fusion, through its interaction with COBL.

Table of contents

List of Figures and Tables

Acknowledgements

Declaration

I declare that this thesis is a presentation of original work and I am the sole author unless explicitly highlighted in the text. Examples include parts of figures adapted for use in this text, all of which are with the authors permission or under a Creative Commons licence and outlined in the respective figure legend. Additionally, LC-MS/MS was performed by Adam Dowle (University of York Biology Technology Facility), as described in the text.

This work has not previously been presented for an award at this, or any other, University. All sources are acknowledged as References.

Chapter 1:

Introduction

Chapter 1: Introduction

1.1 Overview

Skeletal muscle comprises 30-40% of total body mass in humans, making it the largest organ system by mass in the body. The primary role of skeletal muscle is the conversion of chemical energy into mechanical energy. The hydrolysis of ATP provides the energy for contractions which produce movement or maintain posture. Alongside this, skeletal muscle tissue acts as a reservoir for amino acid storage, as well as helping to maintain body temperature due to its high metabolic activity. There is also evidence that skeletal muscle acts as a secretory organ, releasing so-called myokines which act in an autocrine/paracrine way on the muscle tissue itself, or in an endocrine manner, facilitating communication between the muscle and other organs (for a review see (Pedersen, 2013)).

Skeletal muscle is a highly plastic tissue, able to respond to the physiological challenges placed on it, and the body as a whole. Physical activity such as running and climbing, or in the modern world resistance training in the gym, stimulate an increase in skeletal muscle mass. Skeletal muscle growth allows the organism to adapt to its environment, providing a survival advantage as it will be able to better respond to the challenges placed upon it in the future. During starvation however, muscle mass falls. Amino acids stored in the muscle tissue are released to help maintain blood glucose levels through gluconeogenesis, or processed into ketones. Muscle mass loss also helps to reduce the metabolic requirements of an organism during scarcity. The processes of increasing and decreasing muscle mass are controlled by several complex and interconnected pathways, which under normal physiological conditions are balanced to maintain a constant muscle mass.

In the modern developed world starvation is no longer a major issue in society. However, inactivity, an aging population, and the atrophy induced by many disease states mean that muscle wasting is an increasing concern. Loss of muscle mass is common during ageing (sarcopenia). Sarcopenia increases the risk of all-cause mortality (Liu et al., 2017) and leads to a reduction in quality of life (Tsekoura et al., 2017), as people become less able to perform

everyday tasks. Muscle wasting is also observed in many disease states including cancer and AIDS (cachexia), where it is a positive indicator of the chance of death from the underlying disease (Bourdel-Marchasson et al., 2016). While exercise and nutritional interventions are often successful in preserving, and even increasing muscle mass and function (Evans, 1999), these interventions are not always appropriate for all patients. High protein diets are not appropriate for some patients with chronic kidney disease (Ko et al., 2017), and exercise may not be possible in the time immediately post-surgery or for critically ill patients. Understanding the processes involved in muscle mass maintenance may help to develop novel therapies to improve the lives of those suffering with sarcopenia and cachexia.

Muscle wasting diseases can also have a genetic cause, with mutations in genes directly involved with muscle function. These congenital myopathies are characterised by a poor quality of life due to muscle weakness, which becomes progressively more severe and often results in early death (for a review see (Ravenscroft et al., 2018)). The most common group of congenital myopathies are muscular dystrophies, with Duchenne muscular dystrophy (DMD) being the most common of these. DMD is caused by a mutation in the gene coding for the dystrophin protein, which is responsible for anchoring the contractile machinery of the sarcomere to the costameres (Hoffman et al., 1987). However, the underlying genetic causes and pathogenic mechanisms of many muscular dystrophies and other myopathies are less well understood, making the understanding of the structure and function of skeletal muscle all the more pertinent.

The *ky/ky* mutant mouse is a model of kyphoscoliosis, characterised by an inability to respond to mechanical load with hypertrophy, with postural muscles in particular showing pathological hallmarks (Blanco et al., 2001). Examples of human myopathies associated with KY deficiency have recently come to light (Hedberg-Oldfors et al., 2016; Straussberg et al., 2016; Yogev et al., 2017), emphasising the importance of the KY protein in muscle mass maintenance. While there is evidence that KY may play a role in protein turnover through Chaperone Assisted Selective Autophagy (CASA) (Beatham

et al., 2004a; Jokl et al., 2018), no definitive role for KY in skeletal muscle has been established.

Immunoglobulin-like and fibronectin type III domain containing 1 (IGFN1) was identified as an interacting partner of KY at the z-disc (Baker et al., 2010). The domain composition of IGFN1 consists of immunoglobulin and fibronectin-like domains, similar to that of sarcomeric proteins involved in maintaining the structural integrity of the muscle fibre. While there is evidence implicating IGFN1 in both atrophy (Chen et al., 2014; Mansilla et al., 2008; Rahimov et al., 2011), and myoblast fusion (Li et al., 2017), the function of IGFN1 has proved elusive and may be crucial to understanding the role of the disease-associated KY protein. This research presented in this thesis was performed with the goal of interrogating the functional role of IGFN1 in skeletal muscle through the use of a CRISPR/Cas9 generated IGFN1 knockout C2C12-derived cell line and the identification and validation of IGFN1 interaction partners.

1.2 Skeletal Muscle Structure and Contraction
1.2.1 Skeletal Muscle Structure
A single skeletal muscle is comprised of bundles of muscle fibres, known as fascicles (fig.1.1). Each muscle fibre is made up of a bundle of myofibrils running in parallel with one another. An individual fascicle is surrounded by the perimysium, a layer of connective tissue which acts to provide structural integrity to the tissue. These fascicles are encased in a further layer of connective tissue, the epimysium, which provides a further degree of structural integrity. Tendons connect muscles to the bone, typically at both sides of a joint, allowing for the transmission of the contractile force of the muscle to the joint, resulting in movement. Muscle tissue is heavily innervated by motor neurons which trigger these contractions, and an abundant supply of blood vessels sustain its high metabolic activity.

Muscle fibres are post-mitotic and multinucleated, formed through the fusion of numerous myoblasts. The traditional theory is one of a single myonucleus

controlling the protein production of a defined region, or nuclear domain (Pavlath et al., 1989). This seems to happen in a coordinated manner so that similar proteins are produced throughout the muscle fibre. However, non-uniformity of protein expression across a muscle fibre has been reported (Wilkins et al., 2001), with myonuclei at the neuromuscular and myotendinous junctions expressing subsets of genes relevant to the specialized regions (Merlie and Sanes, 1985).

Because muscle fibres are post-mitotic, muscle stem cells, otherwise known as satellite cells, are required in the event of injury to regenerate the damaged tissue, or to contribute to muscle growth by providing additional myonuclei. Satellite cells are found under the basal lamina of the muscle fibre, and are able to self-renew and contribute to muscle regeneration by fusing with damaged fibres (for a review see (Morgan and Partridge, 2003)). It is thought that satellite cells are required once the upper size limit of the myonuclear domains of the existing myonuclei is reached during muscle fibre growth. However, this paradigm has been brought into question, with highly flexible myonuclear domains, and hypertrophy independent of satellite cell fusion observed (for a review see ((Murach et al., 2018)).
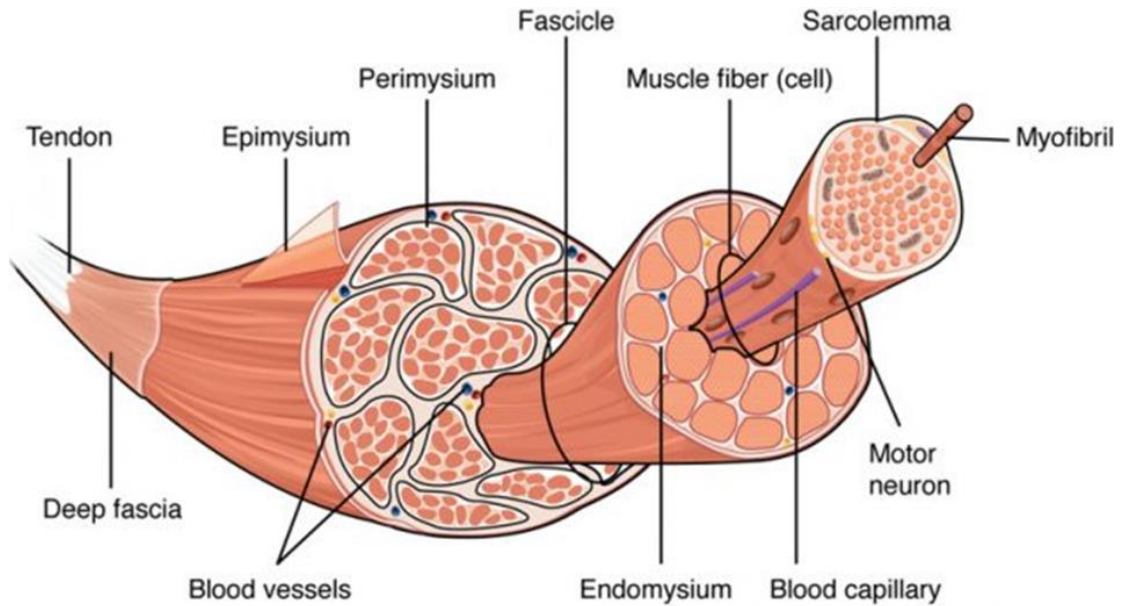
Figure 1.1. Skeletal muscle structure. *Whole tissue to myofibril, showing a nested set of bundles. Muscle fibres formed by a bundle of myofibrils, followed by fascicles formed by a bundle of muscle fibres which make up the muscle belly encased in the epimysium. Image taken from* http://library.open.oregonstate.edu/aandp/chapter/10-2-skeletal-muscle/*.*

1.2.2 Skeletal Muscle Contraction

The individual contractile units of the muscle fibre are the sarcomeres, which are organised end on end to form a myofibril. The sarcomere consists of actin thin filaments anchored to the z-disc and myosin thick filaments anchored to the M-line, which marks the centre of the sarcomere (fig. 1.2). Actin and myosin filaments overlap at the A band where they mediate muscle contraction by pulling against one-another in a cross bridge cycle, thereby shortening the length of the sarcomere and the muscle itself (Huxley, 1957).

This process is reliant on ATP, myosin heads detach from actin upon the binding of ATP. ATP is then hydrolysed, providing the energy for the myosin head to move and bind to the next actin molecule and perform a power stroke, pulling the actin filaments towards the M-line. An influx of Ca^{2+} ions caused by

an action potential, initiated by a motor neuron at the neuromuscular junction, is required for this process to occur. Tropomyosin masks the myosin binding sites of actin at rest. Upon Ca^{2+} ion influx troponin displaces tropomyosin, allowing myosin heads to bind to the actin filaments (Parry and Squire, 1973).

1.2.3 Muscle Fibre Type

The myosin thick filament is made up of a myosin heavy chain (MYHC), a myosin light chain (MYLC), and myosin binding protein C (MYBC). Different isoforms of MYHC are expressed in different muscle fibre types, in accordance with the physical demands placed on the muscle. Type I "slow twitch" muscle fibres are oxidative and produce sustained slow contractions and are often involved in maintaining posture. Type IIb "fast twitch" muscle fibres are glycolytic and produce short, powerful contractions required for dynamic movement. Type IIa muscle fibres are intermediate muscle fibres which display features of both fast and slow muscle fibre types.
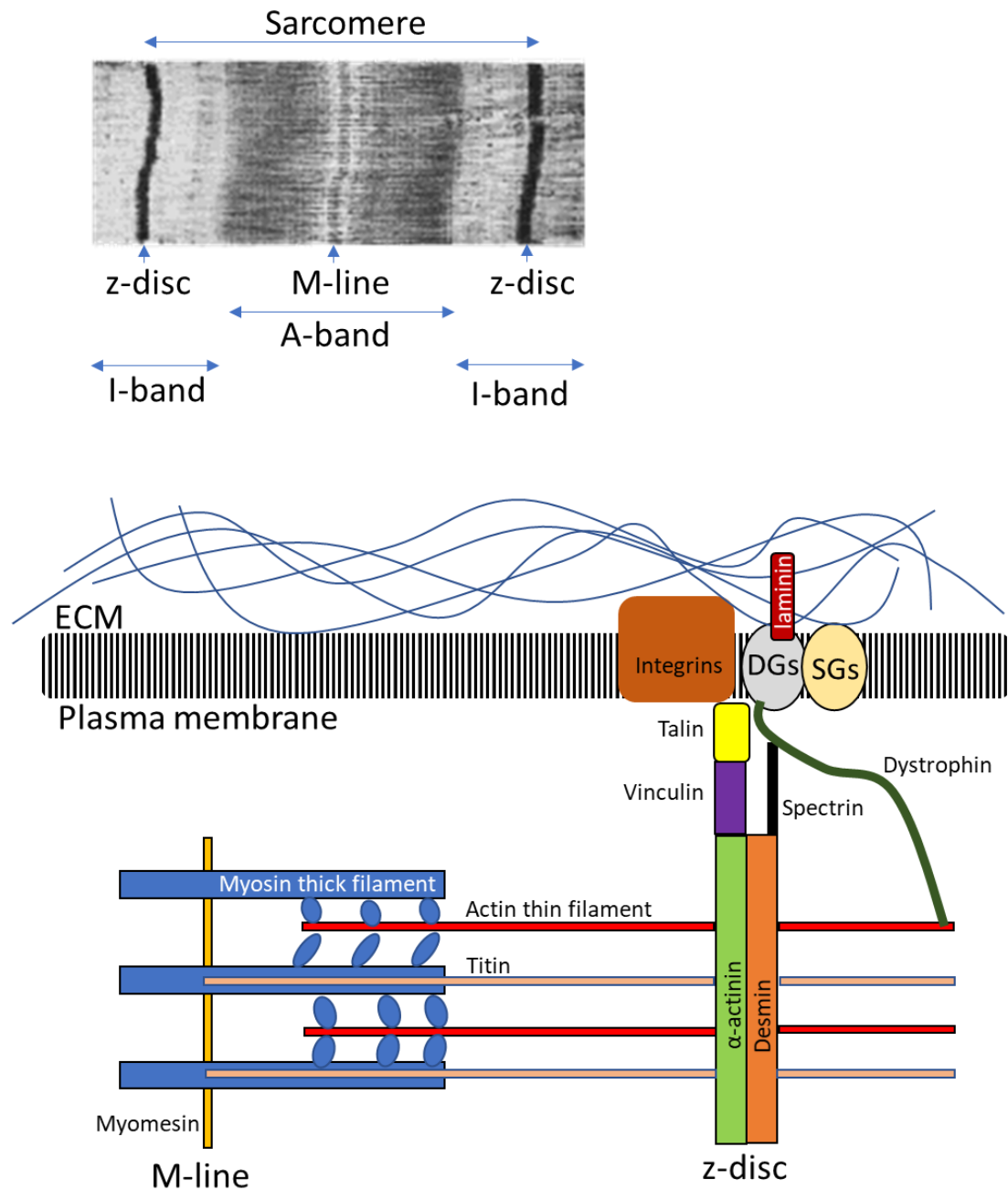
Figure 1.2 Sarcomeric Structure. *Top: electron microscopy image of the sarcomere with significant regions labelled. Adapted from https://commons.wikimedia.org/wiki/File:Sarcomere.gif reproduced under a creative commons licence. Bottom: Schematic of the sarcomere with key structural components from the M-line to z-disc shown. Myomesin crosslinks myosin thick filaments at the M-line, while α-actinin crosslinks actin at the z-disc. Titin spans the length of the M-line to the z-disc. Dystrophin provides stability and a signalling function between the z-disc and the costamere via dystroglycans (DGs) and sarcoglycans (SGs).*

1.2.4 Sarcomeric Structural Proteins

The structural integrity of the sarcomere is maintained by a complex network of crosslinking proteins, which anchor the contractile apparatus in place (fig. 1.2). Titin is the largest protein in the human body, consisting of hundreds of immunoglobulin and fibronectin domains. It spans the sarcomere form the z-disc to the M-line and performs numerous functions, providing a scaffold for many other structural proteins to bind to (for a review see (Tskhovrebova and Trinick, 2003)). Nebulin is another giant muscle protein, known to help regulate the length of actin filaments by acting as a molecular ruler (Bang et al., 2006; Witt et al., 2006). However, how nebulin regulates actin filament length is clearly not the sole function of the protein, with links to sarcoplasmic Ca^{2+} handling and myofibrillar force generation (Chu et al., 2016).

It is increasingly clear that many proteins assumed to perform only structural or scaffolding roles may be responsible for more complex cellular processes, such as mechanosensing and signalling. Titin is known to provide structural integrity to the sarcomere as it contracts and relaxes. Atomic force microscopy (AFM) has demonstrated that the immunoglobulin domains of titin are able to unfold and refold in response to mechanical tension, allowing it to act as a mechanical spring to absorb contractile forces (Rief et al., 1997). In addition, there is evidence that titin may play role in mechanotransduction, potentially as a mechanosensor, due to its elastic properties (Gautel, 2011; Kruger and Kotter, 2016; van der Pijl et al., 2018).

α-actinin is a z-disc protein which forms antiparallel homodimers which interact with the n-terminus of titin (Atkinson et al., 2001), and is responsible for crosslinking actin filaments at the z-disc. In addition to this structural role, α-actinin is known to interact with a number of proteins implicated in mechanical strain sensing. One such protein is actinin-binding muscle LIM protein CSRP3/MLP, believed to be a mechanosensing protein (Boateng et al., 2009). At the M-band another titin binding partner, myomesin, is responsible for the crosslinking of myosin. Like α-actinin myomesin forms antiparallel dimers which interact with the c-terminal end of titin (Lange et al., 2005). Interestingly, as with titin, the immunoglobulin domains of myomesin have been shown to

act as mechanical springs, able to absorb the contractile forces placed upon the M-band and maintain its structural integrity (Schoenauer et al., 2005).

Integration of the structural components of the muscle fibre to the extracellular matrix (ECM) is another mechanism of maintaining sarcomeric structure. The Z-disc is anchored to the ECM through the costamere, made up of a protein complex including dystrophin and desmin, which are bound to integrins within the cell membrane. These integrins are connected to ECM components including collagen and proteoglycans. Mutations in costameric proteins often result in severe myopathies, and in the case of dystrophin, Duchenne muscular dystrophy (Hoffman et al., 1987).

1.2.5 The C2C12 Cell Line as a Model for Skeletal Muscle *in vitro*

The C2C12 cells line is a mouse myoblast cell line, a subclone of a line originally isolated from the leg muscle of an adult mouse (Blau et al., 1983; Yaffe and Saxel, 1977). It proliferates in high serum media (typically ~10% serum), and upon transfer to low serum media (typically ~2% serum) differentiation is initiated. C2C12 myoblasts form myocytes and multinucleated myotubes upon fusion. Further differentiation of these cells results in the formation of striations, reflecting the contractile machinery observed *in vivo.* Under ideal conditions contraction can be observed in C2C12 cells differentiated for long periods of time. These properties make C2C12 cells a valuable model for skeletal muscle *in vitro,* particularly when studying myoblast fusion and differentiation.

1.3 Myoblast Fusion

Myoblast fusion allows for the formation of multinucleated muscle fibres during development, as well as satellite cell fusion in response to growth signals or muscle damage. It is a process underpinned by remodelling of the cytoskeleton throughout each stage: migration, recognition, adhesion, membrane alignment, and membrane pore formation and resolution (Rochlin et al., 2010). Much of the early evidence regarding myoblast fusion came from

Drosophila, however many of the genes identified have vertebrate orthologues. A summary of the myoblast fusion machinery in *Drosophila* and in mammals can be seen in figure 1.3.

1.3.1 Myoblast Fusion in *Drosophila*

Cytoskeletal changes are crucial for proper cell migration. During myoblast migration in *Drosophila;* Kette, a conserved member of the SCAR/WAVE regulatory complex (Gildor et al., 2009), regulates the actin nucleator Arp2/3 (Ibarra et al., 2005) to drive the migration of a fusion competent myoblast (FCM) to a founder cell (FC). This is followed be recognition of the FC and adhesion. Immunoglobulin super family (IgSF) members Dumbfounded (Duf) and Roughest (Rst) are expressed in the FC. While Sticks and Stones (Sns) and Hibris (Hbs) are expressed in the FCM. The interaction between Duf and Sns, and Rst and Hbs is required for cell recognition and adhesion of the FC and the FCM. (Artero et al., 2001; Bour et al., 2000; Dworak et al., 2001; Ruiz-Gomez et al., 2000; Strunkelnberg et al., 2001).

Upon the adhesion of fusing cells, an actin "focus" is formed in the FCM and a thin actin "sheath" forms in the FC. Without the formation and dissolution of these structures, fusion cannot proceed (Kesper et al., 2007; Kim et al., 2007; Richardson et al., 2007). The formation of this actin focus is dependent on the Kette-SCAR-Arp2/3 pathway. It is thought that the actin focus provides a positional cue for membrane targeting of vesicles required at the onset of pore formation (Rochlin et al., 2010). Again Arp2/3 is implicated in the expansion of these pores, with actin providing a force generating mechanism (Berger et al., 2008). Pore expansion allows the nucleus of the FCM to enter the FC, hence completing the fusion process.

1.3.2 Myoblast Fusion in Vertebrates

As in Drosophila, myoblast migration in mice depends on actin remodelling. Myoblasts treated with latrunculin A or cytochalasin D, which block actin polymerisation, show reduced migration in vitro (Constantin et al., 1995; Sanger and Holtzer, 1972), and pharmacological inhibition of F-actin remodelling leads to an inability of myoblasts to migrate, resulting in reduced myoblast fusion (Dhawan and Helfman, 2004; Nowak et al., 2009).

Cell recognition is meditated by nephrin, the vertebrate ortholog of Sns, which localises to the membrane of fusing cells (Sohn et al., 2009). Recognition is then followed by adhesion, mediated by M/N-cadherin (Hollnagel et al., 2002; Radice et al., 1997) as well as by integrin family members, which help to properly align the myoblasts. Beta1-integrin knockout myoblasts adhere but plasma membrane alignment and breakdown does not occur, preventing fusion from occurring (Schwander et al., 2003).

While there is no evidence for an F-actin focus in vertebrates as yet, there is evidence that an actin wall forms along the pre-fusion myoblast. This structure regulates cell fusion through vesicle trafficking, and its formation requires non-muscle myosin type IIA (Duan and Gallagher, 2009). The formation of this actin wall is also dependent on Nap1 the mammalian homologue of Kette, which acts through the N-WASP complex to promote Arp2/3 mediated actin remodelling (SCAR in *Drosophila*) (Nowak et al., 2009).

Additionally, Similar to Drosophila mbc mutants, Dock1-null mice embryos exhibit severely impaired myoblast fusion and skeletal muscle content is reduced (Laurin et al., 2008). Dock1 (mbc) is a GEF which activates the GTPase Rac. In a conditional Rac1 knockout mouse model, the recruitment of Arp2/3 and F-actin to the cell-contact site is reduced, resulting in impaired myoblast migration and fusion (Vasyutina et al., 2009). G-protein coupled receptors BAI 1 and 3 also feed into the Dock/Rac1/Arp2/3 pathway, providing signal transduction from the membrane to the cytoskeleton (Hamoud et al., 2014; Hochreiter-Hufford et al., 2013).
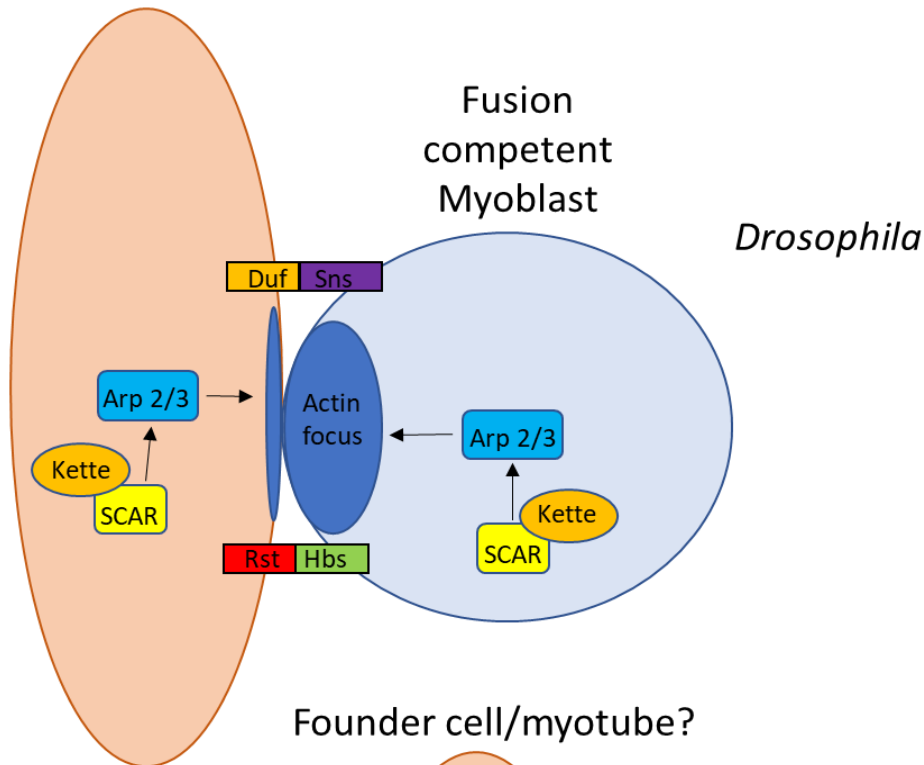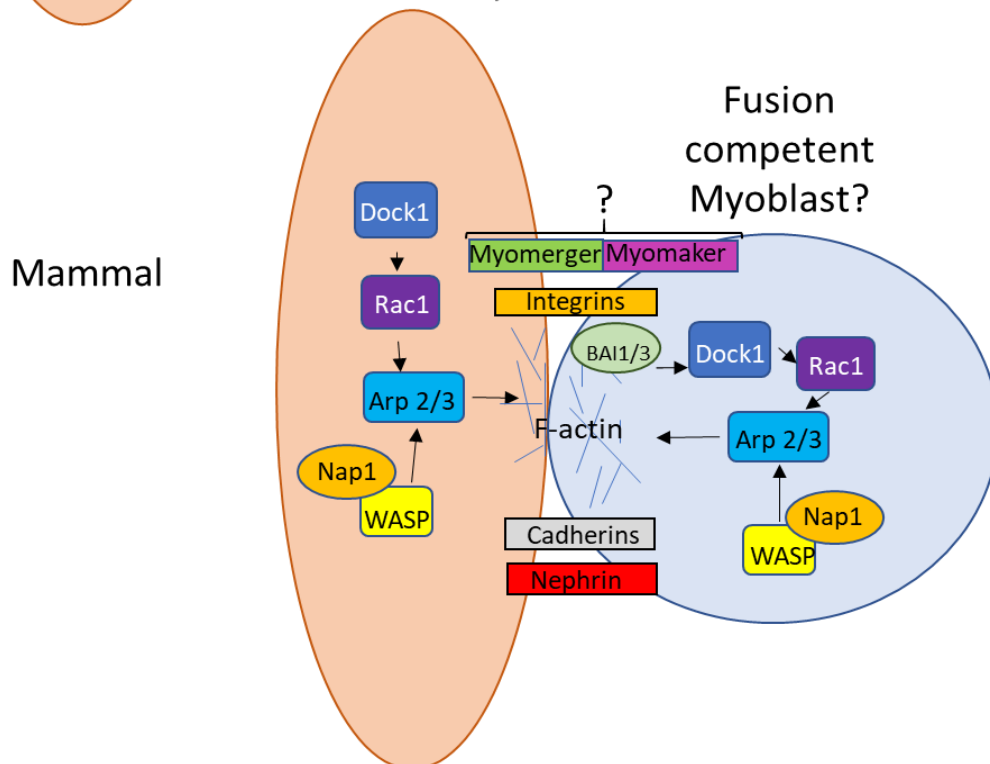
Figure 1.3. Comparison of recognition, adhesion, and actin remodelling during myoblast fusion *in Drosophila (Top) and Mammals (Bottom). Orthologues are shown in the same colour. Proteins spanning both cells are involved in membrane recognition and/or adhesion. Arrows represent signalling cascades.*

1.3.3 The Fusogens: Myomaker and Myomerger

Several proteins and pathways are known to be involved in recognition, adhesion, and cytoskeletal remodelling during fusion. However, until recently, no one protein which is able to directly induce myoblast fusion had been identified and decoupling of the fusion and differentiation pathways has proved challenging. The recent discovery and characterisation of Myomaker and Myomerger/Minion/Myomixer has provided the first examples of muscle specific fusogens. Myomaker and Myomerger are expressed in myoblasts and/or myotubes of vertebrates during differentiation and are not expressed in any other tissue, or in adult skeletal muscle. It is not yet known whether any orthologues are expressed in invertebrates, however it is possible that functional homologs, lacking sequence similarity, do exist.

Myomaker knockout cells fail to fuse, but it is the effect of Myomaker expression in non-muscle cells which is particularly interesting. Myomaker expressing non-muscle fibroblasts are able fuse with C2C12 cells, providing the first example of a muscle specific fusogen (Millay et al., 2016; Millay et al., 2013). A second example soon followed with the discovery of Myomerger. Myomerger too was sufficient to allow fusion between muscle and non-muscle cells, with expression of both Myomaker and Myomerger allowing the fusion of two non-muscle cells with one another (Bi et al., 2017; Quinn et al., 2017; Zhang et al., 2017). It was found that Myomaker is required symmetrically, on both fusing cells, while Myomerger is required asymmetrically, on only one of the cells in a fusing pair. This could be evidence of a *Drosophila*-like model of myoblast fusion, with a founder cell expressing both Myomaker and Myomerger, and a fusion competent myoblast expressing only Myomaker.

The mechanism of action of both Myomaker and Myomerger remains elusive. It is likely that Myomaker is involved in fusion competence, whereas Myomerger may activate fusion through pore formation. There is some evidence of interaction between the two proteins (Bi et al., 2017), but this is disputed (Deng et al., 2017). What is clear is that remodelling of the actin cytoskeleton is crucial for Myomaker and Myomerger to perform their roles. The fusogenic activity of Myomaker and Myomerger is lost through

pharmacological inhibition of F-actin polymerisation (Millay et al., 2013; Zhang et al., 2017), emphasising the importance of cytoskeletal remodelling in myoblast fusion.

1.4 Skeletal Muscle Hypertrophy
Increases in skeletal muscle mass can occur through two distinct processes, hyperplasia and hypertrophy. Hyperplasia refers to the generation of new muscle fibres through satellite cell fusion. Whereas hypertrophy refers to the increase in size of a muscle fibre, driven by a net increase in protein synthesis. Hypertrophy is the main driver of muscle mass increases.

1.4.1 The IGF-1/Akt signalling pathway
The canonical pathway for skeletal muscle hypertrophy is the Insulin-like Growth Factor (IGF-1)/Protein Kinase B (Akt)/ Mammalian Target of Rapamycin (mTOR) pathway (fig 1.4). Growth hormone (GH) is produced by the pituitary gland in response to numerous stimuli, including diet and exercise. GH stimulates the upregulation of IGF-1 in most tissues, but the liver is primarily responsible for increasing serum IGF-1 levels in response to GH (Mathews et al., 1986). However, it is the autocrine/paracrine effect of IGF-1 expressed in muscle itself in response to GH that appears to be the main driver of muscle hypertrophy (Velloso, 2008).

IGF-1 binds to its tyrosine kinase receptor IGFR1, thereby inducing the phosphorylation of Insulin Receptor Substrate 1 (IRS-1). This then results in the activation of Akt through Phosphatidylinositol 3 Kinase (PI3K) (Rommel et al., 2001). Akt goes on to activate mTOR via repression of the tuberous sclerosis 1/2 (TSC1/2) complex, which in turn releases the repression of Ras Homolog Enriched in Brain (Rheb) a GTPase which upregulates mTOR activity. mTOR serves as a central regulator of protein synthesis in the muscle cell, promoting protein synthesis through the activation of translational regulators p70S6K and eIF4E (Hara et al., 1997; Inoki et al., 2002). mTOR can also be activated independently of IGF-1 signalling, notably through the

availability, above a given threshold, of amino acids such as leucine (Burnett et al., 1998; Hara et al., 1998; Kimball et al., 1999), and through mechanical loading, as discussed below.

1.4.2 Loading-Induced Hypertrophy Independent of IGF-1/Akt

The traditional paradigm of muscle hypertrophy, with IGF-1 activating mTOR through Akt, is now being challenged. It is clear that mTOR, and its downstream effectors, are activated independently of IGF-1 signalling. Pharmacological inhibition of IGF-1 using wortmannin does not prevent p70S6K activation during mechanical loading of the muscle (Hornberger et al., 2004). This result provided the first evidence of an IGF-1 independent model of muscle hypertrophy in response to mechanical load.

Knock-in of a dominant negative IGF-1 receptor (IGFR1) abolishes IGF-1 signalling and results in mice with muscles around 30% smaller than in wildtype littermates. However, upon mechanical loading mutant mice displayed a similar hypertrophic response to the wildtype and had normal p70S6K phosphorylation (Spangenburg et al., 2008). Another study demonstrated that mTOR was a central regulator of hypertrophy, which does not rely on PI3K signalling, and can be activated independent of PI3K through overexpression of Rheb (Goodman et al., 2010). While this study did not employ mechanical overload, it provides genetic evidence for mTOR activation independent of the IGF-1/Akt axis.

Tracking of protein phosphorylation levels during a 10-day bout of mechanical overload in mice revealed that mTOR is activated after just a single day. This was accompanied by an increase in p70S6K phosphorylation. In contrast, Akt phosphorylation was not increased until 2-3 days of overload, suggesting another pathway for the activation of mTOR early in muscle overload. The authors identified the mitogen-activated protein kinase kinase (MEK)/extracellular signal-regulated kinase (ERK), signalling through tuberous sclerosis 2 (TSC2), as a possible pathway for the early activation of mTOR in mechanical overload (Miyazaki et al., 2011).

While the IGF-1/Akt/mTOR signalling pathway during muscle hypertrophy is relatively well understood, very little is known about how mTOR is activated in response to mechanical overload. There has been no definitive identification of any mechanosensors thus far. Titin has been proposed as a potential mechanosensing protein. Its size, coupled with its spring-like properties, and interactions with numerous signalling proteins make it an ideal candidate as protein with the potential to detect mechanical load and initiate hypertrophic signalling (Kruger and Kotter, 2016). There are a number of other candidates with similar domain compositions to titin, at both the z-disc and the M-line which may serve as mechanosensors, however the evidence thus far is scarce. Indeed, more work is required to unravel the complex signalling pathways upstream of mTOR.

1.5 Skeletal Muscle Atrophy

Muscle atrophy is a loss in muscle mass caused by net protein degradation which does not simply reflect a lack of hypertrophy. Atrophy can occur in congenital myopathies, ageing, and during starvation. These different physiological inputs serve to upregulate forkhead box transcription factors (FOXO), through Akt repression. FOXO transcription factors also upregulate genes involved in the ubiquitin-proteasome system (fig. 1.4). Models for atrophy *in vivo* include denervation, starvation, and immobilisation of a limb. *In vitro,* myotubes derived from differentiated C2C12 cells can be used, with pharmacological interventions, such as treatment with dexamethasone, used to induce atrophy.

1.5.1 The Ubiquitin-Proteasome System

The Ubiquitin-Proteasome System (UPS) is found across all cells of the body, where it targets proteins for degradation by the proteasome through addition of ubiquitin (ubiquitination). For ubiquitination, three enzymes are required, an E1 ubiquitin-activating enzyme, an E2 ubiquitin-conjugating enzyme, and an E3 ubiquitin-ligating enzyme. E1 ubiquitin-activating enzymes ligase ubiquitin,

facilitating its transfer to an E2 ubiquitin-conjugating enzyme. The E2 ubiquitin-conjugating enzyme then binds to an E3 ubiquitin-ligase, this complex binds to and ubiquitinates a substrate protein, signalling it for degradation in the proteasome (Hershko and Ciechanover, 1998). E3 ubiquitin-ligases provide the substrate specificity for the Ubiquitin-Proteasome System.

The role of the UPS in skeletal muscle atrophy has been well established (Jagoe et al., 2002; Tawa et al., 1997), and the main E3 ubiquitin-ligases identified as Muscle Ring Finger1 (MuRF1) and Atrogin-1 (Bodine et al., 2001). Both MuRF1 and atrogin expression are promoted by FOXO transcription factors (Lee et al., 2004; Sandri et al., 2004; Stitt et al., 2004), which in turn are regulated through Akt. MuRF1 and atrogin expression can also be increased independently of FOXO. MuRF1 expression is increased through NF-κB signalling (Cai et al., 2004), while atrogin expression is increased through the p38 MAPK pathway (Li et al., 2005). Both pathways are positively regulated by TNFα, a pro-inflammatory secreted cytokine released in several atrophic conditions including cancer, disuse, and starvation.

1.5.2 Autophagy

Autophagy refers to the breakdown of cellular components within a membrane-bound compartment, the lysosome. Targets can be small, as in microautophagy, or large, as in macroautophagy, where whole organelles can be degraded. This process can be selective, such as the degradation of a damaged mitochondrion, or non-selective as is the case during atrophy. Selective autophagy requires the recruitment of chaperones to target the protein for degradation.

One proposed mechanism for the selective degradation of damaged proteins in muscle is Chaperone Assisted Selective Autophagy (CASA) (Arndt et al., 2010; Ulbricht et al., 2013). This process involves the binding of several chaperones including BAG3, which itself is upregulated in response to mechanical tension, to damaged filamin-c (FLNC). The E3 ubiquitin-ligase CHIP binds and ubiquitinates the damaged protein, targeting it to the

autophagosome. In addition to facilitating the breakdown of damaged FLNC, BAG3 promotes YAP/TAZ signalling, resulting in the upregulation of FLNC. Thereby contributing to overall protein turnover and not only degradation.

CASA is required for muscle mass maintenance (Arndt et al., 2010; Ulbricht et al., 2013), and CASA components are upregulated in response to resistance training in humans (Ulbricht et al., 2015). Thus, CASA may help to maintain healthy muscle, and even facilitate new muscle growth, through the clearance of damaged cytoskeletal crosslinkers and prevention of the formation of crosslinker aggregates which result in cellular stress.

1.6 Myostatin

Myostatin is a negative regulator of skeletal muscle mass; myostatin-null mice display a double muscle phenotype (McPherron et al., 1997), this effect is also observed in Belgian Blue cattle, which carry a frameshift mutation in the myostatin gene (McPherron and Lee, 1997). Myostatin mutations have been identified in humans (Schuelke et al., 2004), where gross muscle hypertrophy is observed. This conservation demonstrates the importance of myostatin in regulating skeletal muscle mass in mammals.

Myostatin binds to activin type II receptor (ActRII) on the surface of the muscle cell, initiating a cascade of phosphorylation which results in the inhibition of the activity of the protein kinase Akt, therefore inhibiting IGF-1 mediated protein synthesis. This inhibition of the Akt/MTOR pathway releases the inhibition of the FOXO transcription factors, thereby allowing the increased expression of atrophy-associated ubiquitin ligases atrogin and MuRF1 (Sandri et al., 2004; Stitt et al., 2004). Phosphorylation of Smad2 and 3 also occurs as a result of ActRII activation (Rebbapragada et al., 2003). Phosphorylated Smad2 and Smad3 Smad2 and 3 translocate to the nucleus where they downregulate gene transcription independent of blocking mTOR signalling (Elkina et al., 2011) (fig. 1.4).

Myostatin, and its and downstream signalling pathway, have been proposed as potential druggable targets in muscle wasting diseases (Tsuchida, 2008).

It is important to understand the mechanism by which myostatin acts, including any genes which are up/downregulated through myostatin signalling, to provide more insight into its potential as a therapeutic target.
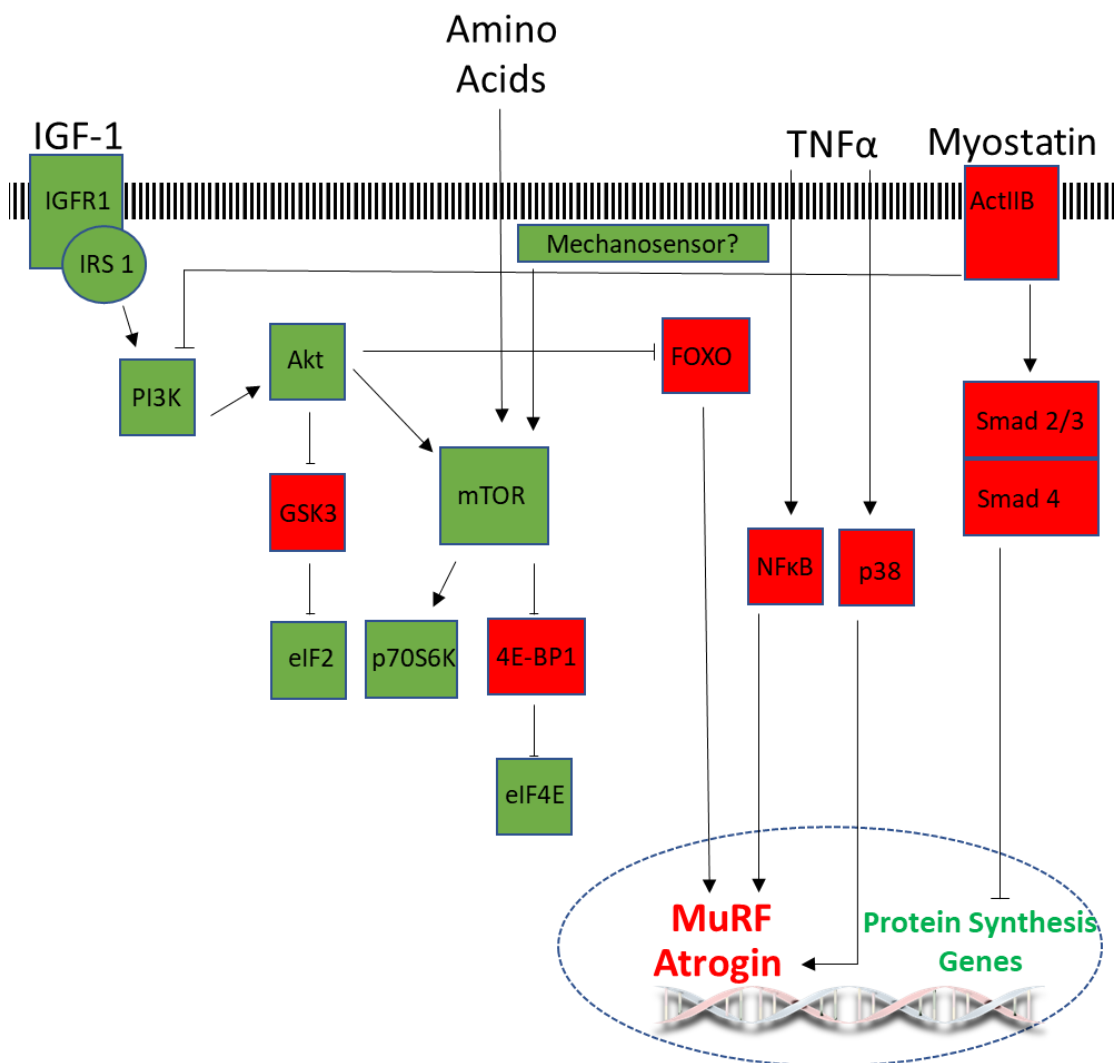
Figure 1.4. Simplified schematic of skeletal muscle hypertrophy and atrophy pathways. *Up-regulators of protein synthesis are shown in green, down-regulators in red. Some intermediates have been omitted.*

1.7 The KY Protein

1.7.1 The *ky/ky* Mouse

The *ky/ky* mouse is the result of a spontaneous mutation of the Kyphoscoliosis Peptidase (Ky) gene in the BDL mouse strain. This mutation produced a strain of mice with kyphoscoliosis (Dickinson and Meikle, 1973). The Ky gene was identified and the mutation giving rise to the ky/ky mouse was discovered to be a GC deletion, resulting in a premature stop codon (Blanco et al., 2001). Postnatally these mice display abnormal spinal curvature, most likely caused by the weakening of the paraspinal muscles, which also prevents mice from reaching to a ledge during the placing response test. No phenotype is detected during the embryonic development of these mice, reflecting the need for mechanical loading of the muscles to reveal the muscular defects (Blanco et al., 2001).

While muscle mass is consistently lower overall in *ky/ky* mice compared to wildtype (Marechal et al., 1995), it is mostly the constantly active, type I fibre dominant muscles that are affected by this mutation. Between 6 and 25 days after birth prominent necrosis and regeneration in the soleus, gracilis, paraspinal, and back muscles is observed (Bridges et al., 1992). Electron microscopy has also demonstrated the accumulation of autophagic vesicles, as well as z-disc thickening and A-band streaming in these postural muscles. The absence of KY results in an inability of type II(A&B) fibres to respond to an increase in mechanical load with hypertrophy, suggesting that the KY protein plays a role in all muscle types during tension-induced hypertrophy (Blanco et al., 2001). Additionally, the Ky mutant mouse displays aggregation of the actin cytoskeleton-associated proteins FLNC (Beatham et al., 2004a) and Xin (Beatham et al., 2006), a sign of a reduced ability to degrade and replace damaged cytoskeletal proteins.

1.7.2 KY-Associated Human Myopathies

Three independent cases of human myopathies associated with a mutation resulting in non-functional KY have so far been reported. Each case was the result of a different mutation resulting in KY loss of function. There is significant overlap in the pathologies observed between the cases. Some variability is seen, likely accounted for by the highly inbred populations causing the accumulation of other deleterious mutations.

A girl presenting with severe and progressive walking difficulties, resulting from generalised muscle weakness, was the first patient identified with a KY loss of function mutation. This patient suffered from mild contractures in the shoulders, hips, and feet, along with cavus feet and lordosis. Some small muscles fibres were observed with some of these having abnormal sarcomeres with thickened Z-discs and small nemaline rods. Internalised nuclei, an indicator or muscle fibre regeneration, were also observed. As in the *ky/ky* mouse, aggregation of FLNC was observed. Whole-exome sequencing revealed a homozygous one-base deletion in *Ky*, predicted to result in a truncated protein (Hedberg-Oldfors et al., 2016).

The second example of a KY-associated myopathy comes from two brothers sharing a mutation resulting in an early stop codon in exon 6 of the *Ky* gene. Both brothers display atrophy and weakness of the lower limbs, as well as tongue atrophy and kyphosis. The younger sibling also suffers from upper extremity weakness, speech difficulties, and impaired intellectual development in addition to the phenotypes observed in his elder brother. FLNC aggregation was also observed in this patient. Autozygosity mapping and whole exome sequencing revealed a homozygous variant, which constitutes a premature termination codon in *Ky* exon 6, hypothesised to lead to nonsense-mediated mRNA decay (Straussberg et al., 2016).

Genetic analysis of twelve individuals from a Bedouin Israeli tribe, presenting with autosomal recessive progressive spastic paraplegia, revealed a single homozygous variant within *Ky* resulting in a frame-shift and loss of function. Spasticity of the lower limbs, hyperreflexia, and toe walking were observed in

all patients, with kyphoscoliosis evident in older patients. Most also had atrophy of the tongue and muscle biopsies showed some small angular fibres and some with centralised nuclei. The observed pathology was detectable by age two (Yogev et al., 2017).

The involvement of KY in human disease, with similar hallmarks as the observed phenotypes in *ky/ky* mice, demonstrates the importance of KY in skeletal muscle mass maintenance, especially in postural muscles.

1.7.3 KY and Autophagy

KY is required for tension-induced hypertrophy (Blanco et al., 2001). FLNC accumulation and mis-localisation is a hallmark of loss of function of KY in both mice and humans (Beatham et al., 2004a; Hedberg-Oldfors et al., 2016; Straussberg et al., 2016). As well as this, FLNC and KY interact at the z-disc (Baker et al., 2010; Beatham et al., 2004a). As CASA is responsible for turnover of damaged FLNC and is required for hypertrophy, it has been hypothesised that KY plays a role in CASA.

Recent examination of KY deficient mice, zebrafish, and C2C12 cells has provided further evidence of a link between KY and CASA. Differentiated, KY deficient, C2C12-derived clones show a trend of increased transcription of CASA factors. *bag3* and *flnc* are also found to be upregulated in the muscle of a KY knockout zebrafish model. While these fish lack overt pathology, swimming in viscous media does not produce the further increase of *bag3* or *flnc* expression which is observed in wildtype fish. Finally, *ky/ky* mice have elevated *bag3* expression in the exterior digitorum longus (EDL), a non-pathological tissue, and BAG3 turnover is impaired in the soleus (Jokl et al., 2018). These results point towards KY helping to maintain and increase muscle size through CASA directed protein turnover, however, a direct mechanism has not yet been discovered. It is possible that KY deficiency simply disrupts the structure of the z-disc and accumulation of damaged cross-linkers results from this, rather than a block on CASA.

1.7.4 The KY Protein and Interacting Partners

According to predictions from sequence analysis the KY protein is a transglutaminase-like protein (Baker et al., 2010). However, to date, no evidence of catalytic activity exists, and it is possible that the transglutaminase domain has been co-opted for protein-protein interactions (Anantharaman et al., 2001). Indeed, KY has been shown to interact with several proteins, including FLNC as outlined above. As well as FLNC, KY interacts with IGFN1 at the z-disc (Baker et al., 2010). At the time this interaction was uncovered very little was known of the function of IGFN1, warranting further investigation to develop the understanding of KY and its role in disease.

1.8 IGFN1

1.8.1 IGFN1 Discovery, Structure, and Interactions

IGFN1 is a large skeletal muscle protein localised to both the z-disc and the nucleus (Baker et al., 2010; Mansilla et al., 2008). It was identified through a yeast two-hybrid screen as an interacting partner of KY at the z-disc (Baker et al., 2010).

The *Igfn1* locus is complex with multiple putative ATG start sites, which, along with alternative splicing, produce multiple IGFN1 isoforms (fig. 1.5). Full-length IGFN1 consists of 11 Immunoglobulin/Immunoglobulin-like (IG/IG-like) and fibronectin type 3 (FN3) domains, separated by a large unstructured region. IGFN1_V1 is an isoform resulting from alternative splicing which lacks the unstructured region. Two other isoforms consisting of the c-terminal globular domains have also been confirmed, expressed from internal promoters within the *Igfn1* gene (Baker et al., 2010).

The *Igfn1* gene is highly conserved across mammals, with the exception of the sequence coding for the unstructured region (Baker et al., 2010), suggesting the amino acid composition of this region is not relevant to its function. Regions such as this have been proposed to provide flexibility to a protein, allowing conformational changes to occur, potentially exposing binding sites for different clients (Dyson and Wright, 2005). Therefore, IGFN1 is likely to

undergo conformational changes in response to some stimulus, possibly in response to mechanical tension.

The domain composition of IGFN1 is like that of sarcomeric proteins involved in maintaining the structural integrity of the sarcomere through cycles of contraction and relaxation. Titin and myomesin both contain globular domains which allow these proteins to act as molecular springs, absorbing the forces of contraction (Rief et al., 1997; Schoenauer et al., 2005). The position of IGFN1 at the z-disc, an area integral to sarcomeric structure, and its domain composition make it an ideal candidate to help maintain the structure of the sarcomere.

IGFN1 has no apparent catalytic domains. It is therefore likely that any function IGFN1 performs occurs through protein-protein interactions via its globular domains. Along with KY, through Y2H and pull-downs, IGFN1 was found to interact with FLNC, titin, and actin (Baker et al., 2010), all important proteins for maintaining sarcomeric structure. These proteins have also been implicated in mechanotransduction and hypertrophy, with FLNC and KY likely to be integral to CASA.

As well as the above, IGFN1 interacts with MLK-Like Mitogen-Activated Protein Triple Kinase 20 (MLTK)/ Leucine Zipper-and Sterile Alpha Motif-Containing Kinase (ZAK) (Baker et al., 2010). Recessive ZAK mutations are implicated in human disease (Vasli et al., 2017). IGFN1 also interacts with Eukaryotic translation elongation factor 1A (eEF1A) (Mansilla et al., 2008), a guanine-nucleotide binding protein, which transports aminoacylated tRNA to the ribosomal A site during protein synthesis (Negrutskii and El'skaya, 1998). The significance of the interaction between IGFN1 and ZAK, and IGFN1 and eEF1A will be discussed below.

Finally, knockdown of IGFN1 in C2C12 cells results in a lack of fusion (Li et al., 2017). Though these initial experiments did not include a rescue of the wildtype fusion phenotype through expression of IGFN1. IGFN1 expression was also found to fluctuate throughout myoblast fusion and differentiation,

suggesting it plays a relevant role in these processes. This thesis will expand on this work, examining the role of IGFN1 in myoblast fusion.
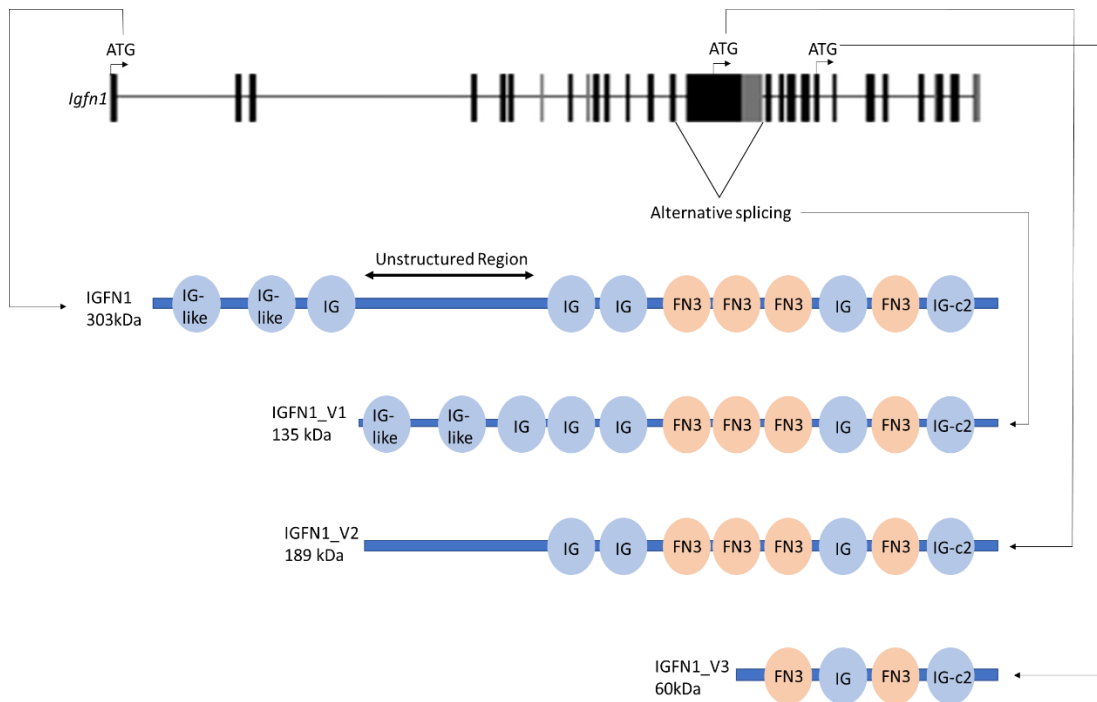
Figure 1.5. Domain composition of IGFN1 isoforms. *Top, exons of Igfn1, with ATG sites shown, adapted from (Baker et al., 2010) with authors permission. Bottom, IGFN1 isoforms produced from the Igfn1 locus via putative internal ATG promoter sites or alternative splicing. Immunoglobulin (IG), Immunoglobulin-like (IG-like), and Fibronectin type III domains (FN3) are indicated.*

<u>1.8.2 IGFN1 and Atrophy</u>

IGFN1 expression is positively correlated with atrophic conditions. Denervation of a muscle induces muscle fibre atrophy and is a common model for muscle atrophy *in vivo* (Pellegrino and Franzini, 1963). IGFN1 expression was found to be increased in response to denervation (Mansilla et al., 2008). In addition to this IGFN1 was found to interact with eEF1A, leading the authors to propose a mechanism whereby IGFN1 downregulates muscle protein synthesis, in response to denervation, by repressing eEF1A activity.

Along with denervation, IGFN1 expression is correlated with myostatin signalling, a negative regulator of skeletal muscle mass. Using soluble activin type B receptors (ActRIIB) to sequester myostatin *in vivo* led to significant increases in muscle mass (Rahimov et al., 2011). This was accompanied by a significant reduction of IGFN1 mRNA expression. Furthermore, when myostatin signalling is increased via injection of adenoviral vectors in mice, muscle mass decreases and IGFN1 mRNA expression increases (Chen et al., 2014).

These findings raise the possibility that IGFN1 is involved in atrophy, possibly acting as an effector of the myostatin signalling pathway. However, no direct mechanism whereby IGFN1 causes atrophy has been identified thus far.

<u>1.8.3 IGFN1 and ZAK</u>

IGFN1 interacts with ZAK (Baker et al., 2010), a mixed lineage kinase family member with two isoforms, ZAKα and ZAKβ (Gotoh et al., 2001). ZAKα is primarily expressed in the heart where it induces cardiac hypertrophy when overexpressed *in vivo* (Christe et al., 2004). Overexpression of ZAKα in cardiomyocytes *in vitro* also results in hypertrophy (Huang et al., 2004). ZAKβ is primarily expressed in skeletal muscle where its overexpression through electroporation induces an increase in muscle fibre cross-sectional area (Li, 2016). Dominant-negative Zak mutations in mice result in hindlimb duplication, implicating ZAK in limb development (Spielmann et al., 2016). Human patients with ZAK deficiency do not show abnormal limb development. However, they

suffer from muscle weakness, scoliosis, and reduced ambulant ability, underpinned by a predominance of type I muscle fibres of varying sizes displaying centralised nuclei (Vasli et al., 2017), hallmarks shared with patients with mutations in the *Ky* gene.

ZAK is known to increase p38 phosphorylation (Gotoh et al., 2001). p38 activation through phosphorylation is implicated in both hypertrophy and atrophy. p38 is activity is increased in response to immobilisation (Kim et al., 2009) and denervation (Paul et al., 2010), and p38 activity is responsible for the upregulation of MuRF1 (Li et al., 2005). On the other hand, p38 phosphorylation is increased in response to mechanical tension, suggesting a role in hypertrophy (Boppart et al., 2001; Carlson et al., 2001; Hornberger et al., 2004). The roles of p38 during skeletal muscle development (Keren et al., 2006), and in satellite cell function (Segalés et al., 2016), further complicate this picture and reflect the fact that p38 is not one single protein and in fact represents a family of four MAP kinases (Cuenda and Rousseau, 2007).

The upregulation of ZAK in the EDL of the *ky/ky* mouse provides a further functional link between the KY/IGFN1 complex and ZAK (Blanco et al., 2004). It is possible that IGFN1 acts to aid ZAK in signalling, acting either as a scaffold, or as a mechanosensor to upregulate p38 in response to mechanical tension. IGFN1 may also act to inhibit ZAK signalling, thereby preventing ZAK-induced hypertrophy.

1.9 Hypotheses and Objectives
1.9.1 Hypotheses
The function of IGFN1 has thus far been elusive. Based on the literature presented above several hypotheses as to the function of IGFN1 were outlined at the outset of this project (fig.1.6). These hypotheses are not mutually exclusive, it is possible that IGFN1 performs many different overlapping and inter-related roles, especially as multiple isoforms of IGFN1 are expressed. The initial hypotheses identified are as follows:

- **IGFN1 is a structural protein.** The most simple hypothesis regarding the role of IGFN1 is that it acts as a structural protein. Its localisation to the z-disc, lack of catalytic activity, and its domain composition make it an ideal candidate to perform such a role. IGFN1 also interacts with many sarcomeric proteins involved in maintaining the structural integrity of the sarcomere, such as titin and actin.

- **IGFN1 is a scaffold for signalling/effector proteins.** IGFN1 contains several immunoglobulin domains, these domains are often implicated in protein-protein interactions. Indeed, IGFN1 has been found to interact with numerous proteins including the signalling kinase ZAK. It is possible that IGFN1 acts as a central signalling scaffold at the z-disc, with its unstructured region allowing for conformational changes exposing different binding sites to potential interacting partners.

- **IGFN1 is a mechanosensor.** IGFN1 may act to sense mechanical tension at the z-disc and relay this to signalling proteins, facilitating muscle hypertrophy. The globular domains of IGFN1 may be able to unfold and refold in response to mechanical tension, as has been observed in other muscle proteins with similar domains, providing a mechanism for detecting mechanical load. This hypothesis overlaps with the two hypotheses proposed above and would require interactions with relevant signalling proteins. The interaction of IGFN1 and KY provides a mechanism by which IGFN1 could act as a mechanosensor in CASA. However, the association between IGFN1 and atrophic signalling places some doubt on this hypothesis.

- **IGFN1 is part of the myoblast fusion machinery.** Preliminary data at the outset of this project suggests a role for IGFN1 in myoblast fusion. The suggested interaction between IGFN1 and actin may facilitate its role in myoblast fusion as actin remodelling is critical for this process. It

is likely that any role in actin remodelling requires interacting partners, due to the lack of catalytic domains in IGFN1.

- **IGFN1 is a facilitator of atrophy.** Although no direct evidence of IGFN1 inducing atrophy currently exists, IGFN1 expression is positively correlated with atrophic conditions. Again, it is unlikely that IGFN1 acts to induce atrophy directly, requiring interacting partners to facilitate any role in atrophy.
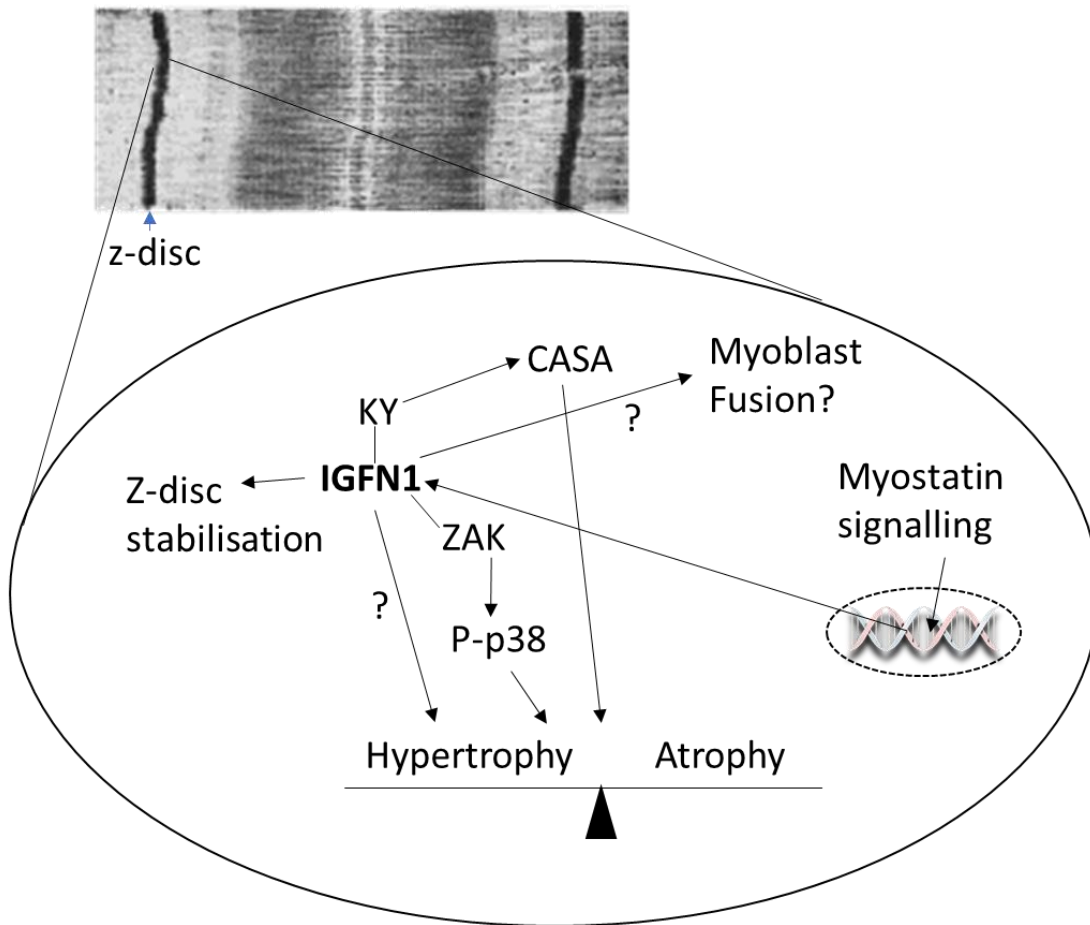
Figure 1.6. Summary of proposed roles for IGFN1 in skeletal muscle. IGFN1 expression is influenced by myostatin signalling, it also interacts with KY and ZAK, possibly facilitating a role in CASA or muscle mass maintenance through another unknown pathway. Its domain composition and position at the z-disc points towards a role in structural stability of the z-disc. A role for IGFN1 in myoblast fusion has also been suggested by fusion deficiency in knockdown cells.

1.9.2 Objectives

In order to explore the above hypotheses, the initial objectives, with associated aims, of this project were:

Characterisation of a C2C12-derived IGFN1 knockout cell line.

- Determine the effect of IGFN1 knockout on cell size, in untreated conditions and following induction of atrophy

- Examinine the effects of IGFN1 knockout on fusion and differentiation, through calculation of relevant indexes
- Determine the G:F actin ratio of knockout cells to reveal any actin remodelling deficits
- Rescue of any phenotypes observed through IGFN1 expression

Production and purification of IGFN1.
- Develop a protocol produce and purify the IGFN1_V1 isoform in *E.coli* for use in future AFM experiments.
- If the above fails, produce and purify smaller IGFN1 fragments

Identification and validation of IGFN1 interaction partners.

- Perform pull-downs of mouse muscle lysates against the proteins produced above for LC-MS/MS identification of potential interaction partners
- Validate interactions identified through pull-downs, co-localisation, and functional analysis

As the project progressed and more evidence came to light these objectives were further developed to allow new avenues of research to be followed, as is discussed in the following chapters.

CHAPTER 2: MATERIALS AND METHODS

Chapter 2: Materials and Methods

2.1 Solutions and Reagents

Name	Formula	Notes
10X Running Buffer	250mM Tris, 1.9M Glycine, 35mM SDS	Dilute in dH$_2$O
10X Transfer Buffer	250mM Tris, 1.9M Glycine	Dilute 1:2:7 Buffer:Methanol:dH$_2$O
50X TAE	2M Tris base, 950mM Acetic Acid, 500 mM EDTA, pH 8	Dilute 1:49 in dH$_2$O
Blocking Buffer	PBST + 4% Skimmed Milk Powder	
Coomassie Destain	40% Methanol, 10% Acetic Acid, 50% H$_2$O	
Coomassie Stain	1g/l Coomassie Brilliant Blue (VWR, R-250), in 30% Methanol, 10% Acetic Acid, 60% H$_2$O	
Differentiation Media	DMEM + 2% FBS + Penicillin Streptomycin to 1X (Gibco, 15140122)	
Elution Buffer	50mM NaH$_2$PO$_4$, 0.5M NaCl, 250mM Imidazole pH8	
Freezing Media	10% DMSO, 40% GM, 50% FBS	
Growth Media	DMEM + 10% FBS + Penicillin Streptomycin to 1X (Gibco, 15140122)	
LB Agar	LB as above + 7.5g Agar	
LB Broth	In 1l H$_2$O: 10g Tryptone, 10g NaCl, 5g Yeast Extract, pH 7	
Mowiol	2.4g Mowiol 4-88, 6g glycerol, 6ml $_{dd}$H20, 12ml 0.2M Tris	
Native Binding Buffer	50mM NaH$_2$PO$_4$, 0.5M NaCl, pH8	
Native Wash Buffer	50mM NaH$_2$PO$_4$, 0.5M NaCl, pH8, 20 mM imidazole	
PBS	140mM NaCl, 2.7mM KCl, 9.6mM NaH$_2$PO$_4$, 1.5mM KH2PO4, pH 7.3	Tablets from Thermo Scientific BR0014
PBST	PBS as above with 0.1% Tween-20	
Resolving Gel Solution	0.5Xml 30% Bis-Acrylamide, 3.75ml 1.5M TRIS NCl pH 8.8, 11-X ml dH$_2$O, 150µl 10% SDS, 10µl TEMED, 120µl 10% APS	X=Desired gel % TEMED and APS added last.
Stacking Gel Solution	1.32ml 30% Bis-Acrylamide, 2.52ml 0.5M TRIS NCl pH 6.8, 6 ml dH$_2$O, 100µl 10% SDS, 15µl TEMED, 80µl 10% APS	TEMED and APS added last.
Stripping Buffer	10M Tween-20, 200mM Glycine, 3.5mM SDS, pH2	
Wash Buffer	50mM NaH$_2$PO$_4$, 0.5M NaCl, 20mM Imidazole pH8	

2.2 Antibodies

2.2.1 Primary Antibodies

Antibody	Supplier	Product/Project code	WB Concentration	IF Concentration
Anti-actin	Cytoskeleton	AAN01	1:300	N/a
Anti-α-actinin (EA53)	abcam	ab9465	N/a	1:250
Anti-His-HRP	BIORAD	MCA1396P	1:300	N/a
Anti-GAPDH	Sigma	G9295	1:50000	N/a
Anti-IGFN1 Kip1	21st Biochemicals	PR0671-2686	1:250	1:150
Anti-IGFN1 Kip1b	21st Biochemicals	1159A 3413V11	1:250	N/a
Anti-IGFN1 Kip1c	21st Biochemicals	1159B 3413V12	1:250	N/a
Anti-COBL	SIGMA	HPA019167	1:300	1:150
Anti-V5	SIGMA	V8137	1:250	N/a

2.2.2 Secondary Antibodies

Antibody	Supplier	Product code	WB Concentration	IF Concentration
Anti-rabbit IgG HRP	Abbkine	A21020	1:10000	N/a
Anti-mouse IgG HRP	Santa Cruz	sc-2314	1:10000	N/a
Anti-mouse IgG TRITC	Abcam	ab6718	N/a	1:100
Anti-mouse IgG FITC	Abcam	ab6717	N/a	1:100
Anti-rabbit IgG FITC	Abcam	ab6785	N/a	1:100
AlexaFluor 488 anti-rabbit	Invitrogen	R37116	N/a	1 drop per ml
AlexaFluor 488 anti-mouse	Invitrogen	R37120	N/a	1 drop per ml

2.3 Primers

Primer	Sequence	Purpose
COBL FWD 1	CACCATGGACGCGCCGCGTGCACTGG	Cloning of COBL
COBL REV 1	CACGAGCAAGGGAACCTTTCTTAGT	
COBL FWD 2	CACCATGGACCCCACAGGAAGGAAGATGAA	
COBL REV 2	GAGCAAGGGAACCTTTCTTAGTCT	
d1-d3 FWD 1	AACAGATCGAAGGTCGTCAGAGCATCAGGCAGCTGGTG	Cloning of IGFN1 fragments into Im9 vector
d1-d3 REV 1	CTATCAACAGGAGTCCAAGCCCAGGCACTGGAGGCATG	
d6-d11 FWD 1	AACAGATCGAAGGTCGTCACCTGGAGGTTCAGGATTGC	
d6-d11 REV 1	CTATCAACAGGAGTCCAAGCGAGGGTGGCTGTGCTGAC	
COBL qPCR FWD 1	GCCTGTCATTCAAAGGCCAC	qPCR amplification of COBL
COBL qPCR REV 1	CTGCAGTCTTCCGGAGCTTT	
MYH7 qPCR FWD 1	ACCCTCAGGTGGCTCCGAGA	qPCR amplification of MYH7
MYH7 qPCR REV 1	TGCAGCCCCAAATGCAGCCA	
HPRT qPCR FWD 1	GTTGGATACAGGCCAGACTTTGTT	qPCR amplification of HPRT (housekeeping control)
HPRT qPCR REV 1	GATTCAACTTGCGCTCATCTTAGG	

COBL seq 1	CACCATGGACGCGCCGCGTGCACTGG	Sequencing of COBL constructs
COBL seq 2	GCTCCTGAGAAATCTGTACGACTGGT	
COBL seq 3	AGACATGAAGAAGCGCAGAGCC	
COBL seq 4	TGAGCTCTCCCTCAGATGCCA	
COBL seq 5	TCATCTGTCCCCATCTCAGACT	
COBL seq 6	CGGAAGCAGGACCATATCCCCA	
COBL seq 7	CCAGGAAAGATGATGCAGCTCCC	
COBL seq 8	ACAGATGGTCAAGACGCAGA	
COBL seq 9	CATCCGCTCGGGCACAGGAG	
TG1F1	TTGGAGGCAAGCGTAAAACC	Validation of COBL Knockout in C2C12 myoblasts
TG1R1	AACCACACTCTGCTTCTCCA	
TG2F1	TTTCTCCTTTTCAGCCACGC	
TG2R1	GTTCTCAGACAATCCACGGG	
TG3F1	ATCCTGCCATACCCAATCCT	
TG3R1	CTTCCCATGCCCACCTCTAG	
LoxP Fwd	CAA CGT GCT GGT TGT TGT GC	
LoxP Rev	CTT CGG GCA TGG CGG ACT TG	
Actn1 Fwd	GACCATTATGATTCCCAGCAGAC	
Actn1 Rev	CGGAAGTCCTCTTCGATGTTCTC	
COBL 11-12 Fwd	AGAAAGCCACCATGCCTACC	COBL Colony PCR

COBL 11-12 Rev	TTCCATGACCTGCCTGTGTC	

2.4 Cell Culture

2.4.1 Proliferation

Cells were thawed and immediately transferred to flasks containing pre-warmed growth media (GM) and incubated at 37°C, 5% CO_2. Upon reaching 70-80% confluency cells were split by washing twice with PBS and incubating with 0.05% trypsin (SIGMA, 59427C) at 37°C until cells detached. Trypsinisation was stopped by adding a few drops of FBS (Foetal bovine serum, South American, Invitrogen, 10270-106) and cells were transferred into new flasks containing fresh pre-warmed growth media. For applications requiring cell counting prior to reseeding, cells were counted using a haemocytometer and then seeded at an appropriate density.

2.4.2 Freezing

Cells were trypsinised as above then centrifuged at 1200rpm for 12 minutes to form a pellet. The pellet was then resuspended in freezing media (in general, 3ml of freezing media per T75 flask) and immediately transferred to cryotubes and placed at -80°C for short term storage, aliquots were transferred to liquid nitrogen for long term storage.

2.4.3 Differentiation

Cells were grown in GM until they reached 100% confluency whereupon the GM was exchanged for differentiation media (DM) (Blau et al., 1983). DM was changed daily, and cells observed under a light microscope until the desired state of differentiation was reached.

2.4.4 Transfections

Transfections were performed using the GenJet transfection reagent (SignaGen, Cat # SL100488) following the provided protocol. For Cos7 and 3T3 cells, DNA was diluted in DMEM to the appropriate concentration (specified in the SignaGen protocol), before transfection reagent diluted in DMEM was added to the DNA solution and incubated for 5 minutes to form a transfection complex. This complex was then added to cells. For C2C12 transfections an enhanced protocol was used, whereby cells were trysinised, pelleted, and then resuspended in the transfection complex before being incubated at 37°C for 20 minutes. Cells were then transferred into an appropriate growth vessel containing pre-warmed GM. In both cases GM was replaced 16-24 hours post-transfection.

2.4.5 Staining and Immunofluorescence

Cells were fixed by washing with PBS followed by 1 minute incubation with ice cold acetone:methanol (1:1) and another PBS wash. For permeabilisation cells were incubated in 4% BSA PBS with 0.1% triton for 30 minutes. Blocking was performed using incubation in 4% BSA PBS for 1 hour and primary antibody incubations were performed using antibody at the appropriate concentration in 4% BSA PBS overnight at 4°C. Secondary antibody incubations were performed following 3 PBS washes using antibody at the appropriate concentration in 4% BSA PBS for a minimum of 2 hours. Following incubation 3 PBS washes were performed, followed by a final wash in dH$_2$O (Renshaw, 2016). Cells grown on coverslips were mounted onto slides using MOWIOL with DAPI and left to set before imaging. Cells grown on 6-well plates (differentiating cells) had coverslips fixed to them using MOWIOL+DAPI.

For phalloidin staining, fixed and permeabilised cells were washed twice in PBS before phalloidin (either: Phalloidin CruzFluor 488 Conjugate, Santa Cruz, sc-363791. Or: Rhodamine Phalloidin, Cytoskeleton, PHDR1) was added, and the cells incubated for 30 minutes in the dark (Capani et al., 2001). Cells were then washed, and slides/coverslips mounted as above.

2.4.6 Cell Stretching

C2C12 cells were plated onto Bioflex Collagen-I plates (FlexCell) (Banes et al., 1985) at $3x10^5$ cells per well in growth medium. After 24hrs plates were loaded onto the Flexcell 4000T baseplate. Stoppers were applied to prevent stretching of control cells. Experimental wells were subjected to a cyclic stretching programme of 10% elongation for 2hrs at 1.3Hz. Cells were immediately processed via fixation for imaging.

2.4.7 Fluorescence Calculations

Phalloidin stained cells were imaged using a Zeiss Upright 710 confocal microscope. All settings including gain and exposure time remained constant between samples. Images were analysed using ImageJ (NIH). Cells were outlined using the Threshold feature and corrected total cell fluorescence (CTCF) was calculated as: CTCF = Integrated Density - (Mean Value Grey of background x Area of cell).

2.4.8 Scratch Wound Assay

Cells were grown to 100% confluency in a 6-well plate. A 200μl pipette tip was used to scrape cells from the growth surface in a single vertical line (t=0) (Rodriguez et al., 2005). Cells were imaged at a number of timepoints using an Evos XL core microscope (Thermofisher). For determination of wound closure three measurements per well, per timepoint, were taken and averaged. An average percentage wound closure was then calculated compared to the wound at t=0.

2.5 CRISPR/Cas9 targeting in C2C12

2.5.1 Constructs

Pre-designed plasmids were purchased from Santa Cruz. Cordon-bleu CRISPR/Cas9 KO Plasmid (m): sc-419728 and Cordon-bleu HDR Plasmid (m): sc-419728-HDR were obtained for CRISPR/Cas9 targeting and homology directed repair respectively. For more details regarding specific target sites see chapter 7.5.

2.5.2 Transfection and Clonal Selection

Both sets of constructs were co-transfected into wildtype C2C12 cells, using the GenJet system, as described above. After 24hrs growth media was changed for growth media containing 4µg/ml puromycin for selection. Following 3-4 days of puromycin selection, protein extracts were taken (see below), or cells were seeded for clonal selection using a serial dilution starting with a stock of ~100 cells/well in a 96 well plate. Dilutions of this stock were made at 1:10, 1:50, 1:100, 1:200, and 1:500, and seeded across the plate. Cells were observed and wells in which single colonies formed were selected for expansion and analysis.

2.6 Protein Extraction

2.6.1 Extraction of Protein from Cultured Cells

As per Abcam protocols, cells were washed twice with PBS on ice, followed by addition of minimal ice-cold RIPA buffer (Sigma, R0278) with protease inhibitors (Sigma, P8340). A cell scraper was used to remove cells from the growth surface, the resulting sample was then placed on a shaker at 4°C for 30 minutes. The sample was then centrifuged (15 minutes, 12,000rpm, 4°C) and the resulting supernatant placed in a fresh tube and placed on ice for immediate use, or at -80°C for longer term storage.

2.6.2 Extraction of Protein from Tissues

Tissue was finely chopped and placed into ice-cold RIPA buffer with protease inhibitors (3ml RIPA per 1g muscle tissue) for 10 minutes on ice. Tissue was then snap frozen in liquid nitrogen and homogenised in a pestle and mortar. The resulting homogenised tissue was then added back into the original RIPA buffer and incubated at 4°C for 2 hours with shaking. Samples were then centrifuged (15 minutes, 13,000g, 4°C) and the resulting supernatant placed in a fresh tube and placed on ice for immediate use or at -80°C for longer term storage (Li et al., 2017).

2.7 SDS-PAGE Gel electrophoresis

2.7.1 Sample Preparation and Bradford Assay

Sample concentration was determined via Bradford assay with BradfordUltra reagent (Expedeon; BFU) on an MRX microplate reader and Revelation software (Dynex Technologies). In order to prevent detergents from interfering with readings a 10-fold $_{dd}H_2O$ dilution was used and a standard curve generated, with BSA diluted in 10% RIPA buffer to known concentrations (Bradford, 1976).

Typically, 20-50µg of protein was used per sample along with 4x NuPage LDS buffer (Invitrogen; NP0008) and 10x NuPage sample reducing agent (Invitrogen; NP004) $_{dd}H_2O$ was used to make up the remaining volume (typically 10-15µl loaded per well). Samples were then heated to 90°C for 10 minutes prior to loading on gels. For *E. coli* pellets, samples were briefly centrifuged at low speed to facilitate easier pipetting due to high levels of DNA in the samples.

2.7.2 Gel Pouring and Running

8-12% Bis-Acrylamide resolving gels were made up, depending on the size of the protein of interest, by pipetting resolving gel solution between two glass slides and leaving to set. Once set, stacking gel solution was added along with plastic combs to form wells, this was then left to set. Once set, combs were removed, and gels were placed into a BioRad tank along with running buffer supplemented with NuPage antioxidant (NP0005) and samples loaded. Typically, gels were run at 160v (dependent on size of protein of interest) until the dye front migrated to the bottom of the gel (Laemmli, 1970).

2.7.3 Transfer and Western Blotting

Wet transfers were performed to transfer from gels to nitrocellulose membrane. Gels were placed onto the transfer buffer-soaked membrane in between filter paper and fibre pads, also soaked in transfer buffer. This was placed in a cassette and loaded into a BioRad tank and filled with transfer

buffer. For 1 hour transfers the tank was placed on ice to prevent overheating and run at 100v, for overnight transfers 10v was used as per BioRad instructions.

Following transfer, membranes were blocked in 4% skimmed milk powder in PBST (0.01% Tween-20) for 1 hour. Primary antibodies at an appropriate dilution were added in blocking buffer and incubated at room temperature for 1 hour or overnight at 4°C. Membranes were then washed in PBST 3 times and HRP-conjugated secondary antibody (if applicable) diluted in blocking buffer was added and incubated for 1 hour at room temperature. Detection was then performed, following a further 3 PBST washes, using Immobilon Western Chemiluminescent HRP Substrate (Millipore, P09718) in a Chemi-Imager (BioRad VersaDoc), or via an X-ray processor (Konica Minolta) (Towbin et al., 1979). Images were processed using ImageJ with densitometry used to compare band intensity between samples. Bands were outlined using the rectangle tool, with ctrl+1 to select the first lane, ctrl+2 to select subsequent lanes, and ctrl+3 to plot lanes. The straight-line tool was then used to define the bottom of the curve, and the wand tool used to measure the area as a proxy for band intensity.

For reuse of a blot where the expected band from the second blot was of a similar size to the first, the blot was stripped by incubating in stripping buffer for 1-2 hours followed by 5 PBST washes of 5-10 minutes. Following this the incubations were carried out as above.

All antibody incubations and washes were performed with shaking.

<u>2.7.4 Coomassie Staining</u>
For Coomassie staining, gels were incubated in Coomassie staining buffer for 1-2 hours followed by several washes in distaining buffer until bands were clearly visible and distinguishable from the background (Meyer and Lamberts, 1965). This usually consisted of 3-4 washes of 30 minutes each. An image of the resulting gel was then taken using the BIO RAD Gel Doc EZ Imager and Image Lab 5.2.1 software

2.8 Immunoprecipitation

Cell extracts were precleared on mouse IgG-Agarose beads (Sigma, A0919) for 1 hour at 4°C on a rotating wheel, 25μl of bead slurry was used per 0.5mg of protein. This was then centrifuged at 3000g for 3 minutes at 4°C and the resulting supernatant harvested.

A sample of the supernatant was aliquoted for western blot analysis as an "input" sample, the rest was divided between either mouse IgG-Agarose beads or Anti-V5 antibody-coupled agarose beads at a concentration of 0.5mg of protein per 25μl of slurry. This was then incubated overnight at 4°C on a rotating wheel.

Samples were then centrifuged at 3000g for 3 minutes at 4°C and the resulting supernatant removed. Bead pellets were then washed with PBS and pelleted, this process was repeated a further three times. After the final wash 4x NuPage LDS buffer (Invitrogen; NP0008) and 10x NuPage sample reducing agent (Invitrogen; NP004) were added in appropriate volumes and the samples were placed on a heat block at 90°C for 10 minutes before loading into gels for SDS-PAGE western blot analysis.

2.9 G:F Actin Ratio Assay

The G-actin/F-actin *In Vivo* Assay Kit (Cytoskeleton, BK037) was used to isolate G-actin and F-actin fractions following the instructions provided. Briefly, LAS2 lysis and F-actin stabilization buffer were added to cells and a cell scraper used to detach cells. Cells were homogenised using a 200μl pipette tip and incubated at 37°C for 10 minutes. This sample was then centrifuged to pellet cell debris and the resulting supernatant was removed into an ultracentrifuge tube. The sample was spun at 100,000g for 1 hour at 37°C, leaving an F-actin pellet and a G-actin supernatant, which was removed into another tube for analysis. The F-actin pellet was the resuspended in F-actin depolymerisation buffer (using the same volume as the volume of the initial sample). G-actin and F-actin samples were then analysed via SDS-PAGE western blotting.

2.10 *In Vivo* Analysis

2.10.1 *In vivo* electroporation

One hour before the electroporation procedure, mice (C3H/HeJ, 5-8 weeks old) were injected with 10µl of 0.4U/µl hyaluronidase (in 0.9% saline). DNA was diluted to 800-1200 ng/µl in ddH$_2$O and 10µl loaded into a sterile syringe. Mice were placed in an anesthetizing box with 4% isoflurane in O$_2$ supplied by an approved gas anaesthetic machine until deeply anaesthetised. Mice were then removed to a heating pad (37°C) and continually anesthetized with a rodent face mask. Toe pinch reflex was used to test the anaesthetic depth.

The extensor digitorum longus/ tibialis anterior (EDL/TA) muscles were chosen for these experiments as they are physically confined within the hindlimb and easy to access. 3mm wide electrodes were placed within the muscle and DNA injected between the electrode sites. Pulses were delivered using a NEPA21 machine (Nepagene, Japan). Three 50msec-long pulses at 100V, followed by three more pulses of the opposite polarity were administered to each injection site at a rate of one pulse per second (Titomirov et al., 1991).

Mice were sacrificed 7 days after the electroporation. Animals were sacrificed by a schedule one killing (cervical dislocation). All animal procedures have been carried with approval from the University of York Ethics committee and followed the UK Animals (Scientific Procedures) Act 1986 Amendment Regulations 2012, performed by under project licence PPL 70/6827 within an approved establishment (licence 5002510). EDL/TA muscles were dissected, fixed for 10 minutes in 4% PFA and snap frozen in liquid nitrogen-cooled isopentane and stored at -80C.

2.10.2 Immunofluorescence of mouse muscle sections

12micron longitudinal sections of muscle tissue were cut using a cryostat. Sections were permeabilised and blocked using 3% BSA in PBS + 0.3% Triton X100 for 1hr. Sections were then incubated overnight at 4°C with primary antibodies against COBL (Sigma, HPA019167 1:100) or α-actinin (abcam,

ab9465 1:100). Slides were washed in PBST and incubated for 2hrs with appropriate combinations of compatible secondary (either Alexa Fluor 488 goat anti-rabbit or goat anti-mouse, Invitrogen R37116/R37120) at RT in the dark before three washes with PBS for 5 minutes (Renshaw, 2016). Slides were mounted with Mowiol plus DAPI to stain nuclei and imaged using a Zeiss Upright 710 confocal microscope.

2.11 Polymerase Chain Reaction (PCR)
2.11.1 PCR
PCR reactions were typically prepared as follows:

- 15µl x2 PCR Master Mix (Thermo Scientific)

- 1µl 10µM forward primer

- 1µl 10µM reverse primer

- 1-2µl DNA

- Up to 30µl with PCR water (Thermo Scientific)

Reactions were performed on a Geneamp 9700 Thermocycler (applied biosystems) with reaction conditions adjusted according to the primers used and the expected product size.

2.11.2 Colony PCR
Colony PCR reactions were prepared as above. However, instead of DNA samples being added, a pipette tip containing cells from an individual *E. coli* colony was placed in each well and mixed, allowing the amplification of DNA from that colony. The tip was then used to inoculate a fresh colony on a new LB Agar plate (with appropriate antibiotic) and labelled for subsequent identification and use.

2.11.3 Agarose Gel Electrophoresis
Products were mixed with 6x DNA loading dye (NEB) and loaded on an agarose gel (agarose percentage dependent on the size of the DNA being

analysed) containing 1:10,000 V/V dilution of SYBR Safe DNA Gel Stain (Invitrogen, 10328162). Electrophoresis was performed using a BioRad power pack with a voltage of 50-100v dependent on the size of the DNA. Bands were then visualised using the EZ Gel Doc Imager (BioRad).

2.11.4 PCR Product Purification

Where required, excess primers, nucleotides, and enzymes were removed from PCR products using a PCR purification kit (Qiagen, 28106) as per manufacturer's instructions.

2.11.5 Sequencing

Sequencing of PCR products (and DNA plasmid constructs) was performed using the GATC Biotech Light Run sequencing service according to their instructions regarding sample and primer concentrations and volumes.

2.11.6 RNA Isolation and cDNA Conversion

Cells were incubated in an appropriate volume of TRIZOL (typically 300µl per well of a 6-well plate) at 50°C until homogenous. Chloroform (at an equal volume to that of TRIZOL) was then added, and the sample was shaken by hand before centrifugation (12,000g, 4°C, 15mins). The clear aqueous phase was then removed to a fresh tube and isopropanol added to precipitate RNA, followed by further centrifugation (12,000g, 4°C, 10mins) to pellet RNA. The RNA pellet was then washed twice with 70% ethanol, this was then dried and resuspended in DNAse/RNAse free water. RNA concentration and quality were then measured using the NanoDrop (Rio et al., 2010).

For conversion of RNA to cDNA the following reaction was set up:

4µl 5x ReadyScript Master Mix (Sigma, RDRT)

Xµl RNA (to give 1µg)

20-X-4µl RNAse/DNAse free water.

The reaction was then run in a thermocycler: 5mins 25°C, 30mins 40°C, 5mins 80°C, 4°C hold. Samples were kept on ice for immediate use of frozen at -80°C for long term storage.

2.11.7 qPCR
qPCR reactions were prepared as follows:

10µl 2X SYBR Green Fast qPCR Mix (Applied Biosciences, 4385612)

1µl each of forward and reverse primer (7µM)

1µl cDNA (or water for controls)

8µl PCR water

All reactions were performed in triplicate giving three technical replicates per biological sample. qPCR was performed on the QuantStudio 3 Real-Time PCR System (Applied Biosciences) using the standard fast protocol with melt curve analysis. Data was analysed using the DDCt method (Livak and Schmittgen, 2001) measuring target gene expression against a *Hprt* control.

2.12 Cloning
2.12.1 Transformation
Transformation of chemically competent *E. coli* was performed via heat-shock as follows. *E. coli* aliquots were thawed on ice prior to addition of plasmid DNA and incubation on ice for up to 30 minutes. Cells were then heat-shocked for 30 seconds at 42°C. S.O.C Medium (Thermofisher, 15544034) was then added, and the cells incubated at 37°C for 1 hour with shaking. Following incubation, cells were spread onto LB agar plates containing the relevant antibiotic (Froger and Hall, 2007).

2.12.2 Minipreps
Minipreps were performed using the QIAprep Spin Miniprep Kit (Qiagen, 27104) according to the manufacturer's instructions.

2.12.3 Gateway Cloning

The pENTR Directional TOPO Cloning Kit (Invitrogen, 25-0434) was used to clone COBL into Gateway vectors for mammalian expression. COBL was amplified from a mouse skeletal muscle cDNA library using primers designed to leave blunt-end PCR products with a 5' CACC to overlap with the GTGG overhang found on the pENTR TOPO Vector (see primer list and chapter 6.4 for more details). The cloning reaction was set up as outlined in the product manual and the resulting vector was transformed into One Shot chemically competent *E. coli* (Invitrogen, C4040-10). Colony PCR was performed to validate the resulting colonies followed by minipreps to isolate the desired plasmids.

An LR recombination reaction (recombination reaction between attL and attR sites) was used to shuttle the COBL from the entry vector into the desired Gateway destination vectors. Reactions were catalysed using LR Clonase II Enzyme Mix (Invitrogen, 11791-020) according to manufacturer's instructions. The resulting constructs were then transformed into One Shot chemically competent *E. coli* and validated through colony PCR as above.

2.12.4 NEBuilder High-Fidelity DNA Assembly Cloning

IGFN1 fragments were cloned into the pQE2-Im9 vector using the NEBuilder High-Fidelity DNA Assembly Cloning system (New England Biolabs, E5520S). The vector was cut using a double restriction digest, and IGFN1 fragments were amplified using primers that left complementary overhangs to the digest sites (see primer list 2.3 and chapter 5.4 for more details). The PCR product and digested vector were then assembled using the Assembly Master Mix according to manufacturer's instructions. The resulting vector was then transformed into One Sot chemically competent *E. coli* and validated through colony PCR as above.

2.13 Protein Expression and Purification

2.13.1 Protein Expression

Expression protocol optimisation is outlined in chapter 5. Typically, 15ml LB with the appropriate antibiotic was inoculated with a single colony of expression-competent *E. coli* and incubated in a shaker overnight at 37°C. 1ml of this culture was then used to inoculate 100ml warm LB with antibiotic and grown to and OD_{600} of 0.6, from here expression protocols differed as described in chapter 5. Samples were taken at various timepoints to validate protein expression, OD_{600} measurements were taken to allow for sample concentration equilibration prior to SDS-PAGE and Coomassie and/or western blot analysis.

2.13.2 Protein Purification

Protein was purified from bacterial cultures using the ProBond Purification System (Life Technologies, K850-01) under native conditions. Protein expression was performed, and cells harvested via centrifugation. The resulting pellets were resuspended in Native Binding Buffer with lysozyme (1mg/ml) and protease inhibitors (Sigma, P8849). Cells were then sonicated using six 10 second bursts with at least 10 seconds on ice between each burst. Lysates were the centrifuged at 10,000g for 15 minutes to remove cellular debris. Ni-NTA agarose beads (Invitrogen, R901-01) were equilibrated in Native Binding Buffer before adding the lysate and incubating for 1 hour with gentle agitation. Beads were then washed in Native Wash Buffer four times, and the sample collected in 1ml fractions using Native Elution Buffer.

2.13.3 Dialysis

Dialysis was performed using 14kDa BioDesignDialysis Tubing (Thermofisher, D011) which was soaked in ddH_2O and clipped at one end. Protein sample was the pipetted into the tube at the open end and clipped, avoiding leaving any bubbles. Filled tubing was then incubated, in the desired buffer, on a magnetic stirrer at 4°C overnight.

2.14 Pull-downs

IGFN1 fragments were expressed and purified as described above, with the protein left immobilised on the beads, and incubated with 1ml mouse skeletal muscle extract (3ml RIPA per 1g muscle tissue, described in 2.6.2) for 1 hour with gentle agitation. Beads were then washed in 8ml Native Wash Buffer four times and 12μl loaded directly onto a 10% Bis/Acrylamide gel. This was run until the dye front was ~1cm down the resolving gel. The lane was cut out and sent for LC-MS/MS analysis.

2.15 Thermal Unfolding

A Prometheus NT.48 Nano DSF with PR.ThermControl v2.1.2 software (NanoTemper) was used for thermal unfolding experiments. Experiments were performed with three technical replicates. Unfolding was performed from 15-95°C with a 1.3°C/min gradient. 350nm/330nm ratio first derivatives were calculated to reveal unfolding temperatures (Cieplak and Sulkowska, 2005).

2.16 Atomic Force Microscopy (AFM)

2.16.1 Cantilever Calibration

Tip C (predicted spring constant 0.01N/m) of an MLTC-Bio cantilever (BRUKER) was used for mechanical unfolding experiments. Touch calibration was performed with the EasyAlign probe holder using "peak force QNM in fluid" on a sapphire surface.

2.16.2 Mechanical Unfolding

Protein was loaded onto a Ni-NTA coated coverslip (attached to a slide via double-sided tape) before the addition of buffer (25mM Tris-HCl, 150mM NaCl, pH 7.4) to give a final protein concentration of 100μg/ml in a total of 150μl. This was incubated at room temperature for 10 minutes before washing with 300μl of buffer, and replacement of buffer on top of the coverslip held in place through surface tension. The coverslip was then placed into the AFM and experiments carried out using the "contact in fluid-FASTForce" program.

Parameters such as pulling speed and contact time contact time were adjusted accordingly.

2.17 Proteomic Analysis
Mass spectroscopy was performed by Adam Dowle at the University of York Department of Biology Technology Facility.

2.17.1 Digestion

In-gel tryptic digestion was performed after reduction with dithioerythritol and S-carbamidomethylation with iodoacetamide. Gel pieceswere washed two times with aqueous 50% (v:v) acetonitrile containing 25 mM ammonium bicarbonate, then once with acetonitrile and dried in a vacuum concentrator for 20 min. Sequencing-grade, modified porcine trypsin (Promega) was dissolved in 50 mM acetic acid, then diluted 5-fold with 25 mM ammonium bicarbonate to give a final trypsin concentration of 0.02 g/L. Gel pieces were rehydrated by adding 25 L of trypsin solution, and after 10 min enough 25 mM ammonium bicarbonate solution was added to cover the gel pieces. Digests were incubated overnight at 37°C. Peptides were extracted by washing three times with aqueous 50% (v:v) acetonitrile containing 0.1% (v:v) trifluoroacetic acid, before drying in a vacuum concentrator and reconstituting in 50 L of aqueous 0.1% (v:v) trifluoroacetic acid.

2.17.2 LC-MS/MS

Samples were loaded onto an UltiMate 3000 RSLCnano HPLC system (Thermo) equipped with a PepMap 100 Å C18, 5 µm trap column (300 µm x 5 mm Thermo) and a PepMap, 2 µm, 100 Å, C18 EasyNano nanocapillary column (75 m x 500 mm, Thermo). The trap wash solvent was aqueous 0.05% (v:v) trifluoroacetic acid and the trapping flow rate was 15 µL/min. The trap was washed for 3 min before switching flow to the capillary column. Separation used gradient elution of two solvents: solvent A, aqueous 1% (v:v) formic acid; solvent B, aqueous 80% (v:v) acetonitrile containing 1% (v:v)

formic acid. The flow rate for the capillary column was 300 nL/min and the column temperature was 30°C. The linear multi-step gradient profile was: 3-10% B over 7 mins, 10-35% B over 30 mins, 35-99% B over 5 mins and then proceeded to wash with 99% solvent B for 4 min. The column was returned to initial conditions and re-equilibrated for 15 min before subsequent injections.

The nanoLC system was interfaced with an Orbitrap Fusion hybrid mass spectrometer (Thermo) with an EasyNano ionisation source (Thermo). Positive ESI-MS and MS2 spectra were acquired using Xcalibur software (version 4.0, Thermo). Instrument source settings were: ion spray voltage, 1,900 V; sweep gas, 0 Arb; ion transfer tube temperature; 275°C. MS1 spectra were acquired in the Orbitrap with: 120,000 resolution, scan range: m/z 375-1,500; AGC target, 4e5; max fill time, 100 ms. Data dependant acquisition was performed in top speed mode using a fixed 1 s cycle, selecting the most intense precursors with charge states >1. Easy-IC was used for internal calibration. Dynamic exclusion was performed for 50 s post precursor selection and a minimum threshold for fragmentation was set at 5e3. MS2 spectra were acquired in the linear ion trap with: scan rate, turbo; quadrupole isolation, 1.6 m/z; activation type, HCD; activation energy: 32%; AGC target, 5e3; first mass, 110 m/z; max fill time, 100 ms. Acquisitions were arranged by Xcalibur to inject ions for all available parallelizable time.

Peak lists were converted from .raw to .mgf format using MSConvert (ProteoWizard 3.0.9974) before submitting to a locally-running copy of the Mascot program using Mascot Daemon (version 2.5.1, Matrix Science). Data were searched against the mouse and E. coli subsets of the UniProt database (39,956 sequences - 13 Oct 2017) with the following criteria specified: Enzyme, trypsin; Max missed cleavages, 2; Fixed modifications, Carbamidomethyl (C); Variable modifications, Oxidation (M), Deamidated (NQ), Gln->pyro-Glu (N-term Q), Glu->pyro-Glu (N-term E), Acetyl (Protein N-term) Peptide tolerance, 3 ppm (# 13C = 1); MS/MS tolerance, 0.5 Da; Instrument, ESI-TRAP. Mascot results in .dat format were imported into Scaffold (version Scaffold_4.8.4, Proteome Software Inc.) and a second

database search was performed using the X!Tandem engine with the same criteria specified. Search results were combined in Scaffold and peptide identifications were accepted if they could be established at greater than 86.0% probability to achieve an FDR less than 1.0% by the Scaffold Local FDR algorithm. Protein identifications were filtered to require a minimum of two unique identified peptides. Protein probabilities were assigned by the Protein Prophet algorithm (12). Proteins that contained similar peptides and could not be differentiated based on MS/MS analysis alone were grouped to satisfy the principles of parsimony. Proteins sharing significant peptide evidence were grouped into clusters.

Complete mass spectrometry data sets are available to download from MassIVE (MSV000083637, https://massive.ucsd.edu/ProteoSAFe/user/login.jsp?url=https%3A%2F%2F massive.ucsd.edu%2FProteoSAFe%2Fdataset.jsp%3Ftask%3D89d53176c6 c0446285d7365ea1027b1a) and ProteomeXchange (PXD013278, http://proteomecentral.proteomexchange.org/cgi/GetDataset?ID=PXD01327 8).

2.17.3 Statistical Rationale

Immunoprecipitations from three samples were analysed with three biological replicates. Samples comprised two regions of IGFN1 and were contrasted with LacZ, which was used as a negative control for non-specific binding. LC-MS/MS sample acquisition was randomised within biological replicate batches – i.e. all samples from biological replicate batch 1 were run before batch 2 but the order of IGFN1(d1-d3), IGFN11(d6-d11) and LacZ within each batch was changed each time. Samples were compared qualitatively using the following criteria. Acceptance of sample group protein identifications as significant to the pull-down required protein identification probability of greater than 95% in at least two of three biological replicates. Classification of protein absence from the pull-down required protein identification probability of less than 95% in all three biological replicates.

2.18 Statistical analysis

Statistical analysis of data was performed using SPSS (IBM). Data were tested for normality using the Shapiro-Wilk test. Unpaired two-tailed Student's t-tests were used for single comparisons and ANOVA for multiple comparisons with the Tukey HSD multiple comparison test for post-hoc identification of significantly different means. For co-localisation analysis, Pearson's correlation coefficient was calculated using Volocity software (Quorum Technologies), with the Costes method (Costes et al., 2004) used to set thresholds.

CHAPTER 3: CHARACTERISATION OF A FUSION AND DIFFERENTIATION DEFECT IN THE IGFN1 KNOCKOUT C1C12-DERIVED CELL LINE

Chapter 3: Characterisation of a Fusion Defect in the IGFN1 Knockout C1C12-derived Cell Line

3.1 Introduction

This chapter describes the characterisation of actin remodelling and fusion defects in an IGFN1 knockout myoblast cell line, originally produced by Li et al (Li et al., 2017).

Up to this point the functional role of IGFN1 in skeletal muscle has remained elusive. Interactions with KY and FLNC as well as with actin have been revealed and imply a role for IGFN1 at the z-disc (Baker et al., 2010). Knockdown of IGFN1 in C2C12 cells has previously been shown to result in decreased myoblast fusion as well as aberrant cell morphologies. However, these defects were never successfully rescued (Li et al., 2017). The domain composition of IGFN1 suggests a role in maintaining sarcomeric integrity under mechanical tension due to similarity with other proteins that perform this role (Otey et al., 2009), but until recently the tools to investigate the role of IGFN1 in any of these processes were not available.

The development of IGFN1 knockout myoblast cell lines using CRISPR/Cas9 technology, targeting exon 13 of IGFN1, provided a valuable tool to further evaluate the role of IGFN1 in skeletal muscle. Initially, to examine the role IGFN1 plays in cells undergoing mechanical tension, myoblasts were stretched in a cyclical manner, and morphological changes were to be measured. Instead of morphological changes, this led to the identification of an actin remodelling defect in knockout cells, and when differentiated these cells displayed similar fusion and morphology defects to those seen previously in IGFN1 knockdown cells. The role for IGFN1 in myoblast fusion was then further examined using several co-culture experiments and antibody staining of cells throughout differentiation.

3.2 Western Blot Confirmation of IGFN1 Knockout

The IGFN1 knockout cell line KO19 has previously been validated via qPCR, demonstrating significant reductions in IGFN1 expression (Li et al., 2017). To validate this knockout at protein level, SDS-PAGE western blots were performed, using antibodies raised against the C-terminus of IGFN1 (fig. 3.1A). Western blots revealed a complex band pattern (fig. 3.1B), as has been seen previously (Baker et al., 2010), rendering interpretation difficult. However, a band matching the molecular weight of IGFN1_V1 was observed to be consistently absent in samples from the knockout cell line, for all antibodies used. This band was always present in both skeletal muscle extracts, and wildtype C2C12 cells, for each antibody used. This confirms that the knockout of at least the IGFN1_V1 isoform was successful.
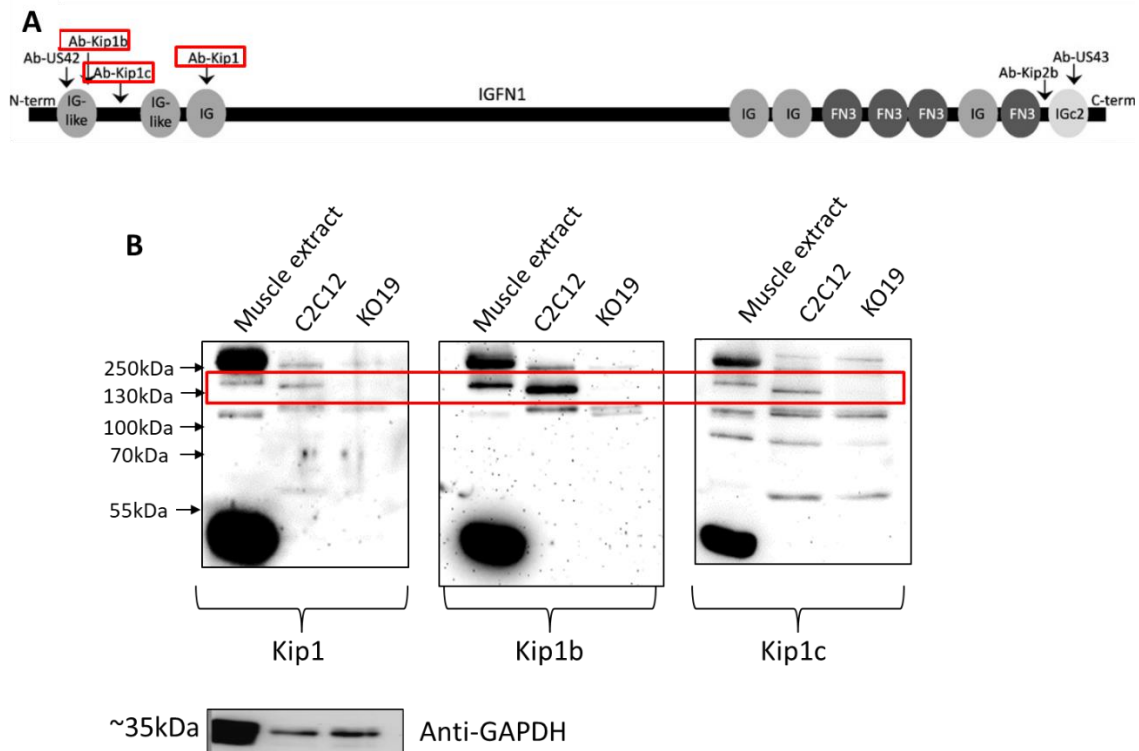
Figure 3.1. IGFN1_V1 is not present in IGFN1 knockout cells. A) *Representation of full-length IGFN1 and the region to which the given polyclonal antibodies bind highlighted in red boxes (adapted from (Baker, et al. 2010)).* **B)** *Top: western blots against IGFN1 using the antibodies in A on samples from a wildtype skeletal muscle extract, wildtype cells (C2C12) and IGFN1 knockout cells (KO19), a complex pattern of bands is seen, with at least one band missing in the knockout cell line. The absence of a band at ~135kDa (red box) likely represents the loss of the IGFN1_V1 isoform in the KO19 cell line. Bottom: loading control against GAPDH showing equal loading of the two cell extracts.*

3.3 IGFN1 Knockout Cells Display Altered Actin Remodelling

It was initially hypothesised, due to the localisation of IGFN1 to the z-disc, and its similar domain composition to a number of sarcomeric structural proteins, that IGFN1 may play a role in maintaining sarcomeric structure during contraction and relaxation cycles. In order to investigate this, wildtype, and two IGFN1 knockout C2C12 cells lines (KO19 and KO33) were subjected to mechanical stretching using the FlexCell system (Materials and Methods 2.4.6 for details). Cells were stained with phalloidin and imaged to allow for changes in cell size or morphology to be measured (fig. 3.2A).

No changes in cell size or morphology were observed either between cell lines or between stretched and non-stretched cells (data not shown). However, it was observed that wildtype cells after stretching appeared to show more intense fluorescence from phalloidin staining, reflecting an increase in actin polymerisation. This affect was not observed in either knockout cell line. In order to quantify this effect, cells were imaged using a confocal microscope with identical settings between samples. ImageJ was then used to measure fluorescence of individual cells, normalised to background fluorescence. Quantification revealed an increase in fluorescence following stretching in wildtype cells, while knockout cells showed either a reduction in fluorescence (KO19) or no change (KO33) (fig. 3.2A and B). This result indicated that actin polymerisation in response to mechanical tension is diminished in knockout myoblasts.
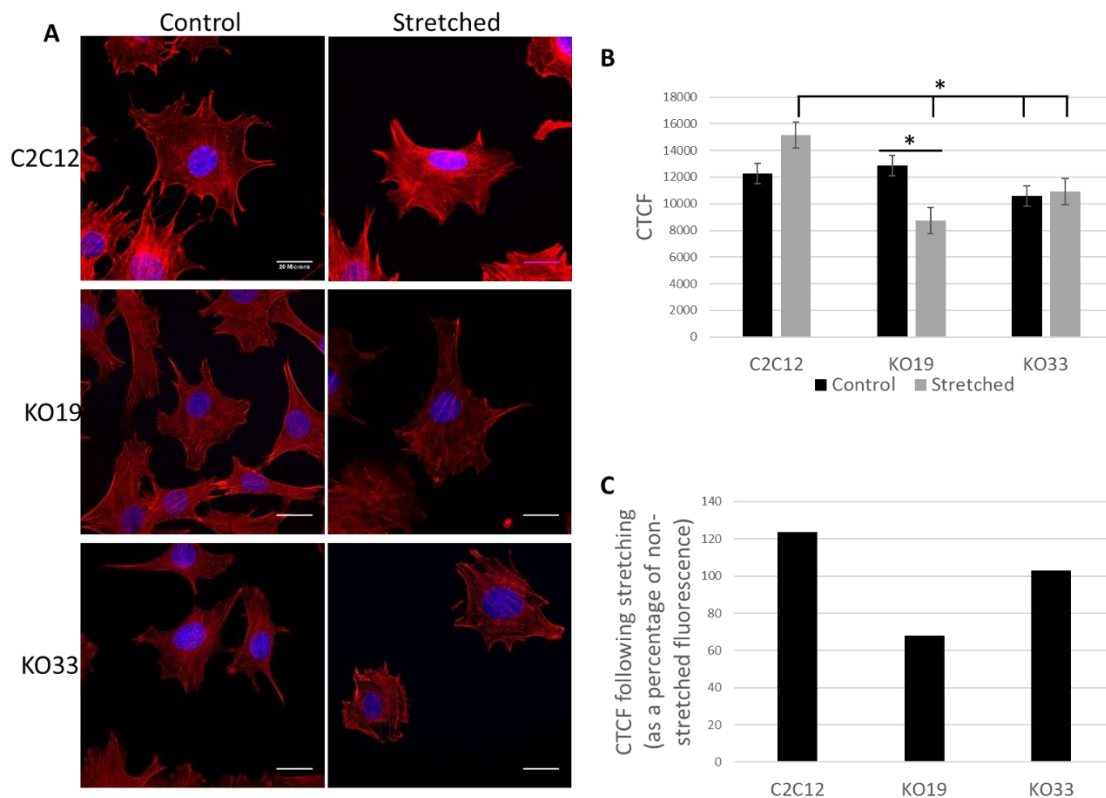
Figure 3.2. The actin cytoskeleton of proliferating wildtype and IGFN1 knockout cells show different responses to mechanical tension. A) *Representative confocal slices of phalloidin (polymerised actin) and DAPI (nuclear) stained proliferating wildtype (C2C12) and IGFN1 knockout cell lines (KO19 and KO33) without or without mechanical stretching (control or stretched, respectively) being applied (2hrs, 1.3Hz, 10%).* ***B)*** *Quantification of mean* Corrected total cell fluorescence (CTCF) *in each cell line in either stretched or non-stretched cells, n≥70. One-way ANOVA revealed there was a significant effect of cell type and condition on fluorescence at the p<0.01 level [F(5, 499)=11.77, p<0.01]. Post-hoc comparisons using the Tukey HSD test revealed a significant difference between the mean CTCF of KO19 control and stretched cells, and between C2C12 stretched cells and KO19 stretched cells, KO33 control cells, and KO33 stretched cells (*p<0.01). Error bars represent standard error.* ***C)*** *Mean CTCF following stretching as a percentage of mean CTCF of control cells.*

A similar experimental protocol was to be followed in differentiated myotubes in both wildtype and knockout cell lines, to give a more accurate reflection of actin dynamics in skeletal muscle. It was observed that differentiated knockout cells display a distinct morphology from wildtype cells, which is explored in detail below. While knockout cells appeared to display lower overall phalloidin fluorescence, this approach was not viable. It was not possible to distinguish between individual cells due to cells being in contact or overlapping, especially in wildtype samples, meaning any analysis of phalloidin intensity would be unreliable (fig. 3.3).
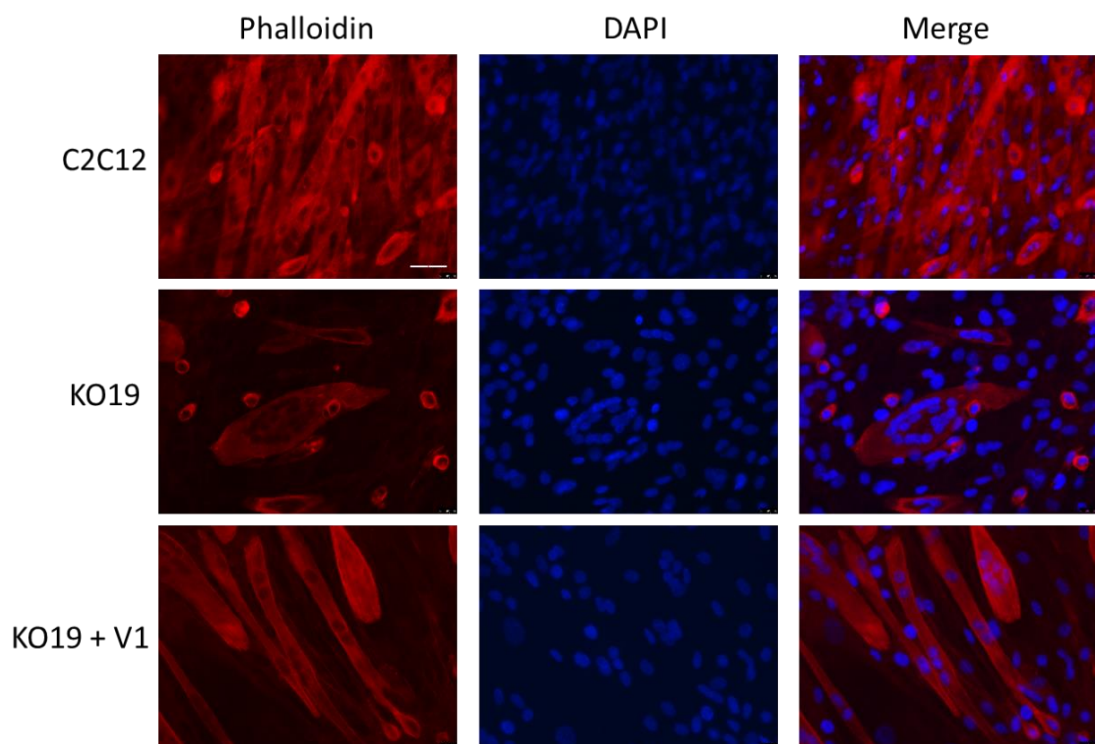
Figure 3.3. Individual differentiated myoblasts stained with phalloidin cannot be distinguished. *Representative widefield images of phalloidin-stained cells following 7 days of differentiation. Cells lines shown are wildtype (C2C12), IGFN1 knockout (KO19) and KO19 stably expressing IGFN1_V1 (KO19+V1). Scale bar=100 microns.*

Because actin polymerisation could not be accurately measured through phalloidin staining of differentiated cells, the ratio of globular actin (G-actin) and filamentous actin (F-actin) in C2C12, KO19 (IGFN1 deficient) and KO19+V1 (KO19 stably transfected with IGFN1_V1-tdTomato) cells was examined using SDS-PAGE western blotting. For these experiments, cells were maintained in differentiation medium (DM) for 7 days. After 7 days in DM, both G-actin and F-actin were detected in all cell lines following the protocol described in Materials and Methods 2.9 (fig. 3.4A). Quantifications from several independently generated blots (n=8) showed a significant G:F actin ratio increase in KO19 cells (Fig. 3.4B). A trend towards rescuing this defect was observed in the KO19+V1 cell line (fig. 3.4A and B). The three cell lines showed similar levels of expression of total actin relative to GAPDH (fig 3.4C), indicating that higher G:F actin ratios in the KO19 cells were not caused by actin expression levels but from lower polymerization activity. It would thus appear that IGFN1_V1 contributes positively to the actin polymerization activity in C2C12 cells.

Stretching of differentiated cells was attempted to measure the effect of mechanical tension on G:F actin ratio in differentiated cells. However, differentiated cells detached from the base of the plates when stretching was applied. Coating of the plates with collagen was attempted to increase adherence but this proved unsuccessful.
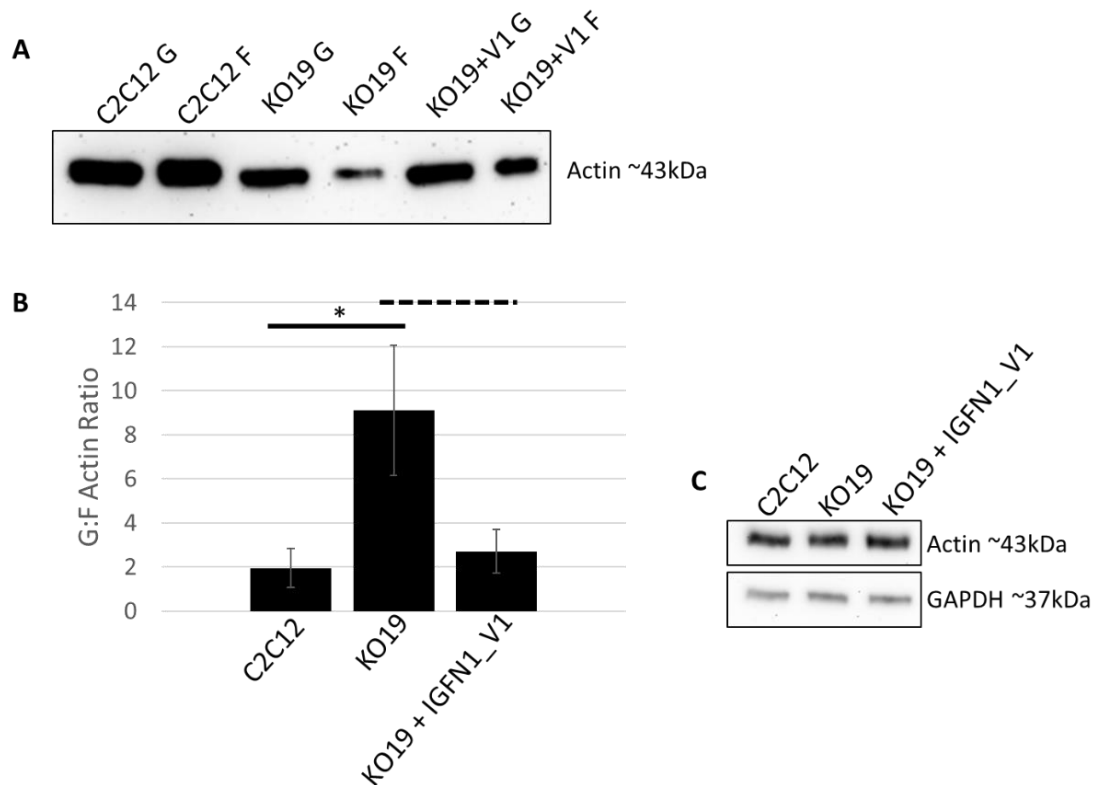
Figure 3.4. IGFN1 knockout cells have a higher G:F actin ratio than wildtype which can be rescued through IGFN1_V1 expression. A) SDS-PAGE western blot against actin from globular (G) or filamentous (F) actin fractions of 7 day differentiated wildtype (C2C12), IGFN1 knockout (KO19) and rescue (KO19+IGFN1_V1) cells. B) G:F actin ratio of C2C12, KO19 and KO19+v1 (n=8). One-way ANOVA was performed, there was a significant effect of cell type at the p<0.05 level [F(2, 22) = 4.665, p = 0.02]. Post-hoc comparisons using the Tukey HSD test revealed a significant difference between the mean G:F ratio of C2C12 and KO19 cells (p<0.05) and a close to significant difference between KO19 and KO19+v1 cells (p=0.056). Error bars represent standard error. C) Confirmation via western blotting that total actin in all cell types is similar (top), using GAPDH as a loading control (bottom).

3.4 IGFN1 Knockout Cells Display a Fusion and Differentiation Defect

A distinct morphology in IGFN1 knockout cells was observed in figure 3.3. To quantify these changes the fusion index, differentiation index, and myotube diameter were calculated in differentiated wildtype, IGFN1 knockout, and IGFN1_V1 rescued cells (fig 3.5). Cells were stained with an anti-α-actinin antibody in order to identify differentiating cells.

To compare the size of multinucleated structures the diameter of cells containing three or more nuclei was measured in images from C2C12 and KO19 cells (fig 3.5A). A value of three or more nuclei was chosen to distinguish between myotubes originated from multiple fusion events from cells undergoing division. KO19 multinucleated cells have a significantly larger mean diameter than C2C12 myotubes (fig 3.5D), indicating that disruption of *Igfn1* exon 13 causes loss of cell size control in differentiating cells. The differentiation index was quantified by calculating the proportion of nuclei within an α-actinin positive structure to the total number of nuclei in a given field. This value was significantly lower in the KO19 cell line (fig 3.5B), indicating a delay in expression of the differentiation programme. This was also the case when measuring the fusion index, expressed as the percentage of α-actinin positive cells with three or more nuclei to the total number of cells expressing α-actinin. The data showed a significantly lower fusion index in KO19 cell line (fig 3.5C). Thus, KO19 shows reduced fusion, reduced differentiation and larger multinucleated structures.

To test whether the above phenotypes are caused by disruption of *Igfn1* exon 13, and not the result of an off target genetic disruption, a construct coding for recombinant IGFN1_V1-tdTomato (pDEST47_IGFN1_V1_tdTomato) was transfected into the KO19 cell line. Transfected cells were selected by G418 treatment and the mixed resulting population was evaluated for size of multinucleated structures, differentiation index and fusion index, as above. The overall morphology of these cells appeared more like that of the C2C12s (fig 3.5A) and quantifications demonstrated partial but significant rescue of fusion and differentiation defects in the KO19 transfected cells (fig 3.5B–D). Therefore IGFN1_V1 plays a critical role in myoblast fusion and differentiation *in vitro*.
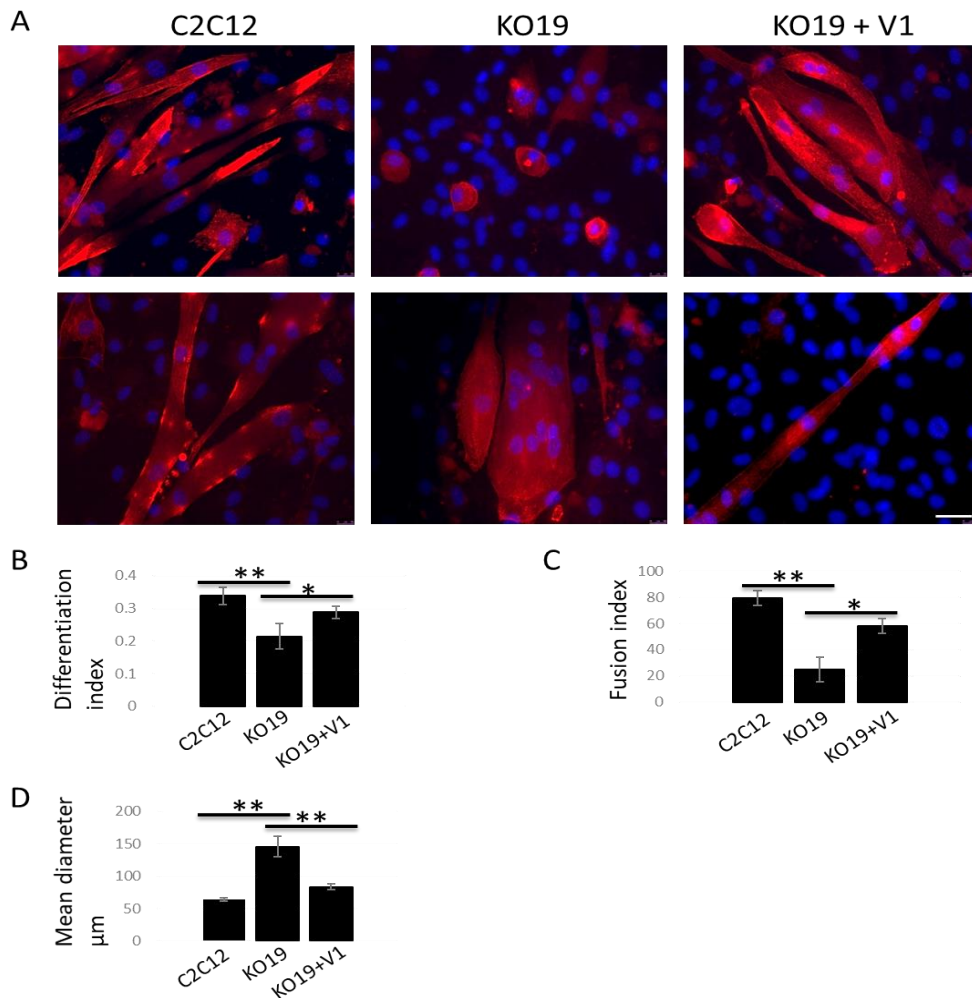
Figure 3.5. The KO19 cell line displays fusion and differentiation defects partially rescued by expression of IGFN1_V1. A) *Representative widefield fluorescence images of myoblasts differentiated for 10 days for C2C12, KO19 and KO19 transfected with IGFN1_V1 coding plasmid (KO19+V1). Cells were stained for α-actinin (red) and DAPI (blue). Two examples per cell line shown, as labelled. Scale bar represents 50μm.* ***B)*** *Differentiation index for the indicated cell lines, calculated as the proportion of nuclei within an α-actinin expressing cell to the total number of nuclei within the same field. Note that KO19 cells have a significantly lower differentiation index than wildtype and rescued cells. (n=35)* ***C)*** *Fusion index calculated as the percentage of α-actinin positive cells with three or more nuclei. KO19 cells have significantly lower fusion index than wildtype and rescued cells. (n=35)* ***D)*** *Mean diameter of α-actinin positive cells containing three or more nuclei, average diameter is significantly higher in knockout cells compared to both the wildtype and the rescue (n=40). (**) p<0.01, (*) p<0.05.(Li et al., 2017). Error bars show standard error.*

3.5. IGFN1 Knockout Myoblasts Migrate and Proliferate Normally

As well as myoblast fusion and differentiation, cell migration and proliferation rely heavily on actin remodelling. To assess whether changes to the actin cytoskeleton specifically affect myoblast fusion and differentiation, and not these other processes, a scratch wound assay was performed (fig 3.6). Cells were grown to 100% confluency before the application of a wound using pipette tip, cells were imaged immediately and at six hours post scratch wound (fig 3.6A). No significant changes in wound closure at six hours were observed (fig3.6B) indicating equivalent rates of proliferation and migration in both wildtype and IGFN1 knockout cell lines. Thus, IGFN1 does not play a role in cell migration or proliferation, and the observed changes to the actin cytoskeleton specifically affect myoblast fusion and differentiation.
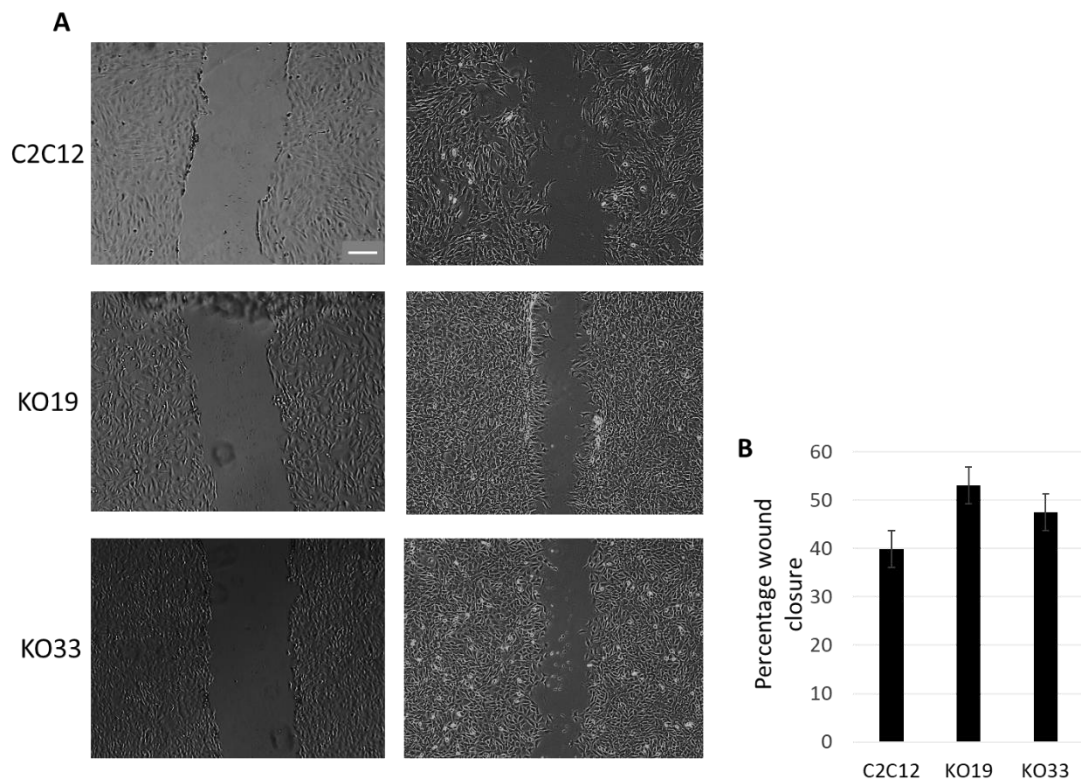
Figure 3.6. Scratch wound assay suggesting migration and proliferation of IGFN1 knockout cells is unaffected. A) *Images of wildtype cells (C2C12) and two IGFN1 knockout cell lines (KO19 and KO33) immediately following scratch wound application (left) and 6 hours post scratch wound application (right). Scale bar represents 500 microns.* ***B)*** *Mean wound closure from 5 wells per cell type, three measurements were taken for each well and an average calculated. One-way ANOVA revealed there was no significant effect of cell type on wound closure [F(2,9)=3.49, p=0.078]. Error bars show standard error.*

3.5 Co-culture of Wildtype and IGFN1 Knockout Cells Leads to Fusion

To further examine the role of IGFN1 in myoblast fusion a co-culture experiment was designed, to determine whether IGFN1 was required in both cells for fusion to occur. Wildtype C2C12 cells were transfected with pDEST47-tdTomato, and IGFN1 knockout cells were transfected with pMax GFP. The transfected cells were seeded together in equal numbers to 100% confluency before growth media was replaced with differentiation media for 3 days (fig 3.7A). Multiple cells were observed to express both pDEST47-

tdTomato and pMax-GFP, demonstrating fusion between wildtype and IGFN1 knockout cells. Additionally, these cells appeared to have morphologies comparable to those of wildtype myotubes. Therefore, IGFN1 is only required on one of two fusing myoblasts for fusion to occur, and the morphology observed in IGFN1 knockout cells following fusion can be rescued by the fusion of a wildtype cell.
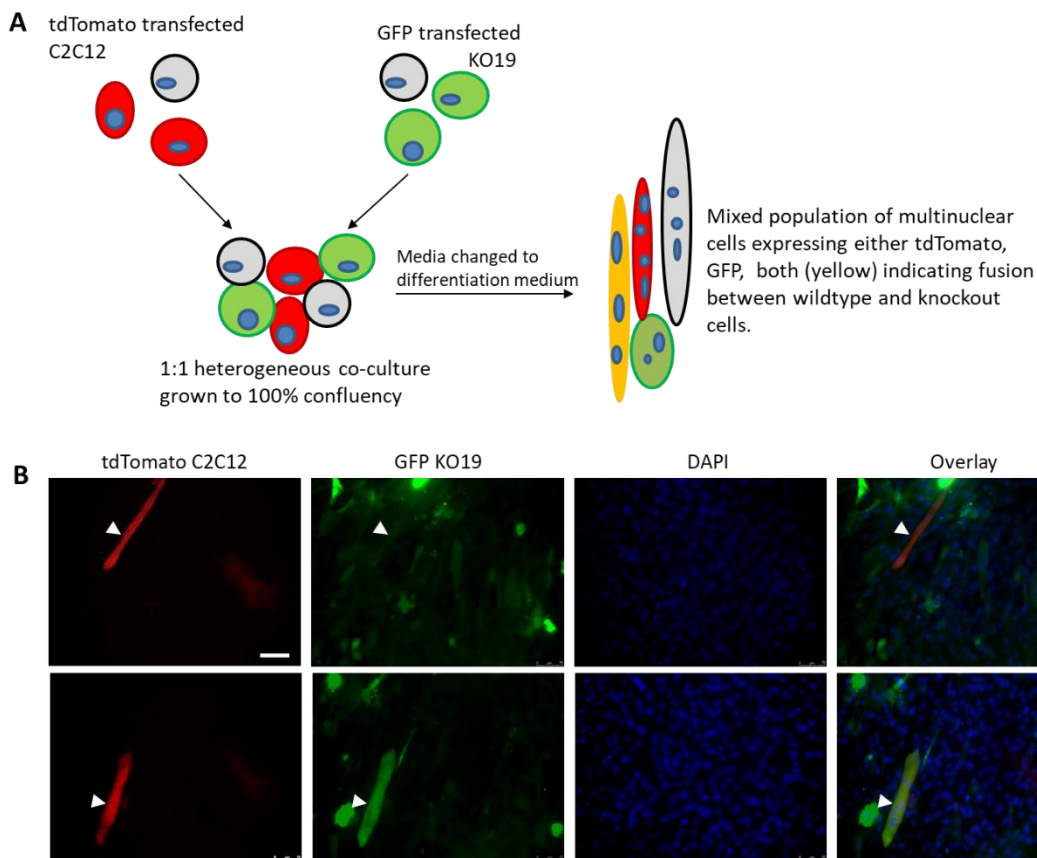
Figure 3.7. Co-culture of Wildtype and IGFN1 Knockout Cells Leads to Fusion.
A) *Schematic of experimental design for co-culture experiments. It should be noted that transfections were not 100% efficient, indicated by cells in grey, meaning that it is possible that there was a much higher incidence of fusion between cell types than it appears.* **B) Widefield** *images of wildtype (C2C12) cells transfected with pDEST47-tdTomato and knockout cells (KO19) transfected with pMax-GFP, grown in a 1:1 co-culture and differentiated for 3 days. Arrowheads indicate myotubes expressing both Td-tomato and GFP. Scale bar represents 75 microns.*

3.6 IGFN1_V1 is Not Sufficient to Induce Fusion Between 3T3 Cells

The recent identification of myomaker and myomerger as "fusogens" are the first examples of muscle-specific proteins able to induce fusion between non-muscle cells (Millay et al., 2016; Millay et al., 2013; Zhang et al., 2017). Due to IGFN1 being implicated in myoblast fusion it was important to determine whether it could elicit similar activity as the fusogens. To this end, a similar experimental model was used as was used for myomaker and myomerger.

Initially, 3T3 cells were transfected with either pDEST47-tdTomato or pDEST47-IGFN1_V1-tdTomato, before being grown in differentiation media for 3 days. Cells were fixed and imaged after 3 days (fig. 3.8A). No examples of fusion between 3T3 cells were observed in either condition. Thus, IGFN1_V1 is not sufficient to drive fusion between two non-muscle cells. Next it was determined whether IGFN1_V1 was sufficient to induce fusion between a non-muscle cell and a myoblast. C2C12 cells were transfected with pMax-GFP and 3T3 cells were transfected with pDEST47-IGFN1_V1-tdTomato. The transfected cells were seeded together in equal numbers, before growth media was replaced with differentiation media for 3 days. Again, no fusion was observed between transfected C2C12 and 3T3 cells (fig. 3.8B). These results show that IGFN1_V1 is not sufficient to induce fusion in a non-muscle cell type.
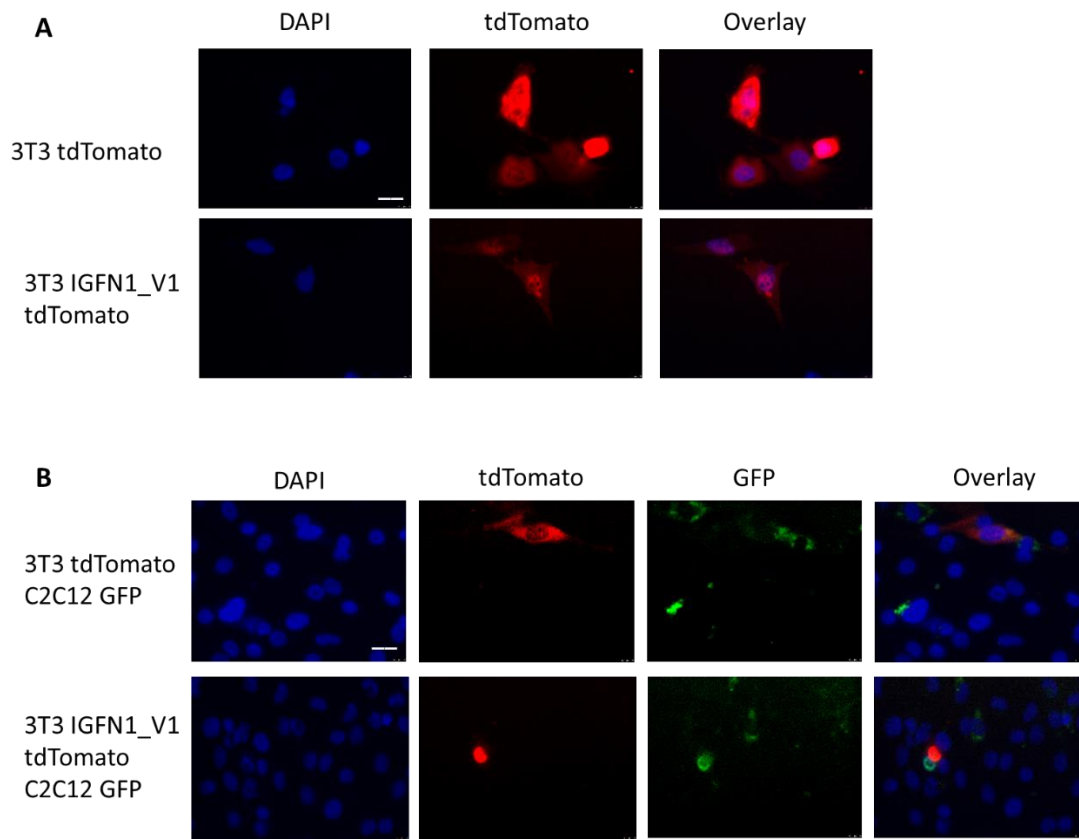
Figure 3.8. IGFN1_V1 expression is not sufficient to induce fusion of non-muscle fibroblasts. A) *Representative widefield images of 3T3 cells transfected with either tdTomato or IGFN1_V1 tdTomato and induced to differentiate for 3 days, no examples of fusion were observed.* **B)** *Representative images of 3T3 cells transfected with either tdTomato or IGFN1_V1 tdTomato, grown in co-culture with C2C12 cells transfected with GFP and induced to differentiate for 3 days. No examples of fusion involving 3T3 cells were observed. For both A and B a minimum of 3 wells of a 6-well plate were observed for each condition. Scale bars represent 50µm.*

3.7 IGFN1 Localisation Throughout Differentiation

The localisation of IGFN1 was tracked, via antibody staining, at numerous time points throughout differentiation. Staining at days 1,2,3, and 10 following the change of growth media to differentiation media was performed (fig. 3.9). During days 1-3 cells that appear to be undergoing fusion show higher IGFN1 expression. At day 10 IGFN1 was shown to clearly localise along the edge of cells fusing to a myotube. It should be noted that observation of this was relatively rare, possibly due to the transient, temporal nature of myoblast fusion.
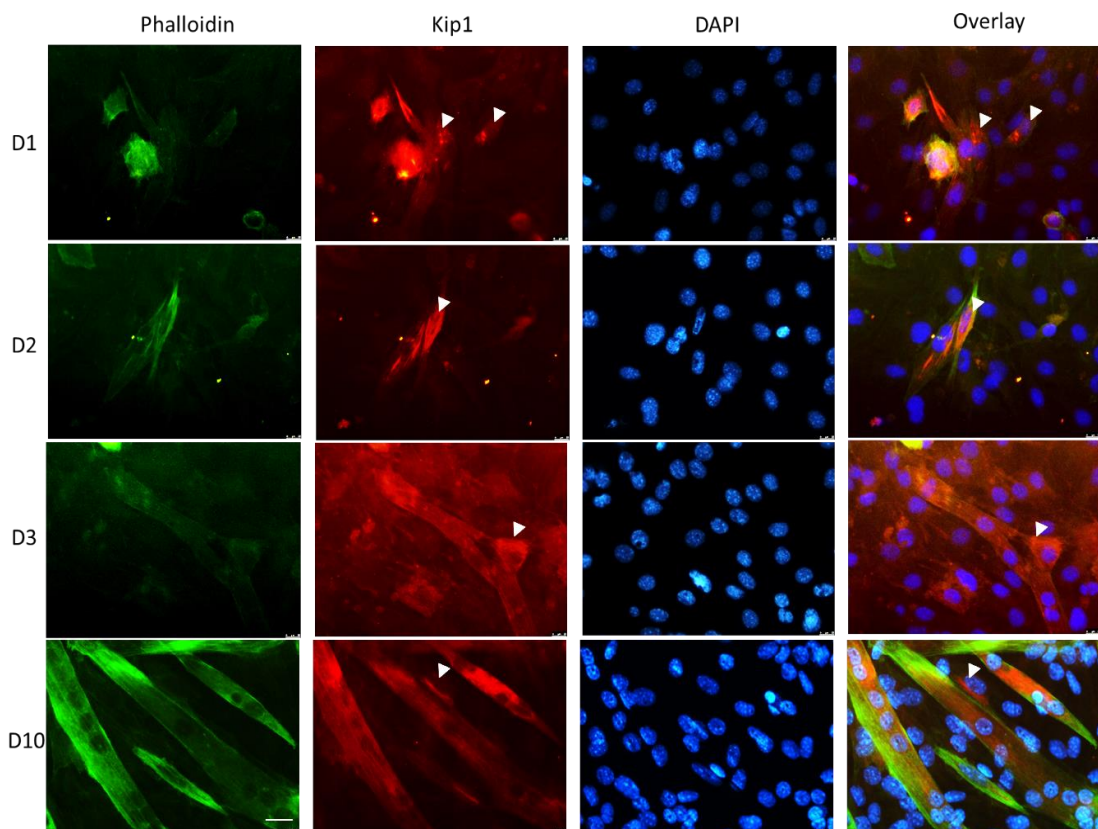
Figure 3.9. IGFN1 expression localisation throughout differentiation. Widefield images of wildtype C2C12 myotubes (1,2,3 and 10 days differentiated) stained with phalloidin against actin (green) and Kip1 against IGFN1 (red). Arrowheads indicate cells with high IGFN1 expression which appear to be undergoing fusion. Exposure was adjusted so that myotubes were more clearly visible. Scale bar represents 50 microns.

3.9 Conclusions

The CRISPR/Cas9-generated, C2C12-derived, IGFN1 knockout cell line used in this chapter had previously been validated via qPCR (Li et al., 2017). However, no protein-level analysis had been performed. Western blots demonstrated a complex banding pattern from IGFN1 antibodies, as was expected based on previous work using these antibodies (Baker et al., 2010). The IGFN1 locus is complex and produces multiple isoforms from multiple promoter regions. As well as this, there is evidence that IGFN1 fragments tend to show different than expected molecular weights when analysed by SDS-PAGE and western blot detection, possibly due to dimerization or aggregation. However, the consistent absence of at least one IGFN1 isoform (most likely IGFN1_V1, based on its molecular weight) was demonstrated.

Initial investigation of the effects of IGFN1 knockout in C2C12 cells was to examine the morphological changes in these cells compared to wild-type cells, especially under mechanical tension. While no morphological changes were observed, because phalloidin staining was used for the imaging of cells, changes in the actin cytoskeleton could be observed. Mechanical tension resulted in increased fluorescence of phalloidin staining in wild-type cells. This effect was not observed in knockout cells, with cells showing either reduced phalloidin staining or no change in response to mechanical tension. This suggested that IGFN1 may play a role in actin polymerisation in response to mechanical load. This warranted further investigation due to the previously observed interaction between IGFN1 and actin, and the localisation of IGFN1 to the z-disc, a sarcomeric region which undergoes a large amount of mechanical load (Baker et al., 2010).

Similar experiments could not be performed in differentiated cells, due to cells detaching from the growth surface under tension. However, a western blot assay could be used which demonstrated lower levels of actin polymerisation, even in the absence of mechanical tension, in IGFN1 knockout cells. Examination of these differentiated cells revealed significant fusion and differentiation defects, as well as significant morphological changes in IGFN1 knockout cells. These phenotypes were then at least partially rescued through

expression of IGFN1_V1, the isoform confirmed to be knocked out. These results imply that IGFN1 is involved in both the remodelling of the actin cytoskeleton, and in myoblast fusion and differentiation, two processes that significantly interact with one another (Rochlin et al., 2010). Therefore, it is possible that IGFN1 influences myoblast fusion and differentiation through the remodelling of the actin cytoskeleton.

The fact that a wildtype cell and an IGFN1 knockout cell are able to fuse demonstrates that only one of the fusing cells requires IGFN1. This implies that IGFN1 does not act symmetrically and is either required in the fusing myoblast, or in the myotube during fusion, but not in both. IGFN1 antibody staining of myoblasts undergoing differentiation demonstrated increased expression of IGFN1 localised to the site of contact between the on the fusing myoblast and the myotube, within the fusing myoblast. It is therefore likely that any requirement for IGFN1 in myoblast fusion is performed in this cell rather than in the myotube. Similar asymmetry has been observed with myomerger with efficient fusion requiring myomaker expression in both fusing cells but myomerger in only one fusing cell (Quinn et al., 2017). When fusion did occur between wildtype and knockout cells the observed myotubes appeared morphologically normal, demonstrating the rescue of the IGFN1 knockout phenotype via IGFN1 expression from the wildtype nucleus.

It could not be shown that IGFN1 displays any fusogenic activity. IGFN1 was unable to induce fusion between two non-muscle cells or between a muscle and non-muscle cell. Such activity has been observed with the membrane-bound fusogens myomaker and myomerger, which play a direct role in myoblast fusion. Therefore, the role of IGFN1 in myoblast fusion is likely to be indirect, possibly through interaction with other effector proteins. The structure of IGFN1 supports this, it lacks any predicted catalytic domains, and contains globular domains often involved in protein-protein interactions. It is possible that IGFN1 regulates myoblast fusion, through changes to the actin cytoskeleton, via interactions with other proteins.

In summary, IGFN1 knockout myoblasts display altered actin remodelling dynamics, both in response to mechanical load, and during myoblast fusion and differentiation. As well as this, IGFN1 knockout myoblasts display a fusion and differentiation defect, and morphological changes which can be rescued through the expression of IGFN1_V1. While it appears that IGFN1 is required for normal myoblast fusion, IGFN1 is not sufficient to drive fusion between non-muscle cells or between a muscle cell and a non-muscle cell. Finally, it appears that IGFN1 is required in the fusing myoblast, rather than in the myotube during fusion.

CHAPTER 4: IGFN1 AND ATROPHY

Chapter 4: IGFN1 and Atrophy

4.1 Introduction

The goal of the research presented in this chapter was to examine any role for IGFN1 in skeletal muscle atrophy using IGFN1 knockout and IGFN1 overexpressing C2C12-derived myoblast cell lines.

IGFN1 expression is associated with increases in atrophic signals, and denervation of a muscle fibre is a common model for muscle fibre atrophy in vivo (Pellegrino and Franzini, 1963). Mansilla et al (Mansilla et al., 2008) found that denervation-induced atrophy is accompanied by an increase in transcription of IGFN1. As well as this, IGFN1 expression is positively correlated with myostatin signalling. Evidence for this comes from gene expression analysis whereby myostatin signalling was downregulated in mice, using soluble activin type B receptors (ActRIIB) to sequester myostatin. As expected, muscle mass increased, this was also associated with changes in the expression of many genes. IGFN1 expression was found to be significantly reduced (Rahimov et al., 2011). The opposite is also true, when myostatin signalling is increased, via injection of adenoviral vectors in mice, muscle mass decreases and IGFN1 expression increases (Chen et al., 2014). This raises the possibility that IGFN1 is involved in atrophy, specifically as an effector of the myostatin pathway.

The glucocorticoid dexamethasone is often used to induce atrophy in myotubes in vitro (Menconi et al., 2008; Qin et al., 2013; Raffaello et al., 2010; Xu et al., 2013). Dexamethasone results in the upregulation of myostatin expression, at least partially through interaction with GRE (glucocorticoid response elements) within the promoter of myostatin (Qin et al., 2013).

Dexamethasone was used in this chapter to induce myostatin expression and, as a consequence, atrophy in differentiated cells. The atrophic response of wildtype, IGFN1 knockout, and IGFN1 overexpressing cells was analysed. Further, IGFN1 expression levels in response to dexamethasone treatment were measured by SDS-PAGE western blot analysis.

4.2 Dexamethasone Induces Atrophy in Differentiated Wildtype Myotubes but not in IGFN1 Knockout Cells

A range of concentrations from 100nM to 100μM (Menconi et al., 2008; Xu et al., 2013) of dexamethasone have previously been reported to induce atrophy in differentiated myotubes. Because of this, a dose response experiment was performed to determine the concentration required to induce atrophy in myotubes, in both wildtype and IGFN1 knockout cells. Myotubes were differentiated for 7 days before dexamethasone was added to the media for 3 days. Cells were imaged, and their diameters measured, both before the addition of dexamethasone, and after 3 days of dexamethasone treatment.

In wildtype cells, as dexamethasone concentration increased, the hypertrophy observed between days 0 and 3 decreased. The highest concentration of dexamethasone (100μM) resulted in atrophy of wildtype C2C12-derived myotubes. This effect was not observed in the IGFN1 knockout myotubes, where myotube size remained relatively constant throughout the experiments for all dexamethasone concentrations (fig 4.1). However, this may have been confounded by the fusion and differentiation defects, and morphological differences between wildtype and knockout cells discussed in chapter 3.These differences made consistent, like-for-like measurements of the knockout cells difficult compared to the wildtype cells which had a regular morphology. Because of this, it was determined that the IGFN1 knockout cells were not a viable tool for investigating the role of IGFN1 in atrophy, and that overexpression of IGFN1 may prove a more insightful experiment.
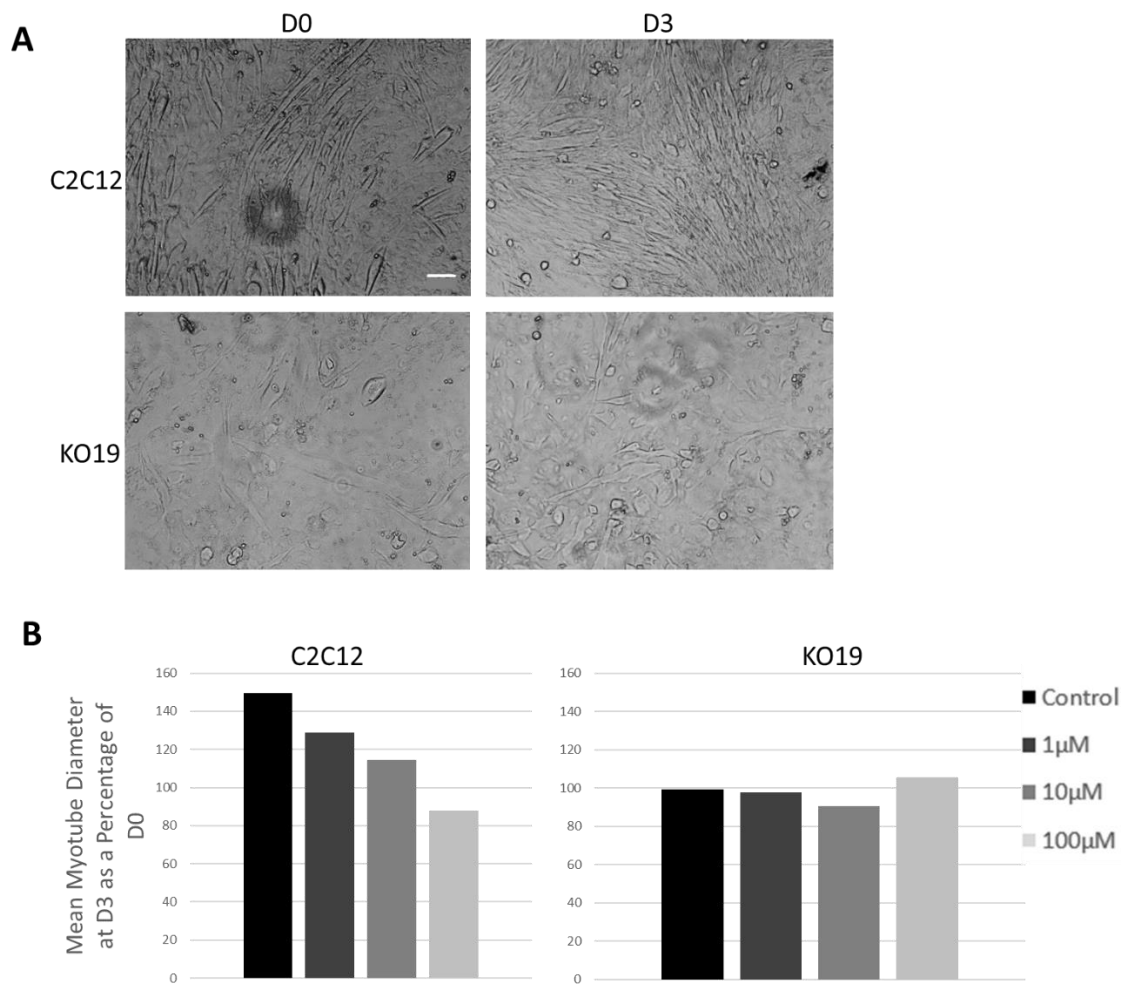
Figure 4.1. Dexamethasone treatment induces atrophy in wildtype myotubes but not in IGFN1 knockout cells. A) *Representative images of cells after 7 days of differentiation at D0 (before dexamethasone addition) and D3 (following 3 days of 100µM dexamethasone treatment). Examples are shown for both wildtype (C2C12) and IGFN1 knockout cells (KO19). Scale bar represents 200 microns.* ***B)*** *Quantification of percentage change in average myotube diameter after 3 days treatment with varying concentrations of dexamethasone. Concentrations given in µM. Min of 50 myotubes measured for each condition.*

4.3 Overexpression of IGFN1_V1 Does Not Result in Myotube Size Decreases

To determine whether IGFN1 overexpression would lead to myotube size decreases, a cell line overexpressing IGFN1_V1 was generated. Wildtype C2C12 cells were transfected with pDEST47-IGFN1_V1-tdTomato, followed by en masse selection with puromycin. pDEST47-IGFN1_V1-tdTomato expression was confirmed through observation of red fluorescence. The resulting cell line was differentiated for 7 days alongside wildtype cells. After 7 days the cells were fixed and stained using an antibody against α-actinin. The diameter of the resulting α-actinin positive cells was measured. It was found that there was a small, non-significant, decrease in diameter in the IGFN1_V1 overexpressing cell line, suggesting IGFN1 is not sufficient to induce atrophy in myotubes (fig. 4.2).

Due to the above, it was hypothesised that IGFN1 may only contribute to myotube atrophy when an upstream signal is present. Therefore, IGFN1 overexpression may exacerbate the atrophy induced by dexamethasone treatment. To test this, wildtype and IGFN1 overexpressing cells were differentiated for 7 days, followed by 3 days of either 100μM dexamethasone treatment or control treatment, as in figure 4.1. Cells were imaged, and their diameters measured before and after treatment. As in figure 4.1, untreated myotubes underwent hypertrophy over the 3 days, this was observed in both cell types, suggesting that overexpression of IGFN1_v1 is not sufficient to stunt hypertrophy. On top of this, in the presence of dexamethasone, both cell types atrophied to a similar extent (fig.4.3). These data indicate that in vitro IGFN1 is not sufficient to induce atrophy, or stunt hypertrophy, nor does IGFN1 overexpression exacerbate atrophy under pharmacological induction of atrophy.
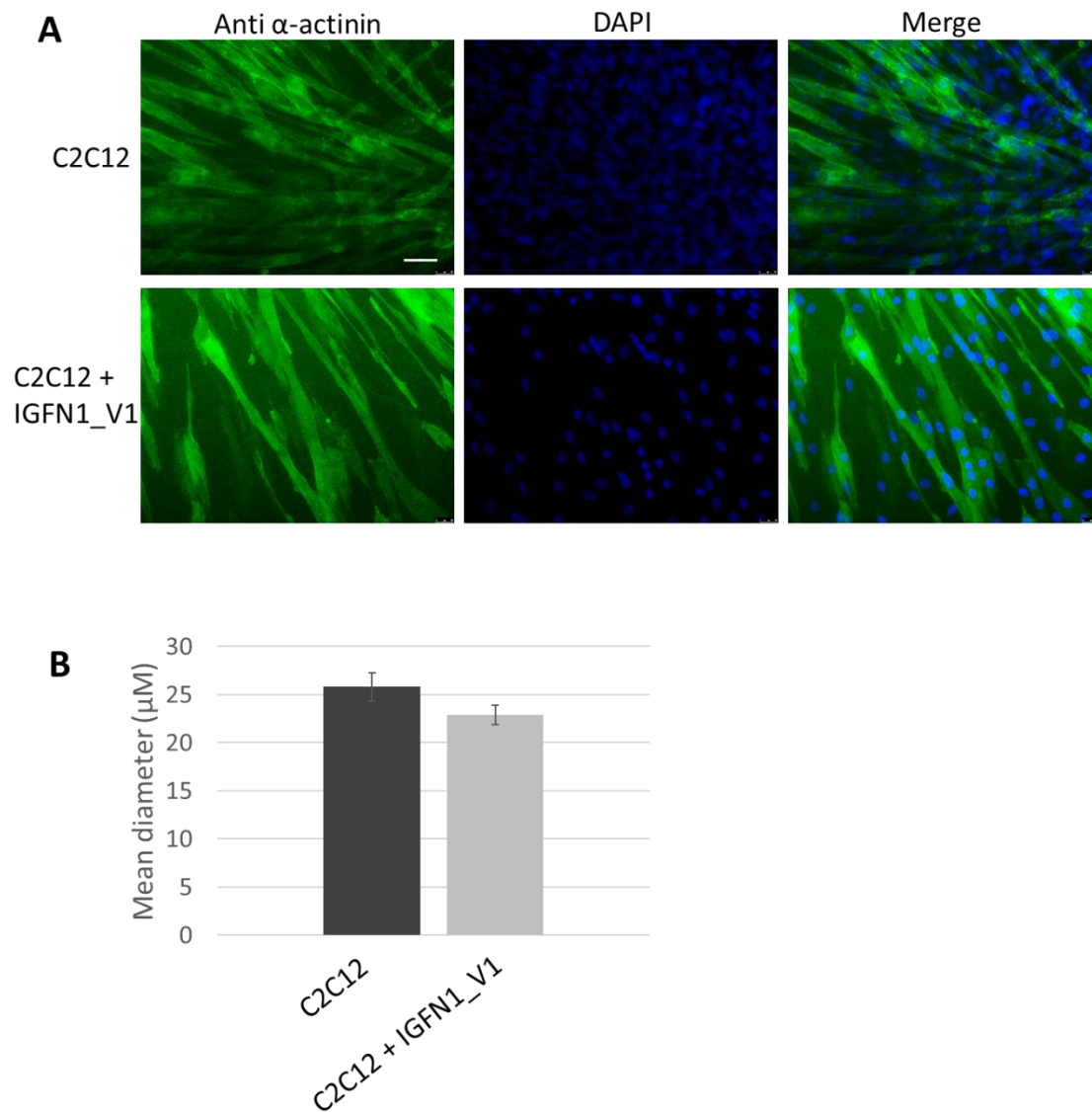
Figure 4.2. IGFN1_V1 overexpression does not lead to a change in myotube diameter. A) *Representative widefield images of wildtype (C2C12) and IGFN1_V1 overexpressing (C2C12+IGFN1_V1) myotubes after 7 days of differentiation. Cells stained with anti-alpha actinin antibody (green) and DAPI (blue). Scale bar represents 100 microns* **B)** *Quantification of mean myotube diameter of wildtype and IGFN1_V1 overexpressing myotubes. A minimum of 60 myotubes were measured per cell line. No significant difference in myotube diameter was detected (P=0.058).*

A

| | D0 | D3 Control | D3 + Dexamethasone |

C2C12

C2C12 +
IGFN1_V1

B

Mean Myotube Diameter at D3 as a Percentage of D0

- ■ No Dexamethasone
- ■ +100µM Dexamethasone
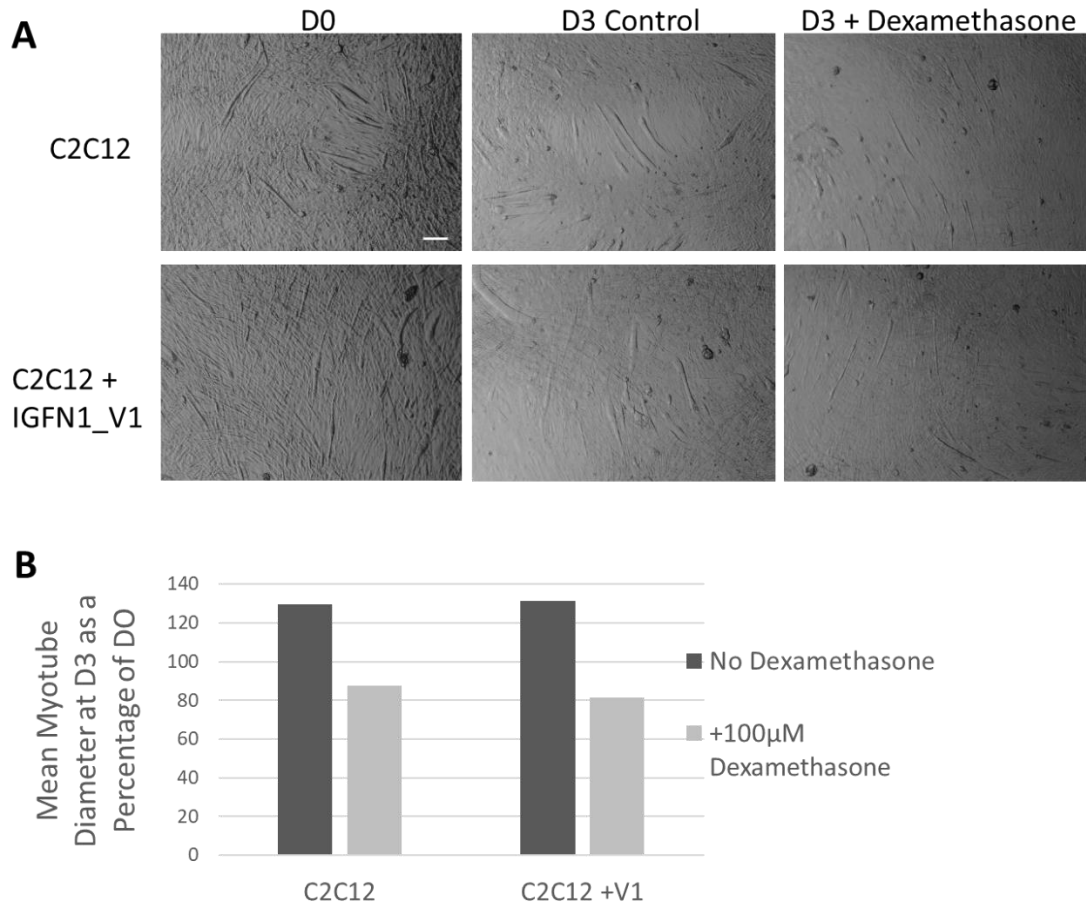
Figure 4.3. C2C12 myotubes and C2C12 myotube overexpressing IGFN1_V1 display a similar atrophic response to dexamethasone treatment. A) representative images of myotubes differentiated for 7 days before dexamethasone treatment (D0), following control treatment of differentiation media for 3 days (D3), and following dexamethasone treatment for 3 days (D3 + Dexamethasone). Scale bar represents 200 microns B) Average myotube diameter on D3 as a percentage of D0. Minimum of 40 myotubes measured per condition.

4.4 Dexamethasone Treatment Does Not Induce IGFN1 Expression

Because of the association of IGFN1 transcript expression with atrophy, and myostatin signalling in particular (Chen et al., 2014; Rahimov et al., 2011), it was expected that dexamethasone treatment would lead to an increase in IGFN1 protein expression levels. To test this, wildtype C2C12 cells were differentiated for 7 days followed by treatment with 100μM dexamethasone. Protein lysates were then taken at 0, 2, 8, and 24 hours post-treatment. SDS-PAGE western blots against IGFN1 were then performed (fig. 4.4).

The band pattern was complex, reflecting that observed in figure 3.1 chapter 3. No significant intensity increases in any band were observed throughout the time course. Overexposure of the blot did reveal one lower molecular weight band at 24 hours that was not observed in any other lane, which may reflect an increase in expression of at least one IGFN1 isoform. However, this result was inconsistent between replicates and is likely only an artefact caused by overexposure of the blot. Thus, this level of dexamethasone treatment does not increase the expression of IGFN1 at the protein level in differentiated myotubes.
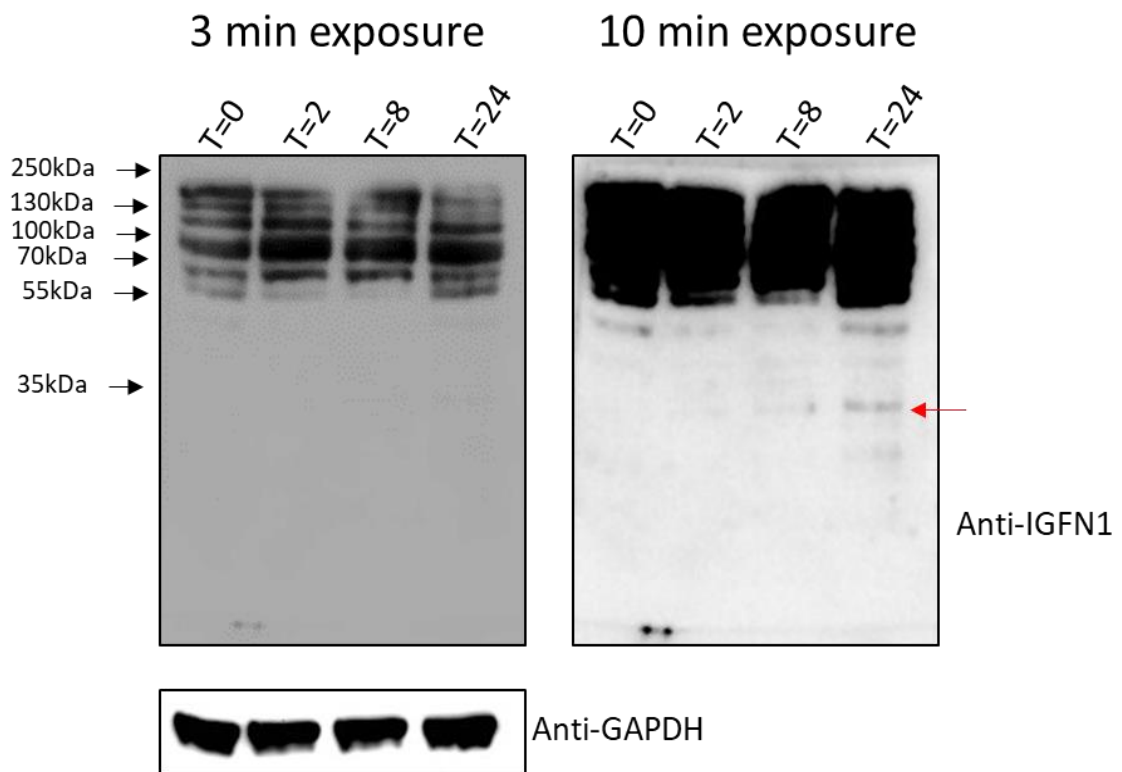
Figure 4.4. No change in IGFN1 expression is detected at the protein level in response to dexamethasone treatment. *Top, representative western blot against IGFN1 (Kip1b antibody) with samples of 7 day differentiated cells following 0, 2, 8, and 24 hours of treatment with 100µM dexamethasone. Two exposures (3 and 10 minutes) are shown. Red arrow indicates band at ~35kDa which may be upregulated. Bottom, anti-GAPDH western blot demonstrating equal loading of the samples.*

4.5 Conclusions

The observation that dexamethasone induces atrophy in wildtype C2C12 myotubes was expected, and in line with the previously published data. However, the concentration of dexamethasone required to induce atrophy was surprising. Concentrations as low as 100nM (Xu et al., 2013) have been shown to induce atrophy. Here however, 100µM of dexamethasone was required,

with lower concentrations merely stunting the atrophy observed in the control. This concentration is supraphysiological, assuming the concentration of dexamethasone in the blood and muscle tissue is equal (Faggioni et al., 2000), but has been used in previous studies (Raffaello et al., 2010). A potential explanation for these discrepancies is the presence of albumin within the serum added to growth media, which is known to bind to steroids (Baulieu, 1990). This makes it difficult to establish the actual amount of free dexamethasone present in the growth media and may lead to significant fluctuation between experiments.

There was no apparent effect of dexamethasone on IGFN1 knockout cells. While this may suggest that IGFN1 plays a role in dexamethasone-induced (and therefore myostatin-induced) atrophy, there are several confounding factors which may contribute to this result. Firstly, the morphological differences between the wildtype and IGFN1 knockout cells when differentiated, outlined in chapter 3, mean that it is much more difficult to define and measure a diameter in these cells compared to the wildtype. Furthermore, because of the fusion and differentiation defect in the IGFN1 knockout cells (chapter 3.4) (Li et al., 2017), it is likely that they are at a different stage of differentiation than the wildtype cells.

Dexamethasone has been demonstrated to have different effects on proliferating and differentiated C2C12 cells. Dexamethasone treatment of myoblasts has been shown to increase proliferation (Desler et al., 1996; Guerriero and Florini, 1980). As well as this, dexamethasone treatment at the single cell stage of myoblast differentiation results in larger myotubes (Han et al., 2017). Therefore, disruption of differentiation in IGFN1 knockout myoblasts may explain the absence of atrophy when treated with dexamethasone.

Due to the upregulation of IGFN1 under atrophic conditions it was expected that IGFN1 would influence myotube size if overexpressed. Myotubes derived from a cell line overexpressing IGFN1_V1 had a slightly smaller diameter than wildtype myotubes. However, this decrease was found to be not statistically significant. Atrophy was induced through dexamethasone treatment in both

cell lines to determine if overexpression of IGFN1_V1 would exacerbate the size decrease observed. Again, no significant difference was found between the change in size of the wildtype and IGFN1 overexpressing myotubes. Taken together, it can be concluded that IGFN1_V1 does not play a direct role in atrophy in myotubes.

From the previously published data it is not possible to determine which isoform of IGFN1 is upregulated in response to denervation or myostatin overexpression (Chen et al., 2014; Mansilla et al., 2008), or downregulated when myostatin signalling is inhibited (Rahimov et al., 2011). It is therefore possible that another IGFN1 isoform, not IGFN1_V1 as tested here, is directly involved in inducing atrophy.

Western blots against IGFN1 were used to determine which, if any, of the isoforms of IGFN1 were upregulated. Only one of the isoforms detected by the antibody used were upregulated in response to dexamethasone, with a band observed at around 35kDa. However, this was not consistent in all replicates and required overexposure of the blot, casting doubt on its reliability. This result suggests that dexamethasone treatment is not sufficient to induce IGFN1 expression. This may be because dexamethasone acts to induce atrophy indirectly and may contribute to other cellular processes, unlike the direct inhibition or upregulation of myostatin signalling used in the literature previously. It should also be noted that the previous data was produced in vivo, compared to the cellular model used here.

Taken together these data show that IGFN1_V1 is not directly involved in atrophy induced by dexamethasone treatment, and that IGFN1 is not overexpressed at a protein level in this model of atrophy. These data support recently published data in vivo demonstrating that overexpression of IGFN1 through electroporation does not change muscle fibre cross-sectional area. Nor does mutagenesis of IGFN1, through electroporation of a CRISPR/Cas9 construct targeting IGFN1, lead to a change in fibre size, although the effectiveness of this mutagenesis was not confirmed (Li et al., 2017). Indeed, it is possible that IGFN1 expression is increased during atrophy in order to

protect the integrity of critical sarcomeric components, especially those at the z-disc.

More work is required to determine the purpose of IGFN1 upregulation in atrophy. This work should focus on the use of in vivo models and the direct inhibition or upregulation of the myostatin signalling pathway, rather than the use of dexamethasone in cellular models, which has proved an unreliable model here.

CHAPTER 5: EXPRESSION AND PURIFICATION OF SOLUBLE IGFN1 FRAGMENTS

Chapter 5: Expression and Purification of Soluble IGFN1 Fragments

5.1 Introduction

This chapter concerns the development of a protocol for the production and purification of IGFN1 fragments for use in biochemical and biophysical analysis.

Recombinant IGFN1 is required for pull-down experiments to identify interacting partners (outlined in Chapter 6). Further, with recombinant IGFN1 the physical properties of the protein's domains could be better understood, shedding light on their roles. Skeletal muscle proteins with similar domain compositions to IGFN1 have been shown, through atomic force microscopy (AFM), to act as molecular springs with domains unfolding and refolding to respond to the tension placed on the sarcomere throughout contraction and relaxation (Rief et al., 1997; Schoenauer et al., 2005). It is possible that IGFN1 performs a similar role. The production of recombinant protein is required to allow for these AFM experiments to take place.

Previous attempts to produce IGFN1 in *E. coli* have been unsuccessful (J Baker, personal comm). These attempts have focused on the large isoforms of IGFN1 including the full-length IGFN1 protein and IGFN_V1. These proteins were largely insoluble, likely due to their size, and could not be expressed and purified in sufficient quantities, with precipitates forming following elution from Ni-NTA agarose beads. In this chapter smaller IGFN1 fragments are used to ascertain whether these would produce higher yields. Additionally, a number of different expression protocols are trialled to optimise IGFN1 expression and solubility. Finally, an IGFN1 fragment is cloned into the pQE2-Im9 vector, resulting in the production of a soluble, folded protein.

5.2 Full-length IGFN1 Isoforms are Largely Insoluble When Expressed in *E. coli*

Previous attempts from our group to purify full-length IGFN1 proved unsuccessful, largely due to insolubility. There had however been some progress in producing and purifying IGFN1_V1 (see table 5.1 for domain composition), albeit at very low concentrations with high insolubility. These previous attempts had used an overnight expression at 37°C. Expression of insoluble proteins at lower temperatures can increase their solubility, through slowing of transcription and translation rates, and decreasing the strength of hydrophobic interactions (Baneyx and Mujacic, 2004). Therefore, a 20°C overnight incubation was trialled.

Table 5.1. Summary of purified recombinant IGFN1 peptides. *Schematics show domain type and linker regions. Domain compositions are not to scale.*

Construct	Domain Composition	Mw (kDa)
IGFN1_V1	His$_6$ — IG-like — IG-like — IG — IG — IG — FN3 — FN3 — FN3 — IG — FN3 — IG-c2	~135
IGFN1_d1-d3	His$_6$ — IG-like — IG-like — IG	~37
IGFN1_d8-d11	His$_6$ — FN3 — FN3 — FN3 — IG — FN3 — IG-c2	~70
Im9-IGFN1_d1-d3	His$_6$ — Im9 — IG-like — IG-like — IG	~40

Glycerol cultures of BL21-AI™ *E. coli* containing the pET161-DEST-IGFN1_V1 vector were plated on LB agar (+ampicillin) and a single colony inoculated into LB (+ampicillin) and grown to OD_{600}=0.6 (t=0). At this point both IPTG (1mM) and L-arabinose (0.02%) were added to the media. Addition of L-arabinose induces expression of T7 RNA polymerase from the BL21-AI™ genome under the control of the araBAD promoter. Addition of IPTG allows the expression of the His-tagged IGFN1_V1 from the pET plasmid. The cultures were then moved to 20°C and samples were taken at multiple timepoints (values for t given in hours). This was followed by purification using the ProBond Purification System (see Materials and Methods 2.13.2 for details).

Figure 5.1A demonstrates robust expression of IGFN1_V1, which increases at each timepoint. However, upon separation of the soluble and insoluble fractions it was revealed as previously that most, if not all, of the IGFN_V1 expressed was insoluble (fig 5.1B). Therefore, it was decided to attempt to purify smaller IGFN1 fragments which may prove more soluble in *E. coli* and lead to higher yields. These included domains 1-3 of IGFN1 (IGFN1_d1-d3) and domains 6-11 (IGFN1_d6-d11) which had been previously cloned into pET161-DEST.
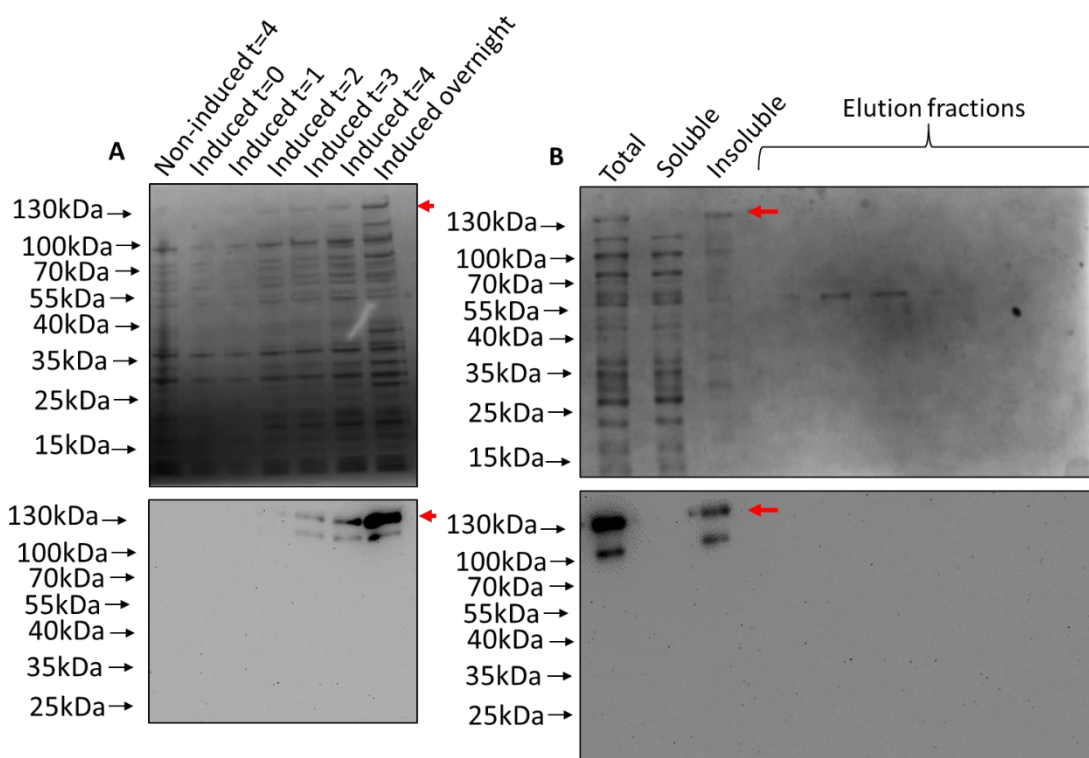
Figure 5.1. IGFN1_V1 is insoluble when expressed in BL21-AI™ E. coli via the pET161-DEST vector. A) *Top Coomassie and bottom anti-His western blot of E. coli lysates throughout induction of pET161-DEST-IGFN1_V1 expression in BL21-AI™ E. coli. At t=0 OD_{600}=0.6, IPTG was added to media to a final concentration of 1mM, and L-arabinose to 0.2%. Samples were then taken at 1,2,3, and 4 hours (t=1/2/3/4) and following overnight incubation at 20°C. A non-induced control was also used demonstrating that IGFN1_V1 was not being expressed in the absence of induction by IPTG and L-arabinose. All lanes were loaded with the same concentration of cell lysate by normalising using OD_{600} readings. Red arrows indicate bands corresponding to the molecular weight of IGFN1_V1 (~135kDa) which increase in intensity throughout the experiment.* ***B)*** *Top Coomassie and bottom anti-His western blot of total, soluble, and insoluble fractions of E. coli expressing pET161-DEST-IGFN1_V1 overnight, as well as elution fractions following purification via the ProBond Purification System. Red arrows indicate bands corresponding to the molecular weight of IGFN1_V1 (~135kDa). IGFN1_V1 was not detectable in the soluble fraction.*

5.3 Soluble IGFN1 Fragments can be Expressed and Purified in *E. coli* but form a Precipitate in the Absence of Imidazole

To alleviate the insolubility observed in the larger recombinant IGFN1 isoforms, two smaller constructs were transformed into BL21-AI™ *E. coli.* These were pET161-DEST-IGFN1_d1-d3 and pET161-DEST-IGFN1_d6-d11 coding for His-tagged IGFN1 fragments, containing domains 1-3 of IGFN1 (IGFN1_d1-d3) and domains 6-11 (IGFN1_d6-d11), respectively (table 5.1). As well as this, and lower incubation temperatures, sequential induction was trialled. This involved the addition of L-arabinose when the culture had reached OD_{600}=0.6 (t=0), to release expression of T7 RNA polymerase from the BL21-AI™ genome. This was followed by the addition of IPTG after 2 hours (t=2) to induce the expression of the His-tagged IGFN_d1-d3 from the pET plasmid. In theory, this would reduce the metabolic load on cells, therefore increasing the solubility and the yield of the over expressed recombinant protein fragment. The different protocols tested are summarised in table 5.2.

The most successful protocol for obtaining soluble IGFN1_d1-d3 described in table 5.2 included sequential induction, 30°C overnight incubation, and a change of media between addition of L-arabinose and IPTG. This is described in figure 5.2A. Robust expression of IGFN1_d1-d3 was seen at t=3 after the addition of IPTG, demonstrating the sequential induction was successful in producing high levels of IGFN1_d1-d3, with a large amount of protein in the soluble fraction (fig. 5.2B).

Purification of the His-tagged protein was performed using the ProBond Purification System, this resulted in relatively high yields of IGFN1_d1-d3 (fig. 5.2C). The band observed at ~37kDa was analysed through LC-MS, confirming its identity as IGFN1. However, upon dialysis to remove imidazole from the buffer, a precipitate formed (fig. 5.2D). The removal of imidazole is required to allow the His-tagged protein to bind to Ni-NTA-coated coverslips for use in AFM experiments. The protein could, however, be left bound to beads for use in pull-down experiments (as in chapter 6).

Table 5.2. Summary of conditions trialled to optimise expression of protein in the soluble fraction. *Simultaneous addition of L-arabinose and IPTG refers to L-arabinose and IPTG being added at the same time point, while sequential describes addition at different time points as described in* figure *5.2.A. Media changed refers to whether the cells were pelleted, and the media changed between the addition of L-arabinose and the addition of IPTG. Overnight culture temperature refers to the temperature at which the culture was left overnight to express protein following the addition of both L-arabinose and IPTG. Success was determined by examining the amount of protein expressed in the soluble fraction compared to the insoluble fraction (Y=yes N=no P=partial).*

Construct	Addition of L-arabinose and IPTG	Media changed	Overnight culture temperature (˚C)	Successful
IGFN1_V1	simultaneous	N/a	37	N
IGFN1_V1	simultaneous	N/a	20	N
IGFN1_d1-d3	simultaneous	N/a	37	N
IGFN1_d1-d3	simultaneous	N/a	30	P
IGFN1_d1-d3	simultaneous	N/a	20	P
IGFN1_d1-d3	sequential	N	30	Y
IGFN1_d1-d3	sequential	Y	30	Y
IGFN1_d6-d11	sequential	Y	30	P

A similar pattern was observed when attempting to produce IGFN1_d6-d11 using the same protocol, with expression observed at t=4, slightly later than for IGFN1_d1-d3 (fig. 5.3A). Soluble protein could then be purified, albeit at lower yields than IGFN1_d1-d3 (fig. 5.3B). However, the same issue occurred following dialysis, with a precipitate forming upon the removal of imidazole (fig. 5.3C). Again, leaving the purified protein bound to the Ni-NTA beads would allow for pull-down experiments. However, it would not be possible to use the recombinant protein in any biophysical analysis.
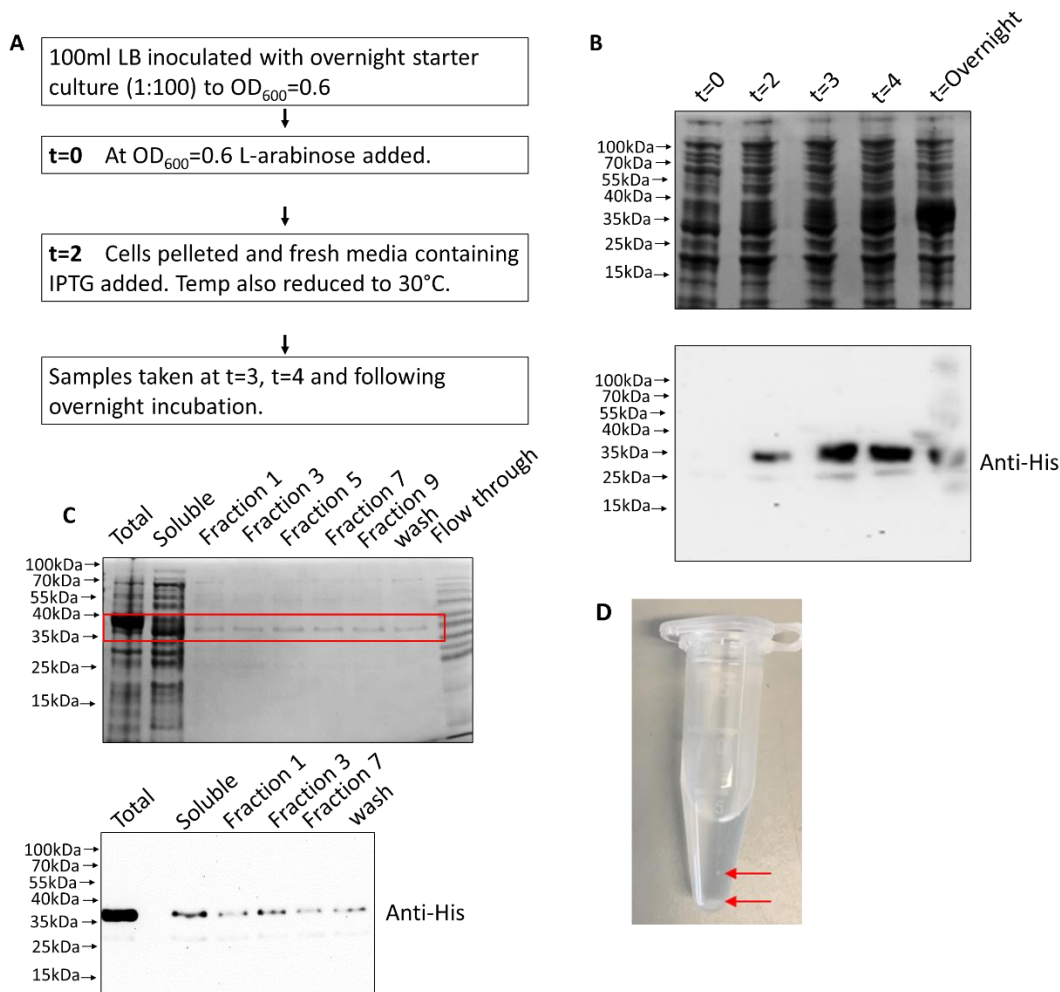
Figure 5.2. Production and Purification of IGFN1_d1-d3. A) *Schematic representation of induction protocol used. Values for t given in hours.* ***B)*** *Top Coomassie and bottom western blot against His-tagged IGFN1_d1-d3 of lysates from time points during the induction protocol, time points correspond to time points in A. All lanes were loaded with the same concentration of cell lysate by normalising using OD$_{600}$ readings. Bands at 37kDa correspond to IGFN1_d1-d3.* ***C)*** *Top Coomassie and bottom western blot against His-tagged IGFN1_d1-d3 following purification using the ProBond Purification System. Total and soluble fractions of E. coli expressing pET161-DEST-IGFN1_d1-d3 overnight are included, as well as elution fractions following purification via the ProBond Purification System. Wash and flow through samples are also shown representing a sample of wash buffer following the first wash, and a sample of E. coli lysate following bead incubation, respectively. Red box highlights bands identified as IGFN1 through LC-MS. Gels were loaded separately with the same samples.* ***D)*** *Image of IGFN1_d1-d3 following purification and dialysis to remove imidazole, red arrows indicate clearly visible precipitate.*
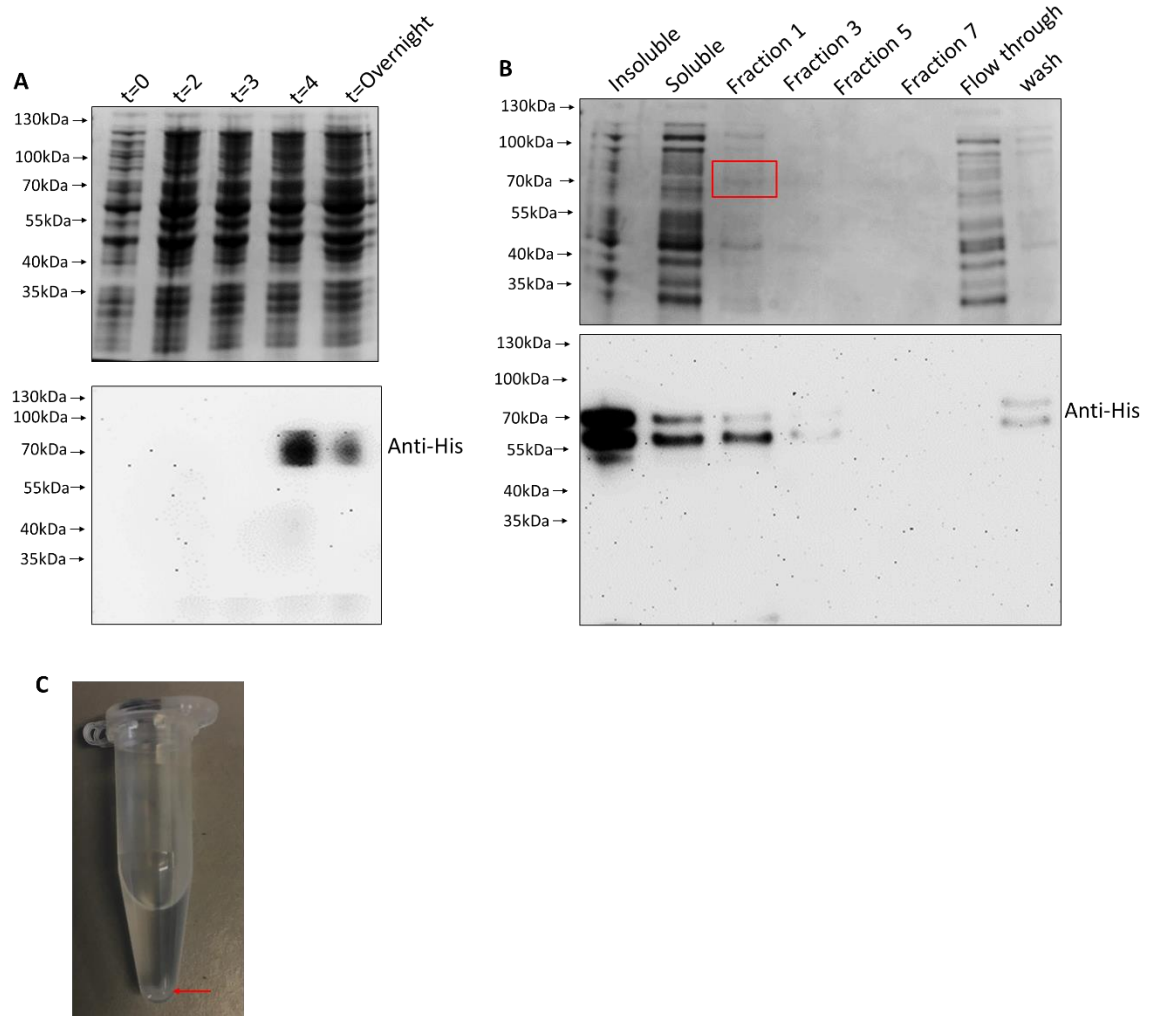
Figure 5.3. Production and Purification of IGFN1_d6-d11. *Expression was induced as for IGFN1_d1-d3 in figure 5.2 **A)** Top Coomassie and bottom western blot against His-tagged IGFN1_d6-d11 of lysates from time points during the induction protocol, time points correspond to time points in fig.5.2A. All lanes were loaded with the same concentration of cell lysate by normalising using OD$_{600}$ readings. **B)** Top Coomassie and bottom western blot against His-tagged IGFN1_d6-d11 following purification using the ProBond Purification System. Red box highlights band identified as IGFN1 through LC-MS. **C)** Image of IGFN1_d6-d11 following purification and dialysis to remove imidazole, red arrows indicate clearly visible precipitate.*

5.4 Cloning of IGFN1_d1-d3 into the pQE2-Im9 Expression Vector Allows Purification of a Soluble, Folded IGFN1_d1-d3 Fragment

Due to the formation of a precipitate upon removal of imidazole from the storage buffer, IGFN1_d1-d3 was cloned into a vector containing the Im9 solubility tag pQE2-Im9 (Jared Cartwright, Bioscience Technology Facility, University of York). This expression vector results in a fusion of a His-tagged variant of the bacterial colicin E9 immunity protein (His7-Im9) to the N-terminus of the recombinant protein-of-interest. The Im9 domain has been used to enhance the solubility of recombinant proteins. The mechanism that underlies this is not fully understood, but may be due to its rapid folding upon exiting the ribosome, thus facilitating the folding of the larger polypeptide to which it is fused (for a review of solubility tags see (Malhotra, 2009)).

IGFN1_d1-d3 was amplified using primers designed for use with the NEBuilder assembly cloning kit (Materials and Methods 2.12.4) (fig. 5.4A and B), and the NEBuilder assembly reaction was performed to ligate the two IGFN1 fragments into the vector (fig. 5.4.D). Colony PCR was then performed on BL21-AI™ E. *coli* colonies transformed with the pQE2-Im9-IGFN1_d1-d3 vector, to confirm the presence of the construct (fig. 5.5). Bands were observed in all colonies of the pQE2-Im9-IGFN1_d1-d3 transformed colonies at the expected size.
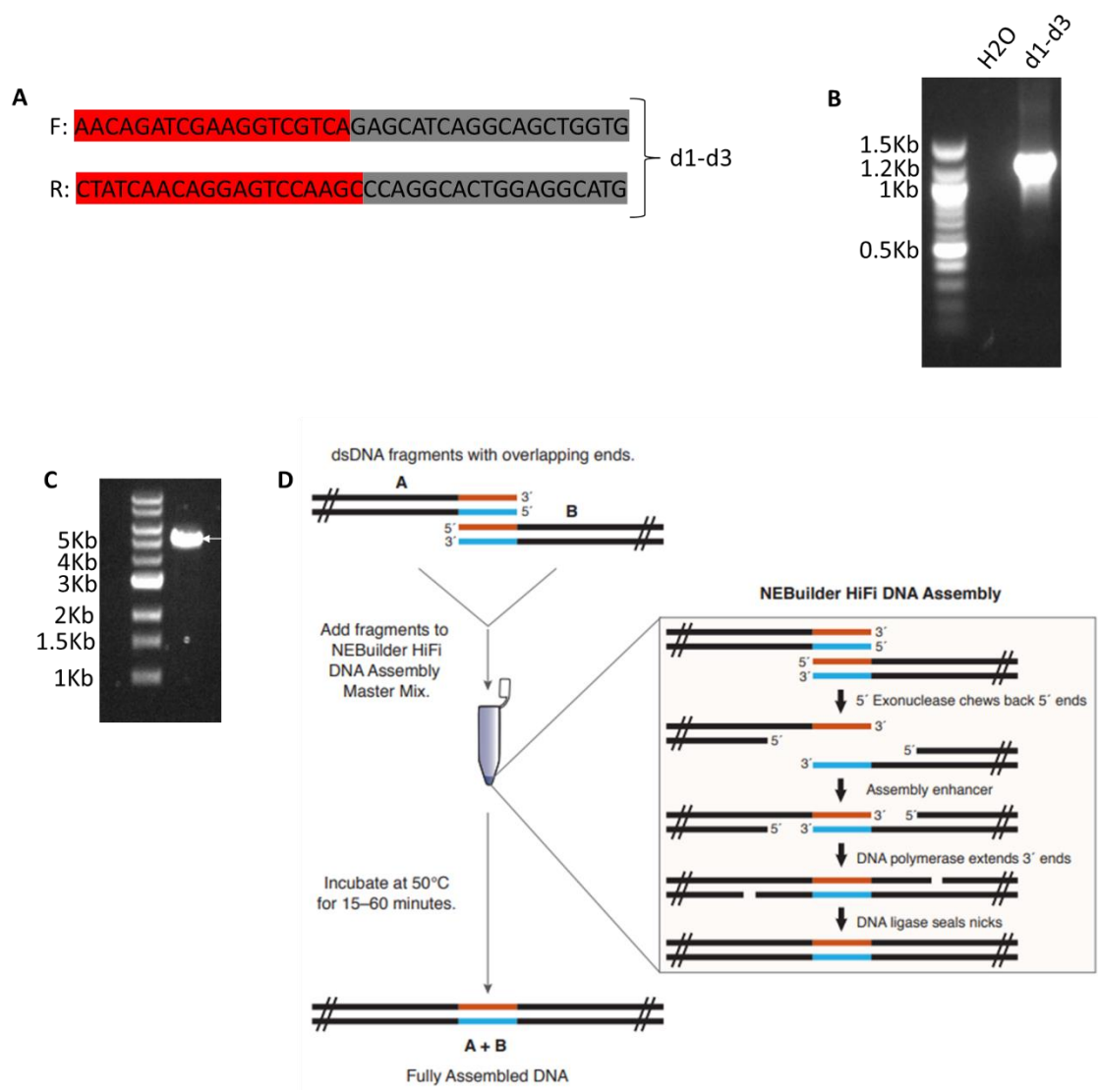
Figure 5.4. Cloning of IGFN1_d1-d3 into pQE2-Im9 using NEBuilder High-fidelity assembly cloning. A) Primer design, text in grey represents gene-specific primer sequence, text in red represents sequence overlapping the digested Im9 vector. **B)** Amplification of IGFN1_d1-d3 from pDEST47-IGFN1_V1-TdTomato vector using primers in A, with water control, band present for IGFN1_d1-d3 at ~1.2Kb. **C)** Digestion of pQE2-Im9 using NdeI and BlpI to produce a linear construct of 4962bp (arrow) to be used for NEBuilder HiFi assembly reaction, and a fragment of 66bp (run off gel). **D)** Schematic of NEBuilder HiFi cloning reaction (taken from NEBuilder manual).
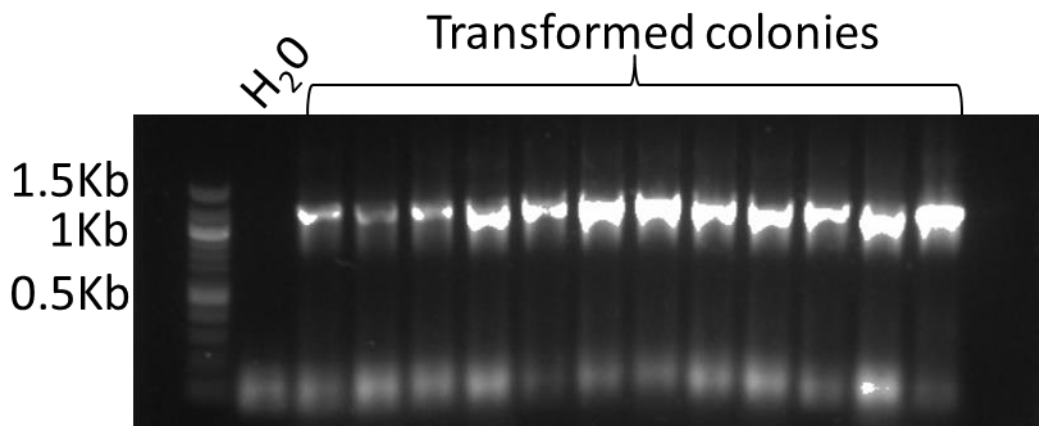
Figure 5.5. Colony PCR of colonies of pQE2-Im9-IGFN1_d1-d3 transformed BL21-AI™ E. coli. *Primers described in figure 5.4A were used and identified pQE2-Im9-IGFN1_d1-d3 at ~1.2Kb in all colonies tested.*

The same expression protocol as in figure 5.2A was used with the BL21-AI™ *E. coli* harbouring pQE2-Im9-IGFN1_d1-d3. Robust expression was observed (fig. 5.6A), and soluble protein was purified (fig. 5.6B). Two main bands were observed in purified fractions, one was identified as Im9-IGFN1_d1-d3 through LC-MS, the other as Elongation Factor Tu (EF-Tu). Crucially, no precipitate formed following dialysis to remove imidazole from the storage buffer (fig. 5.6C).
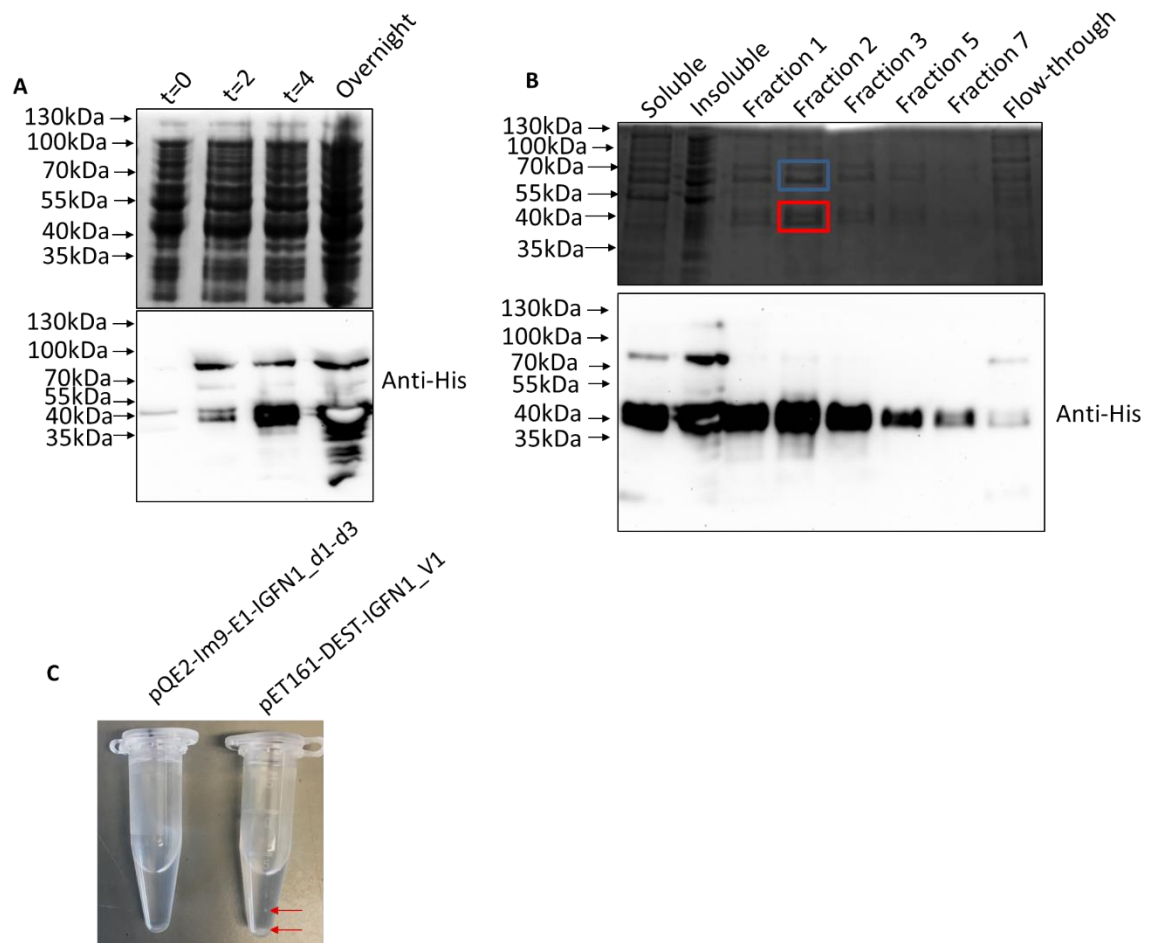
Figure 5.6. Production and Purification of IGFN1_d1-d3. A) *Top Coomassie and bottom western blot against His-tagged Im9-IGFN1_d1-d3 of lysates from time points during the induction protocol (as in figure 5.2A). At t=0 both L-arabinose and IPTG were added. All lanes were loaded with the same concentration of cell lysate by normalising using OD$_{600}$ readings.* **B)** *Top Coomassie and bottom western blot against His-tagged Im9-IGFN1_d1-d3 following purification using the ProBond Purification System. Red box highlights band identified as IGFN1 through LC-MS, contaminant highlighted in blue box was identified as Elongation Factor Tu.* **C)** *Comparison of Im9-IGFN1_d1-d3 and original recombinant IGFN1_d1-d3 from figure 5.2 following dialysis to remove imidazole. No precipitate is observed in the Im9-IGFN1_d1-d3 sample.*

Finally, thermal unfolding of the recombinant Im9-IGFN1_d1-d3 was performed to determine whether it contained folded domains. Differential scanning fluorimetry was performed using the Prometheus NT.48 Nano DSF with PR.ThermControl v2.1.2 software (NanoTemper). The fluorescence emission wavelength of intrinsic tryptophan residues buried in a folded protein structure will shift upon thermal unfolding. This unfolding transition is monitored by detecting the fluorescence emission at wavelengths of 330 nm and 350 nm as the temperature is increased. The two separate wavelengths monitor the change in emission from intrinsic tryptophan residues as they move from a non-polar (buried) to a polar (not buried) environment during protein unfolding. This is used to determine the protein melting point Tm, where half of the protein is folded, and the other half is unfolded. The first derivative of the F350/F330 fluorescence intensity ratio is used to calculate this parameter.

Distinct peaks were observed in the first derivatives of the 350nm/330nm ratio, which revealed two distinct unfolding events at ~58°C and ~73°C (fig.5.7). These may represent the sequential unfolding of two domains at different temperatures. It may also be that one of the peaks is from the contaminant Elongation Factor Tu. These possibilities will be discussed below.

Mechanical unfolding using atomic force microscopy was attempted with the above samples, as described in Materials and Methods 2.16. Unfortunately, this work proved unsuccessful. The peaks generated did not fit a worm-like chain model (For a review see (Fisher et al., 1999; Ott et al., 2017)). This meant that the unfolding and refolding dynamics of the IGFN1 domains could not be measured during the timeframe of this project.
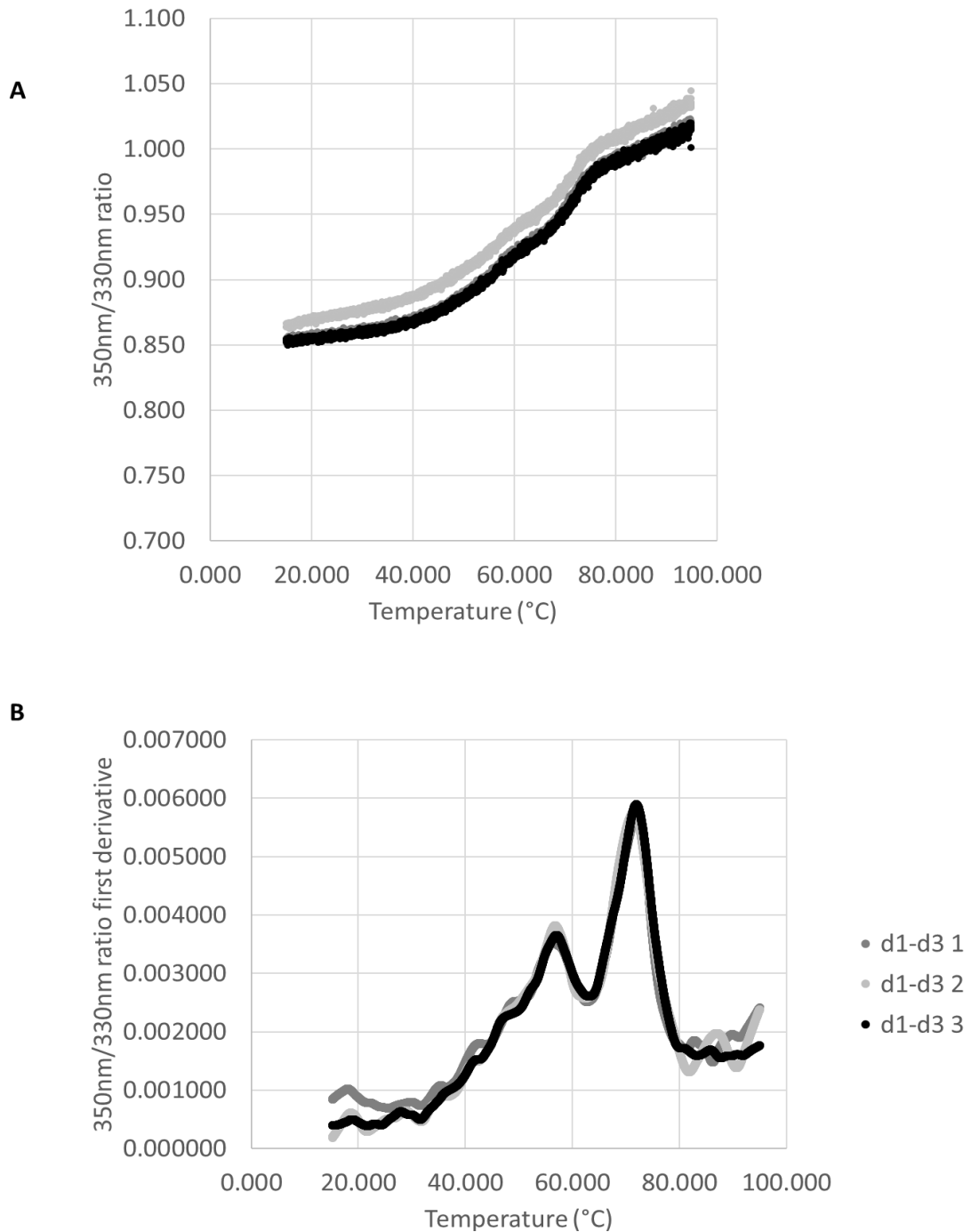
Figure 5.7. Thermal Unfolding of Im9-IGFN1_d1-d3. *Thermal unfolding (differential scanning fluorimetry) was performed using the Prometheus NT.48 Nano DSF with PR.ThermControl v2.1.2 software (NanoTemper). Three technical replicas are shown. Unfolding was performed from 15-95°C with a 1.3°C/min gradient, 200μg/ml of protein in PBS was used. **A)** 350nm/330nm ratio against temperature **B)** First derivatives of 350nm/330nm ratio. Peaks at ~58°C and ~73°C reveal two distinct unfolding events.*

5.5 Conclusions

As was previously reported, the production and purification of any IGFN1 peptide proved a difficult undertaking. Most of the difficulty stemmed from the insolubility of the recombinant protein. This was particularly apparent for the larger IGFN1 isoforms, and some of the issues were overcome by using the smaller IGFN1 fragments IGFN1_d1-d3 and IGFN1_d6-d11. However, upon removal of imidazole, a precipitate was present. Cloning of IGFN1_d1-d3 into the pQE2-Im9 vector allowed for production and purification of recombinant protein, free from precipitate in the absence of imidazole.

This protein was not entirely pure, with the elongation factor EF-Tu detected as co-purifying with IGFN1. The eukaryotic homologue of EF-Tu is the alpha subunit of eEF1A, which itself has been previously shown to interact with IGFN1 (Mansilla et al., 2008). It is therefore likely that the co-purification of IGFN1 and EF-Tu is the result of a specific interaction between the two. This lends weight to the idea that IGFN1 may play a role in elongation during translation, possibly as a scaffold or inhibitor, and may be related to the association of IGFN1 expression with atrophic signalling.

The resulting recombinant protein was then thermally unfolded. This would provide some insight into whether the protein was properly folded, thus allowing for mechanical folding experiments using AFM. Two distinct unfolding events at ~58°C and ~73°C were detected. As mentioned above, a contaminant protein was present which was identified as EF-Tu. However, it is unlikely that either unfolding event was that of EF-Tu. The T_m of *E. coli* EF-Tu is 42.4°C or 46.5°C depending on whether the protein is GTP or GDP bound (Sanderova et al., 2004), much lower than either peak detected here.

The T_m of titin modules made up of Ig-like domains mostly range from 54.0°C to 72.6°C, with only one example outside of this range having a T_m of 35.3°C (Politou et al., 1995). Assuming that the Ig-like domains of titin and IGFN1 are structurally similar, it is likely that the unfolding events seen at ~58°C and ~73°C for Im9-IGFN1_d1-d3 represent the unfolding of its Ig or Ig-like

domains. On that basis, we consider the recombinant protein of sufficient purity and integrity for mechanical unfolding experiments.

The objective at the outset of this project was to be able to perform mechanical unfolding experiments to ascertain whether IGFN1 plays a biophysical role at the z-disc, possibly acting as a mechanical spring to absorb the contractile forces placed on the sarcomere. Proteins with similar domain compositions have been demonstrated to perform this role, therefore it is possible that IGFN1 also performs this role (Rief et al., 1997; Schoenauer et al., 2005). Initial attempts to unfold the purified domains using AFM were undertaken and distinct peaks in the force versus extension data were observed (data not shown). Worm-like chain analysis of these force peaks (analysis completed by William Rochira and Christoph Baumann) suggested they were due to adsorption of the AFM tip to the functionalised glass surface, rather than unfolding of a single protein domain. Issues including a delay in the full installation of the atomic force microscope, and scheduling issues with the relevant people, meant that, despite protein being ready for use, the mechanical unfolding experiments could not be repeated and refined for inclusion in this thesis.

Now that a protocol has been established for the purification of one IGFN1 fragment, future work should include fresh attempts at the AFM experiments to investigate the mechanical unfolding properties of the purified IGFN1 fragment. Alongside this, other IGFN1 fragments should be cloned into the pQE2-Im9 vector, to establish a full picture of the unfolding, and refolding, dynamics of all the predicted IGFN1 domains.

CHAPTER 6: VALIDATION OF A PROTEIN-PROTEIN INTERACTION BETWEEN IGFN1 AND COBL

Chapter 6: Validation of a Protein-Protein Interaction Between IGFN1 and COBL

6.1 Introduction

This chapter outlines the identification and validation of an interaction partner of IGFN1 in skeletal muscle.

The domain composition of IGFN1, consisting of a series of evenly spaced globular domains at the N and C-terminal ends of the protein, suggests that IGFN1 acts as a scaffolding protein. These immunoglobulin and fibronectin-like domains are typically present in other sarcomeric proteins (e.g. titin and myomesisn) and have been implicated in protein-protein interactions. It is therefore hypothesised that IGFN1 may act by bringing together protein complexes and that its main biological function may be revealed by exposing these interaction partners, since IGFN1 itself lacks any enzymatic activity. In order to identify potential interaction partners of IGFN1, proteomic analysis of pull-downs of mouse muscle against IGFN1 fragments was performed. Because of the fusion defect and the altered actin remodelling phenotypes observed in IGFN1 knockout myoblasts outlined in previous chapters, any proteins involved with myoblast fusion or in actin remodelling were of particular interest, and these interactions were to be validated further. Validation was performed using co-immunoprecipitation, as well as co-localisation both in-vitro and in-vivo.

6.2 Proteomic Identification of Potential IGFN1 Interaction Partners

To identify interaction partners of IGFN1 pull-downs were performed using mouse muscle extracts against either LacZ (as a negative control), IGFN1 domains 1-3 (IGFN1_d1-d3), or IGFN1 domains 6-11 (IGFN1_d6-d11) immobilised on Ni-NTA agarose beads (fig. 6.1). The eluate was sent for LC-MS/MS analysis, which was performed by Adam Dowle at the University of York Biology Technology Facility (see Materials and Methods 2.17 for details).
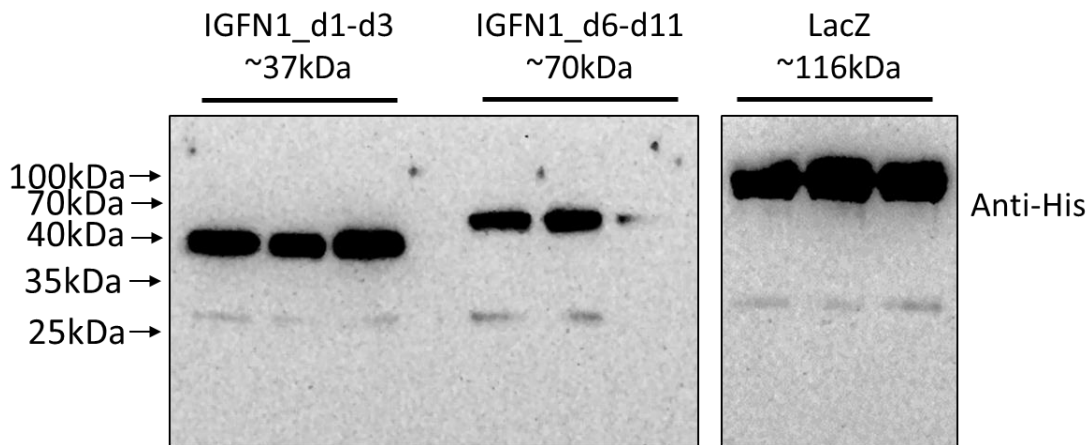
Figure 6.1. Confirmation of purified protein immobilisation to Ni-NTA agarose beads. *Anti-His western blots of Ni-NTA agarose beads following immobilisation of protein show bands at the expected sizes for all three His-tagged proteins (LacZ-His, IGFN1d1-d3-His, and IGFN1d6-d11-His) in all three replicas of each protein. All gels were run alongside one another with blot development performed in tandem. It should be noted that the concentration of immobilised protein was relatively low for d6-d11 replica 3, however protein was clearly present. LacZ concentration was higher in all samples than either IGFN1 fragment.*

Several potential interaction partners were identified. The following criteria were applied to determine presence or absence in each pull-down: 1) Inclusion required protein identification probability of greater than 95% in at least two of three biological replicas; 2) Exclusion required protein identification probability of less than 95% in all three biological replicas. The filtered data set indicating proteins identified with fragment IGFN1(d1-d3), IGFN1(d6-d11) or both, and not with LacZ, is presented in Table 1. Functional enrichment as determined by STRING-db (Szklarczyk et al., 2015) highlighted the cytoskeleton and the proteasome as the main components. STRING-db identified significantly more interactions between the proteins identified than would be expected of a random set of proteins, suggesting the potential interactions are functionally relevant (fig. 6.2). The cytoskeletal crosslinker alpha-actinin, located at the Z-disc, and the actin nucleation protein cordon-bleu (COBL) were found in

eluates from both IGFN1 fragments. A number of proteasome subunits were also detected.

Table 6.1. IGFN1 interaction partners. *Filtered data set including proteins identified as potential interaction partners of fragment IGFN1(d1-d3), IGFN1(d6-d11), or both, and not with the LacZ control. Protein ID required a minimum of 2 peptides (<1FDR), for a protein to be included in a set a >95% ID probability in >1 sample was required and for the protein to be classed as not identified in the LacZ control. p values from ANOVA testing represent the probability of obtaining the given LC-MS/MS results for each protein across all experiments to minimise false positives from multiple tests. Therefore, for proteins identified as an interacting partner of more than one fragment the p value is the same.*

d1-d3			d6-d11			d1-d3 and d6-d11		
Accession Number	Alternate ID	p value	Accession Number	Alternate ID	p value	Accession Number	Alternate ID	p value
IGFN1_MOUSE	Igfn1	0.0001	IGFN1_MOUSE	Igfn1	0.0001	IGFN1_MOUSE	Igfn1	0.0001
NFS1_MOUSE	Nfs1	0.0018	LAMC1_MOUSE	Lamc1	0.0028	COBL_MOUSE	Cobl	0.0043
COBL_MOUSE	Cobl	0.0043	COBL_MOUSE	Cobl	0.0043	EMC7_MOUSE	Emc7	0.15
HDHD5_MOUSE	Hdhd5	0.0066	CO1A2_MOUSE	Col1a2	0.056	CAVN4_MOUSE	Cavin4	0.2
ACSL1_MOUSE	Acsl1	0.018	EMC7_MOUSE	Emc7	0.15	JSPR1_MOUSE	Jsrp1	0.2
MIC26_MOUSE	Apoo	0.031	ILK_MOUSE	Ilk	0.17	PSD12_MOUSE	Psmd12	0.56
SYQ_MOUSE	Qars	0.061	H2B1B_MOUSE	Hist1h2bb	0.17			
AT2L2_MOUSE	Phykpl	0.079	CAVN4_MOUSE	Cavin4	0.2			
DJB11_MOUSE	Dnajb11	0.086	JSPR1_MOUSE	Jsrp1	0.2			
PDK2_MOUSE	Pdk2	0.12	CAN2_MOUSE	Capn2	0.25			
UN45B_MOUSE	Unc45b	0.13	EF1D_MOUSE	Eef1d	0.25			
BCKD_MOUSE	Bckdk	0.13	MAGT1_MOUSE	Magt1	0.25			
EMC7_MOUSE	Emc7	0.15	PCBP1_MOUSE	Pcbp1	0.27			
CALM1_MOUSE	Calm1	0.17	ACTN1_MOUSE	Actn1	0.32			
RIPL1_MOUSE	Rilpl1	0.18	PLAK_MOUSE	Jup	0.37			
CAVN4_MOUSE	Cavin4	0.2	TPP2_MOUSE	Tpp2	0.37			
JSPR1_MOUSE	Jsrp1	0.2	PSD12_MOUSE	Psmd12	0.56			
MP2K6_MOUSE	Map2k6	0.25	KLC1_MOUSE	Klc1	0.58			
ERGI1_MOUSE	Ergic1	0.25						
STRAP_MOUSE	Strap	0.27						
PSMD2_MOUSE	Psmd2	0.4						
SYK_MOUSE	Kars	0.42						
RL24_MOUSE	Rpl24	0.53						
PSD12_MOUSE	Psmd12	0.56						
PSD11_MOUSE	Psmd11	0.59						
TM109_MOUSE	Tmem109	1						
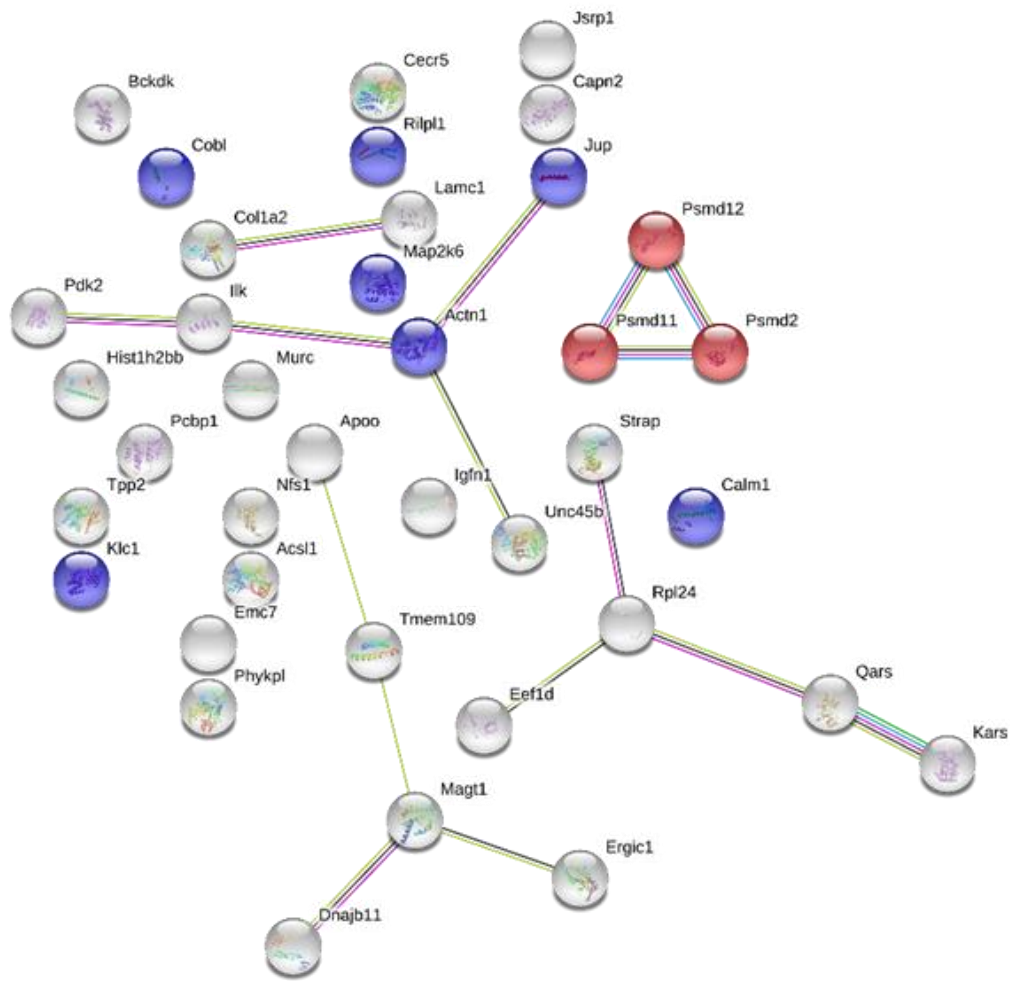
Figure 6.2. STRING-Db summary of IGFN1 interaction partners. *STRING-Db output of proteins found to interact with either IGFN1_d1-d3 or IGFN1_d6-d11, or both, and not LacZ, through LC-MS/MS. Lines between nodes represent interactions found in the STRING database, with colours denoting how the interaction was identified as described in the legend. The number of interactions is higher than would be expected from a random set of proteins (PPI enrichment p-value=0.00983). Functional enrichments in the cytoskeleton (blue) and the proteasome (red) are shown (FDR=0.033 and 0.0038 respectively).*

6.3 Confirmation of COBL Expression *in vivo* and in C2C12 Myoblasts

COBL is a protein containing tandem repeats of WASP-homology 2 (WH2) domains, these domains are multifunctional regulators of actin assembly. They contribute to filament nucleation, severing, and barbed end capping or tracking, depending on the context in which they are found (Carlier et al., 2011). COBL specifically has been shown to play a role in development including in neural tube formation (Carroll et al., 2003), as well as playing a role in promoting the growth of brush border microvilli in the intestine (Grega-Larson et al., 2015). No specific function has been found for COBL in skeletal muscle thus far.

The specificity of a COBL antibody was tested to determine if it could be used to reveal the localisation of COBL *in vivo* and *in vitro* (fig.6.3). SDS-PAGE and western blots were performed on samples from the soluble fraction of mouse brain, heart, skeletal muscle, and 7-day differentiated C2C12 cells. A complex band pattern was observed. Initially it was assumed that this represented a number of COBL isoforms, and that the full-length COBL isoform was represented by a band at ~144kDa, its predicted molecular weight. However, upon examining the literature (Ahuja et al., 2007; Haag et al., 2018), and through the generation of a C2C12-derived COBL knockout cell line (outlined in chapter 7.5), it was determined that the band at ~170kDa was the genuine COBL band (fig.6.3A). COBL was shown to be expressed in the brain (as expected) and in myoblast cells. However, expression was not apparent in the soluble fraction of skeletal muscle or the heart. It is possible that COBL is not found in the soluble fraction of skeletal muscle due to a strong association with the cytoskeleton. Insoluble COBL may be detected in skeletal muscle through antibody staining, rather than through western blots.

Longitudinal sections of mouse gastrocnemius muscle that had been electroporated with a KY-tdTomato construct, to mark the z-disc, were incubated with anti-COBL antibody (fig 6.3B). Co-localization of KY-tdTomato and COBL indicate that COBL may be localized to the Z-disc where IGFN1 is also expressed. However, due to the lack of isoform specificity, and potential cross-reactivity observed from this COBL antibody, it could not be determined

whether this was indeed COBL at the z-disc. To confirm this localisation, and to perform other interaction assays, COBL was to be cloned into a mammalian expression vector containing a fluorescent tag, as described below.
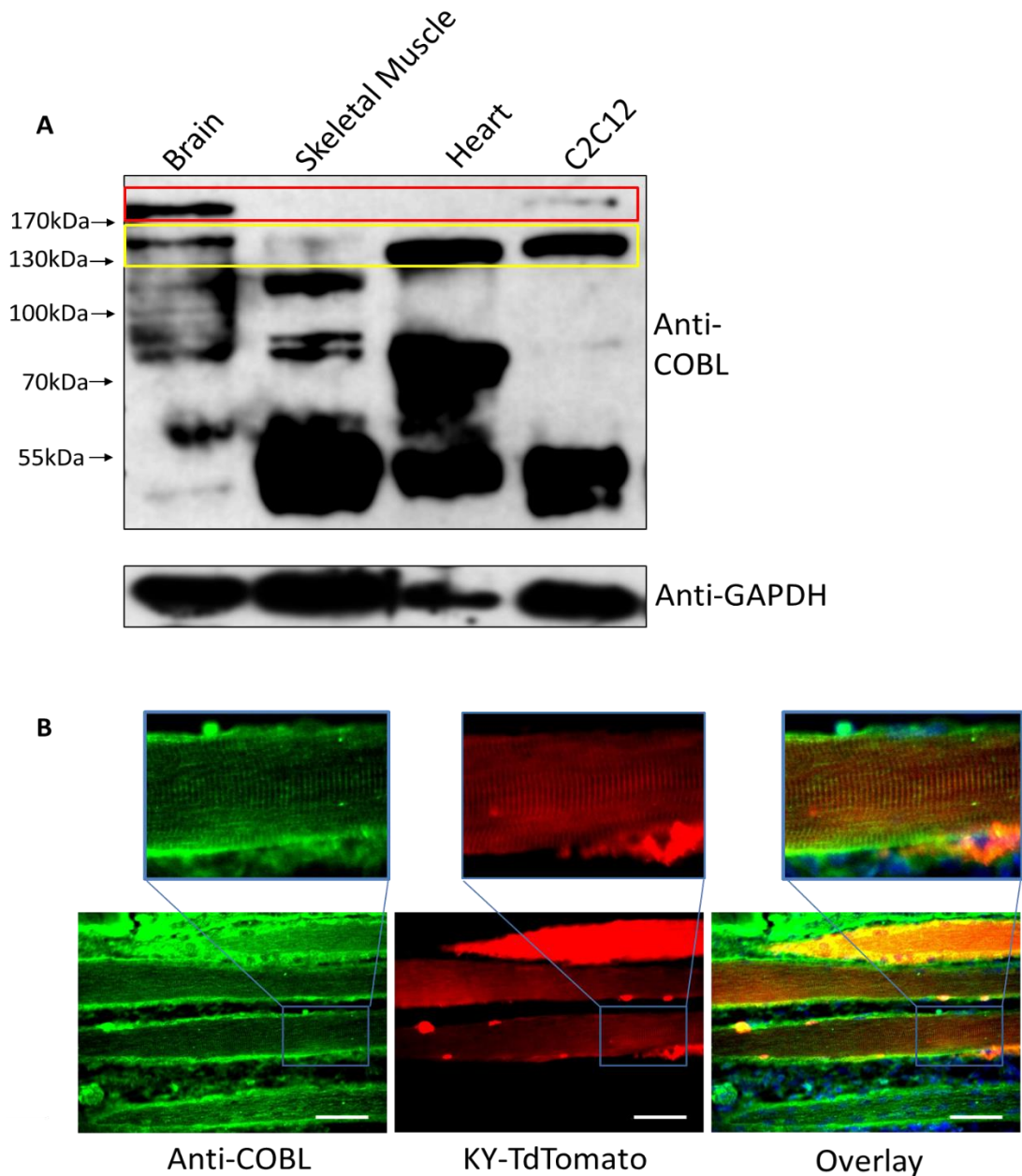
Figure 6.3 COBL antibody validation. A) *Anti-COBL western blot with samples from the soluble fraction of mouse brain, heart, and skeletal muscle, and 7-day differentiated C2C12 cells. Yellow box indicates bands at the approximate predicted size of full-length COBL (~144kDa), red box indicates the band confirmed to represent full-length COBL (~170kDa).* **B)** *Widefield longitudinal cross-sections of mouse gastrocnemius muscle. Sections are from mice electroporated with a KY-tdTomato vector to identify the z-disc (red) and incubated with anti-COBL antibody (green). Note that COBL antibodies identify a striated pattern that coincides with the z-disc. The insets (blue squares) are shown magnified above. Scale bar represents 50 microns.*

6.4 Cloning of *cobl* into Gateway vectors

To provide a tool for further validation of the potential interaction between IGFN1 and COBL, and because of the lack of antibody specificity, a mouse muscle cDNA library was used to amplify *cobl* transcripts present in muscle. Primers compatible with the TOPO cloning system were used (fig.6.4A, B). Several amplicons were amplified including the full length *cobl* isoform (COBL-201) matching the larger isoform observed in figure 6.3A, and a number of smaller amplicons representing either non-specific amplification, or smaller COBL isoforms (fig. 6.4C). The resulting PCR product was cloned into the pENTR/SD/D-TOPO vector, using the pENTR Directional cloning TOPO Cloning Kit (Invitrogen), the vectors produced were then transformed into chemically competent *E. coli*.

Colony PCR was performed to identify colonies containing a *cobl* insert (fig. 6.5A), followed by minipreps and a double restriction digest to identify the size of the *cobl* insert (fig. 6.5B). Only 1/40 of the colonies screened contained the full length *cobl* insert. This colony was grown in LB in order to perform a miniprep to extract the pENTR/SD/D-TOPO vector containing an insert coding for the full length COBL isoform. This construct was then used to shuttle the full length *cobl* insert into the "Gateway" compatible destination vector containing a tdTomato C-terminal tag: pDEST47-tdTomato. The presence of an ORF was confirmed via transfection of the COBL-tdTomato construct into COS7 cells. The resulting red fluorescence likely indicates translation of a full length in frame fusion of COBL and tdTomato, although the presence of alternative translation starts within the COBL ORF cannot be ruled out (fig. 6.6A). The construct was then sequenced using primers spaced at 500bp intervals along the ORF, this confirmed that the insert was indeed the *cobl* isoform COBL_201 (UniProt identifier: Q5NBX1-1) (fig. 6.6B). Sequencing of the smaller inserts (seen in fig. 6.5B) was unable to identify any as COBL isoforms, meaning that these were likely artefacts, rather than isoforms of COBL.
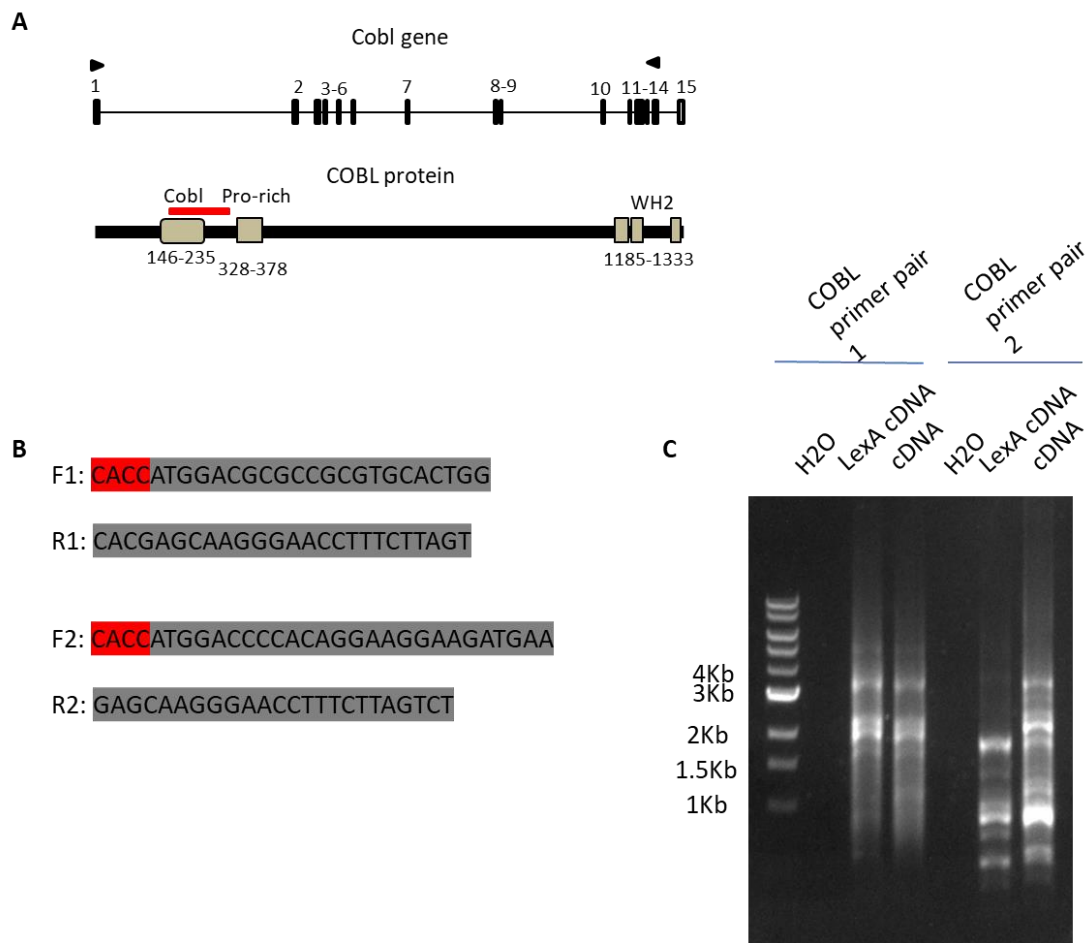
Figure 6.4 Amplification of COBL from a mouse muscle cDNA library. A) *Above,*
intron/exon structure of the mouse Cobl gene with exons numbered according to the
predicted ENSEMBL Cobl-201 (ENSMUST00000046755.13). ENSEMBL Cobl-201
matches the sequence from the mouse cDNA amplified from a skeletal muscle library
using the indicated primers (arrow tips). The mouse skeletal muscle cDNA predicts a
protein of 1337 AA identical to UniProtKB Q5NBX1. Below, the mouse COBL protein
with domains annotated as follows: Cobl, ubiquitin-like fold domain (IPR019025); Pro-
rich, indicates a proline rich region (compositional bias); WH2, Wiskott-Aldrich
homology 2 domain (IPR003124). The antigen used for anti-Cobl antibodies is
indicated by the red bar. **B)** *Sequence of two sets of primers designed to amplify*
COBL, grey represents sequence complementary to cobl gene, red represents CACC
sequence required for cloning into pENTR/SD/D-TOPO vectors. Primer pair 1
designed to amplify entire ORF excluding the stop codon, primer pair 2 skips 9 5'
codons and 2 3' codons (including the stop codon) in order to increase primer
efficiency. **C)** *PCR amplification with NEB Q5 high fidelity DNA polymerase (to*
produce blunt ends for TOPO cloning) using both primer pairs on two cDNA libraries;

lexA (human) and cDNA (mouse) bands are present in both libraries at expected sizes for a number of COBL isoforms. PCR product from primer pair 1 was taken forward for cloning into pENTR/SD/D-TOPO as it contains the complete cobl ORF.
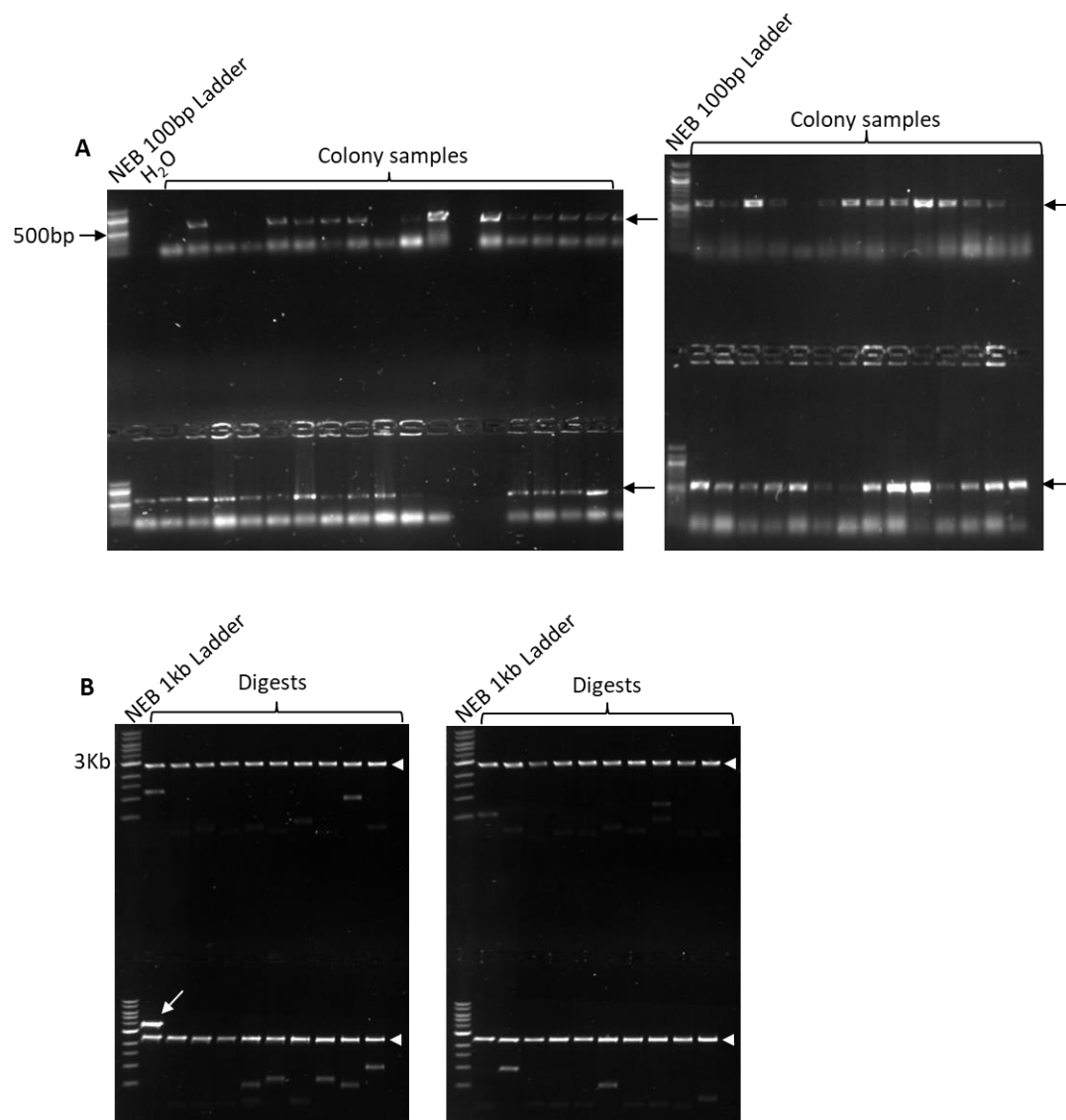
Figure 6.5. Validation of cobl cloning into pENTR/SD/D-TOPO. A) *Colony PCR of E. coli transformed with pENTR-COBL using primers spanning exons 11 and 12 of the cobl transcript. Confirmation of presence of cobl in majority of the transformants with a band at 585bp (black arrows).* **B)** *Double restriction digests (using BsrGI) of plasmid DNA following minipreps from cobl positive colonies in A. The band at ~2.5Kb represents the vector backbone (white arrowheads). Inserts of various sizes were observed as expected, one construct contained an insert of the predicted size of the full-length cobl isoform at ~4Kb (white arrow).*
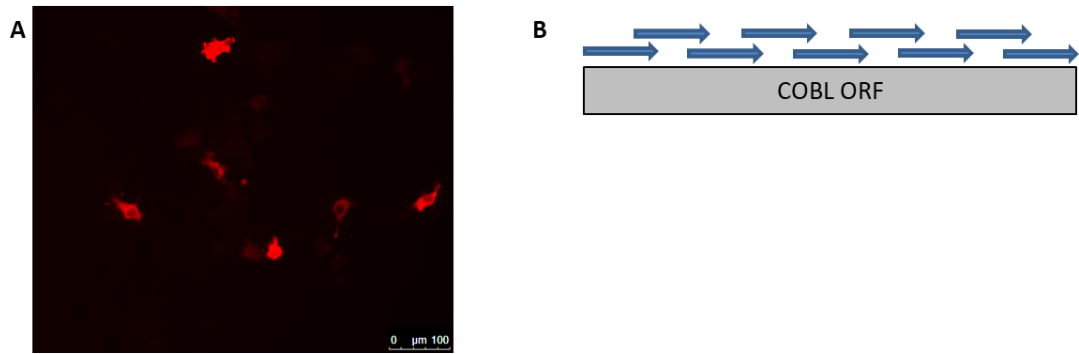
Figure 6.6. Validation of destination vectors containing cobl inserts. A) *COS7 cells were transfected with the pDEST47-COBL-TdTomato construct, fluorescence indicates the presence of an open reading frame.* ***B)*** *Schematic of sequencing strategy, primers were designed at ~500bp intervals along the cobl full length open reading frame, each primer gave a sequence length of ~1000bp meaning that sequences could be assembled using the overlapping regions, this allowed confirmation that a full-length cobl ORF was present.*

6.5 IGFN1_V1 and COBL Co-immunoprecipitate Following Co-transfection in COS7

To test the specificity of the IGFN1-COBL interaction COS7 cells were co-transfected with either pDEST47-IGFN1_V1-V5 and pDEST47-COBL-tdTomato or with pDEST47-V5 and pDEST47-COBL-tdTomato and were left for 48 hours to express the transfected constructs. Cells were then lysed, and this lysate was incubated against either anti-V5 IgG agarose beads or IgG Agarose beads. Beads were then washed and processed via SDS-PAGE and a western blot performed with the anti-COBL antibody, followed by stripping and reprobing with anti-V5 antibody. A band at the expected molecular weight of COBL-tdTomato was detected in samples from COS7 cells transfected with pDEST47-IGFN1_V1-V5 and pDEST47-COBL-tdTomato confirming that the two proteins interact (fig. 6.7). A lack of COBL bands in the with pDEST47-V5 and pDEST47-COBL-tdTomato samples rules out non-specific binding of COBL to the V5 tag, and the lack of bands in the IgG Agarose bead samples rules out non-specific binging of COBL or tdTomato to the beads themselves, indicating that the interaction between COBL and IGFN1_V1 is likely to be specific.

127
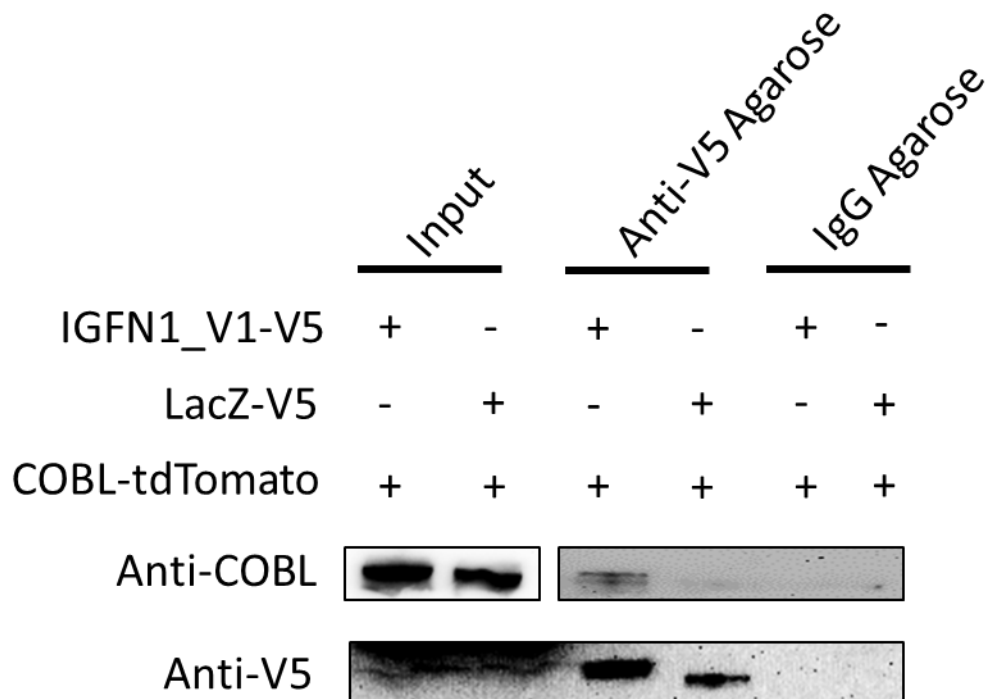
Figure 6.7. IGFN1_V1 and COBL coimmunoprecipitate following IgG Agarose bead pull-down. *Representative blots are shown from pulldowns of cell extracts from COS7 cells co-transfected with either pDEST47-IGFN1_V1-V5 and pDEST47-COBL-tdTomato or with pDEST47-V5 and pDEST47-COBL-tdTomato to control for non-specific binding between the two tags. Pull-downs were performed against either anti-V5 IgG agarose beads or IgG Agarose beads as a control for protein binding directly to the beads. Blots were incubated with anti-COBL antibody before being stripped and re-probed with anti-V5 antibody. A band is present at the expected size of COBL-tdTomato in the pDEST47-IGFN1_V1-V5 and pDEST47-COBL-tdTomato co-transfection extract but not in the pDEST47-V5 and pDEST47-COBL-tdTomato co-transfection extract suggesting a specific interaction between IGFN1_V1 and COBL. Transfections and pull-downs were repeated in triplicate.*

6.6 COBL and IGFN1_V1 Co-localise in COS7 Cells

In order to look for possible changes in the subcellular localization of these proteins when co-transfected in a heterologous system, COS7 cells were transfected with either pDEST47-IGFN1_V1-GFP and pDEST47-COBL-tdTomato or pDEST47-IGFN1_V1-GFP and pDEST47-tdTomato. Initial analysis concerned the location of IGFN1_V1 and COBL expression. For singly transfected cells, IGFN1_V1 was found to be highly expressed in the nucleus of cells only expressing IGFN1_V1-GFP whilst COBL-tdTomato was expressed predominantly in the cytoplasm. However, in cells expressing both IGFN1_V1-GFP and COBL-tdTomato a shift of IGFN1_V1-GFP expression was observed with a higher proportion of cells expressing IGFN1_V1-GFP in the cytoplasm, suggesting that COBL may prevent IGFN1_V1 from translocating to the nucleus. This nuclear to cytoplasmic expression shift for IGFN1_V1-GFP was not observed in cells co-transfected with IGFN1_V1-GFP and tdTomato (fig. 6.8).

Confocal microscopy was then used in order to quantify the levels colocalization for IGFN1 and COBL in COS7 cells transfected with either pDEST47-IGFN1_V1-GFP and pDEST47-COBL-tdTomato or pDEST47-IGFN1_V1-GFP and pDEST47-tdTomato. Volocity software was used to quantify the Pearson's correlation coefficient, with the Costes method (Costes et al., 2004) used for setting thresholds. It was found that the Pearson's correlation coefficient was significantly higher in the pDEST47-IGFN1_V1-GFP and pDEST47-COBL-tdTomato transfected cells than in the or pDEST47-IGFN1_V1-GFP and pDEST47-tdTomato transfected cells (fig. 6.9) showing that IGFN1_V1 and COBL interact and colocalise even outside of the context of a muscle cell.

Attempts were made to co-transfect and express pDEST47-IGFN1_V1-GFP and pDEST47-COBL-tdTomato in C2C12 cells. However, the transfection efficiency was very low, meaning that no cells expressing both IGFN1_V1-GFP and COBL-tdTomato could be observed. To circumvent this the interaction of IGFN1_V1 and COBL was explored *in vivo* using electroporations of adult mouse muscles
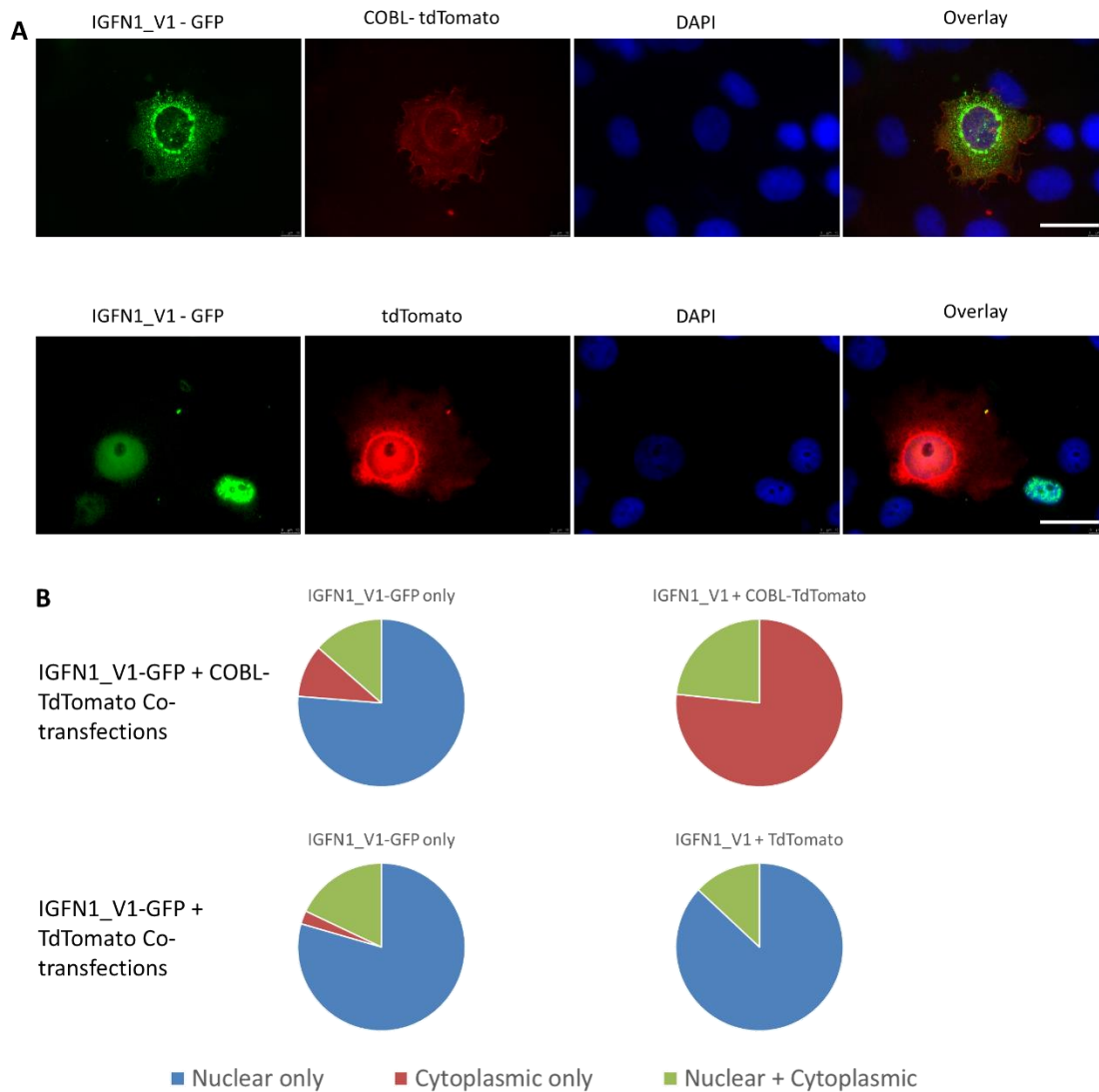
Figure 6.8. Localisation of IGFN1_V1 shifts from nuclear to cytoplasmic in the presence of COBL in COS7 cells. A) *Representative widefield images of COS7 cells co-transfected with either pDEST47-IGFN1_V1-GFP and pDEST47-COBL-tdTomato or with pDEST47-IGFN1_V1-GFP and pDEST47-tdTomato. IGFN1_V1-GFP is localised to the nuclei of cells co-transfected with pDEST47-tdTomato, cytoplasmic expression is observed in cells co-transfected with pDEST47-COBL-tdTomato. Scale bar represents 30 microns.* **B)** *Quantification of IGFN1_V1-GFP localisation in COS7 cells co-transfected with either pDEST47-IGFN1_V1-GFP and pDEST47-COBL-tdTomato or with pDEST47-IGFN1_V1-GFP and pDEST47-tdTomato. IGFN1_v1-GFP distribution is similar in cells expressing IGFN1_V1-GFP alone and in cells expressing both IGFN1_V1-GFP and tdTomato with mainly nuclear localisation observed. In cells expressing both IGFN1_V1 and COBL-tdTomato a higher proportion of cytoplasmic expression is observed (n>30 in each condition).*
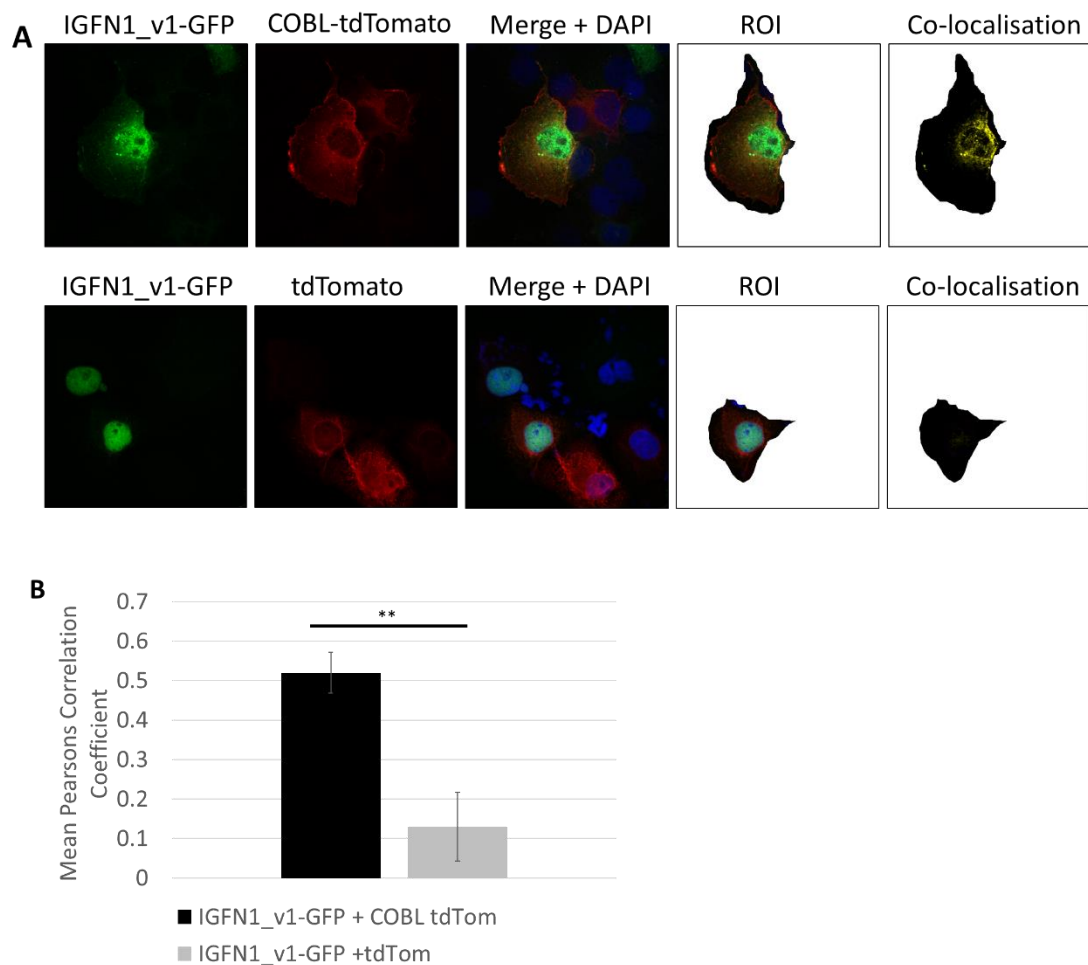
Figure 6.9. IGFN1_V1-GFP colocalises with COBL-tdTomato in COS7 cells. A) *Representative widefield images of COS7 cells co-transfected with either pDEST47-IGFN1_V1-GFP and pDEST47-COBL-tdTomato or with pDEST47-IGFN1_V1-GFP and pDEST47-tdTomato. The selected range of interest (ROI) for individual cells expressing both constructs are shown as are images showing pixels where co-localisation is apparent.* ***B)*** *Mean Pearson's correlation coefficient values. Volocity software was used for analysis with the Costes method used to set thresholds. For cells co-transfected with pDEST47-IGFN1_V1-GFP and pDEST47-COBL-tdTomato n=25 and for cells transfected with pDEST47-IGFN1_V1-GFP and pDEST47-tdTomato n=12. Colocalisation was significantly higher in cells co-transfected with pDEST47-IGFN1_V1-GFP and pDEST47-COBL-tdTomato than cells transfected with pDEST47-IGFN1_V1-GFP and pDEST47-tdTomato (students t-test, p<0.01).*

6.7 COBL and IGFN1_V1 are Present at the Z-disc *in vivo*

The TA/EDL muscles of C3H/HeH mice were electroporated with either pDEST47-COBL-tdTomato, pDEST47-IGFN1_V1-GFP and pDEST47-COBL-

tdTomato, or pDEST47-IGFN1_V1-GFP and pDEST47-tdTomato to investigate the interaction between IGFN1_V1 and COBL *in vivo* and establish whether the z-disc localisation in figure 6.3B was genuine. Following 10 days of expression longitudinal sections were made of the EDL of electroporated mice. Unfortunately, the co-electroporations of IGFN1_V1-GFP and COBL-tdTomato were unsuccessful. However, in sections from mice electroporated with COBL-tdTomato alone, clear striations were observed, as had previously been observed using anti-COBL antibodies (fig. 6.3B). In order to confirm that the striations observed were from COBL-tdTomato expression at the z-disc the sections were incubated with EA-53, an anti α-actinin antibody. Confocal analysis of these sections revealed that the expression of COBL in the electroporated muscles was localised to the z-disc with the striations observed from COBL-tdTomato aligning with those from the anti α-actinin antibody (fig. 6.10).

| COBL-tdTomato | EA-53 (α-actinin) | Merge + DAPI |
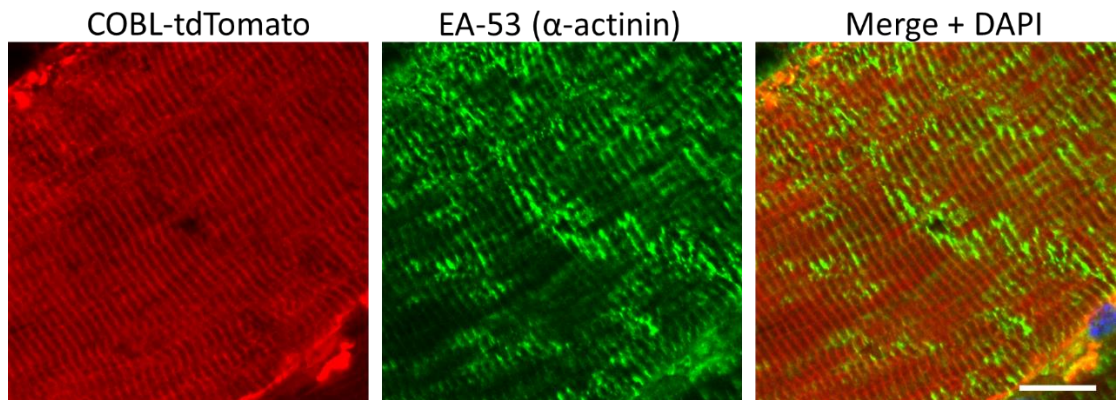
Figure 6.10. COBL localises to the Z-disc in vivo. *Mouse EDL muscles were electroporated with pDEST47-COBL-tdTomato. After 10 days mice were euthanised and longitudinal sections of the electroporated EDL muscle were taken. In order to visualise the z-disc sections were stained with the anti-sarcomeric alpha actinin antibody EA-53 using the secondary antibody anti-mouse IgG Alexa Fluor 488. Images were taken using a Zeiss Upright 710 confocal microscope (confocal slice). Scale bar represents 15 microns.*

6.8 Conclusions

Initial proteomic analysis revealed a functional enrichment in the cytoskeleton with potential interacting partners including the z-disc protein α-actinin (Actn1). This gave an indication that the interactions detected were specific as they were consistent with the z-disc localisation of KY, the bait originally used to identify IGFN1 (Beatham et al., 2004b), which was also found to localise to the z-disc (Baker et al., 2010). Functional enrichments in the proteasome were also detected through proteomic analysis of the pull-down of mouse muscle extract against IGFN1 fragments. IGFN1 expression has previously been associated with muscle atrophy (Chen et al., 2014; Rahimov et al., 2011) meaning these potential interactions may provide an insight into any function IGFN1 plays in atrophy. A similar approach to validating these interactions as used for COBL and IGFN1 should be explored in future work.

As shown in chapter 3, IGFN1 knockout cells display a fusion defect, as well as a higher G:F actin ratio than wildtype cells. Additionally, IGFN1 was shown to interact with actin in a Y2H screen (Baker et al., 2010). Actin remodelling plays a pivotal role in all steps of myoblast fusion: migration, recognition, adhesion, membrane alignment and membrane pore formation and resolution (Rochlin et al., 2010). Therefore, validation of the interaction between IGFN1 and COBL was of particular interest because of its numerous roles in actin remodelling in other tissues, including neural tube formation (Carroll et al., 2003), as well as playing a role in promoting the growth of brush border microvilli in the intestine (Grega-Larson et al., 2015). While no role for COBL has been identified in skeletal muscle thus far. It is possible that COBL plays a role in cytoskeletal remodelling especially during myoblast fusion and development. IGFN1 may regulate COBL activity by acting as a scaffold.

Previous findings have suggested that COBL expression in skeletal muscle is relatively low (Ahuja et al., 2007; Carroll et al., 2003). Indeed, the western blot showed here would support this. However, COBL was identified by LC-MS/MS from a skeletal muscle extract following pull-down experiments, and COBL was cloned from a mouse skeletal muscle cDNA library, suggesting that it is expressed at some level in skeletal muscle. It may be that COBL is not found in the soluble fraction and is only detectable in the cytoskeletal fraction of muscle protein extracts. Furthermore, COBL was shown here to be expressed in differentiating myoblasts, and is known to be expressed in the somites of zebrafish 24hpf (Schuler et al., 2013), at a similar time as Myomerger (Shi et al., 2017) and MyoD (Weinberg et al., 1996). This raises the possibility that COBL is upregulated in skeletal muscle during myoblast fusion. This may occur in the developing embryo and/or in adult skeletal muscle in response to injury.

The interaction between IGFN1 and COBL was validated through pull-down and co-localisation experiments. As well as this, COBL was shown to localise to the z-disc *in vivo*. It is significant that interactions between IGFN1 and COBL were detected in COS7 cells, this demonstrates that the two proteins interact outside of the context of a muscle cell and therefore the interaction is likely to

be direct. It is also noteworthy that COBL promotes actin assembly at the barbed end of the actin filament (Ahuja et al., 2007), and that sarcomeric actin filaments are orientated such that the barbed ends are anchored at the z-disc (Ono, 2010). These observations indicate that the localisation of COBL to the z-disc *in vivo* is potentially functionally relevant.

The research presented in this chapter outlines a novel interaction between IGFN1_V1 and the actin nucleator COBL in skeletal muscle, with evidence to suggest that this interaction occurs at the z-disc. This interaction may provide an insight into the underlying causes of the actin remodelling phenotype observed in IGFN1_V1 knockout cells as well as the fusion defect observed.

CHAPTER 7: INVESTIGATING A ROLE FOR COBL IN MYOBLAST FUSION AND DIFFERENTIATION

Chapter 7: Investigating a Role for COBL in Myoblast Fusion and Differentiation

7.1 Introduction

This chapter describes experiments performed to examine the role of COBL in muscle cells, in particular during myoblast fusion and differentiation.

The previous chapter details the identification of COBL as an interaction partner of IGFN1 in skeletal muscle. COBL contains multiple WH2 domains, involved in actin filament nucleation, severing, and barbed end capping or tracking, depending on the context in which they are found (Carlier et al., 2011). Overexpression and knockdown experiments have revealed a role for COBL in dendritogenesis of dissociated hippocampal neurons and of cerebellar Purkinje cells (Ahuja et al., 2007; Haag et al., 2012). COBL has also been implicated in the formation of microvilli (Grega-Larson et al., 2015; Wayt and Bretscher, 2014).

In vivo, a zebrafish knockout model displays impaired swimming and balance keeping, caused by defects in the development of sensory hair cells (Schuler et al., 2013). Most recently, a COBL knockout mouse line has demonstrated a role for COBL in postnatal planar cell polarity refinement and cochlea function, with knockout mice having impaired hearing (Haag et al., 2018). No stringent examination of the skeletal muscle of COBL knockout mice (Haag et al., 2018) has thus far been reported. Clearly COBL plays diverse roles across several tissues, with no specific role for COBL elucidated in skeletal muscle at this time.

Given its interaction with IGFN1, and the actin remodelling, and fusion phenotypes observed in IGFN1 knockout cells, it is possible that COBL acts as an effector of IGFN1 in remodelling the cytoskeleton during myoblast fusion and differentiation. Here the role of COBL in myoblast fusion and differentiation is investigated. First, by examining its expression profile throughout differentiation. Followed by examining morphological changes induced by COBL in C2C12 cells. Finally, a CRISPR/Cas9 knockout cell line is developed and characterised.

7.2 COBL Expression Changes Throughout Differentiation and is Affected by IGFN1

For COBL to play a role in myoblast fusion and differentiation it must be expressed during these processes. Therefore, the expression of COBL at both the protein and transcript level was investigated throughout fusion and differentiation. This was performed for both wildtype and IGFN1 knockout cells to determine whether IGFN1 influences COBL expression.

SDS-PAGE followed by western blotting revealed that the largest COBL isoform, a band migrating to ~170kDa, was not detectable in proliferating myoblasts of either cell type (fig.7.1). Although this band does not appear at the predicted molecular weight of full-length COBL (~144kDa) it has been previously reported to be the full-length COBL isoform (Ahuja et al., 2007; Haag et al., 2018), and is confirmed by CRISPR/Cas9 knockout (below). COBL protein expression was apparent at full confluency (D0, before addition of differentiation media) in both cell types and was maintained throughout differentiation (fig.7.1). This demonstrates that COBL protein expression is associated with the myoblast fusion and differentiation programmes. COBL expression did appear more variable in IGFN1 knockout cells maintained in differentiation media for 7 days, but the direction of the change in expression was not consistent between blots (fig.7.1).
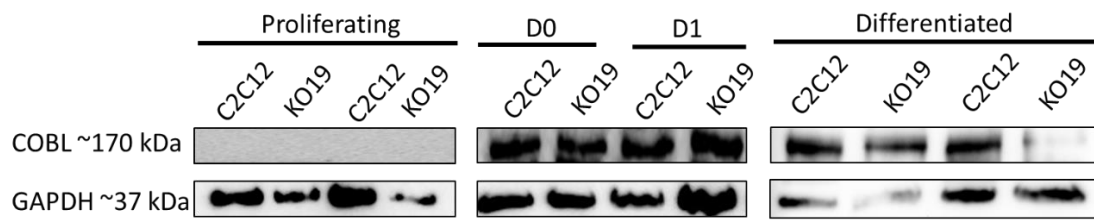
Figure 7.1 COBL protein expression throughout in vitro differentiation.
Representative anti-COBL western blots from wildtype C2C12 (C2C12), and IGFN1
knockout (KO19) cells at the following time points: proliferating (P), fully confluent
(D0) in differentiation medium for one (D1) or seven (D7) days. Two independent
samples are shown for each cell line/timepoint from a total of 4 repeats.

A very different COBL expression pattern is observed at the transcript level,
especially in the IGFN1 knockout cell line, as shown through qPCR. In wildtype
cells, COBL transcript expression remains relatively stable throughout
differentiation (fig.7.2A). In IGFN1 knockout cells, COBL transcript expression
is higher than in wildtype cells at every timepoint observed, with the difference
growing as differentiation progresses (fig.7.2A). As expected, the IGFN1
knockout cell line had drastically lower expression of the differentiation marker
myosin heavy chain 7 (MYH7) at day 7 of differentiation (fig.7.2B), further
emphasising the role of IGFN1 in myoblast differentiation. Taken together
these results suggest that IGFN1 plays a role in the regulation of COBL
expression, and that this may be important during myoblast fusion and
differentiation.

A

COBL mRNA Expression

B

MYH7 mRNA Expression
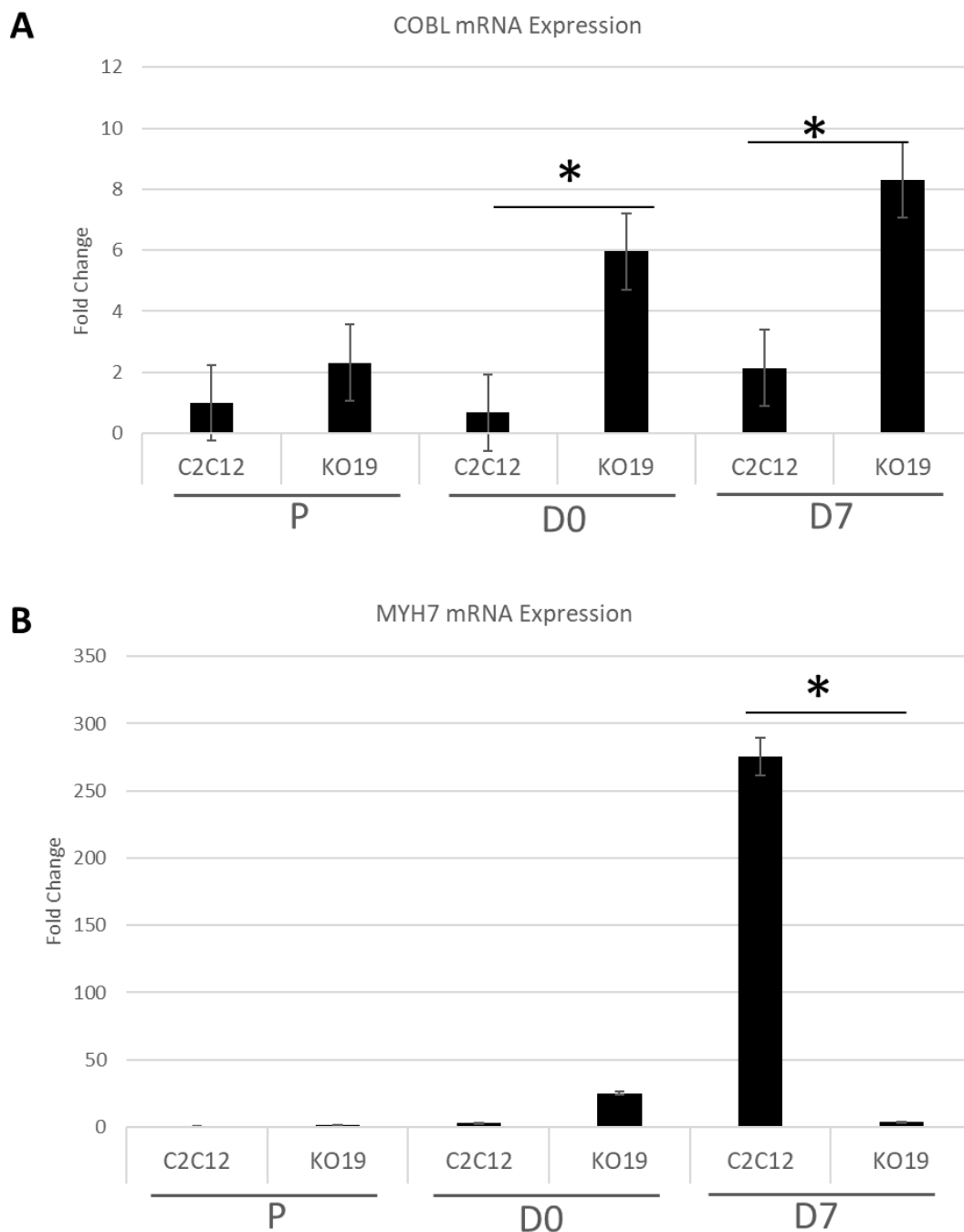
Figure 7.2 COBL transcript expression throughout in vitro differentiation. A) *qPCR analysis from wild type (C2C12) and IGFN1 knockout cells (KO19) at the indicated growing conditions. Fold changes compared to C2C12 proliferating cells were calculated using the ΔΔCt method relative to the housekeeping gene HPRT. A statistically significant interaction between cell type and time point on Ct values was shown by one way ANOVA [F(5,12)=11.5 p<0.001], post-hoc comparisons (Tukey HSD) revealed COBL expression was significantly higher in confluent (D0, *p<0.01)*

*and differentiating (D7, *p<0.05) KO19 cells. **B)** Relative MYH7 expression as differentiation marker in C2C12 and KO19 cells. One way ANOVA revealed that there is a statistically significant interaction between cell type and time point on Ct values [F(5,12)=68.4 p<0.001]. Post-hoc comparisons using Tukey HSD revealed that at D7 of differentiation MYH7 expression was significantly higher in C2C12 cells (*p<0.01).*

7.3 COBL Colocalises with Actin and Affects the Morphology of C2C12 Myoblasts

Previous work has shown that COBL induces the formation of actin-rich ruffles in COS7 cells (Ahuja et al., 2007). A similar effect was observed here in the context of a muscle cell, where C2C12 cells were transfected with pDEST47-COBL-tdTomato. Actin-rich protrusions were observed in COBL transfected cells (fig 7.3A) this was accompanied by high levels of colocalization between F-actin and COBL (fig 7.3B). This was not observed in pDEST47-tdTomato transfected cells.

To quantify the morphological changes induced by COBL expression in C2C12 myoblasts, the circularity of cells transfected with either pDEST47-COBL-tdTomato or pDEST47-tdTomato was measured using the analyse particles tool in ImageJ. This method was selected as an objective way of measuring the changes in morphology induced by COBL expression, as opposed to the more subjective counting of ruffles. Circularity of pDEST47-COBL-tdTomato transfected cells was significantly lower than that of pDEST47 -tdTomato transfected cells (fig 7.4), reflecting an increase in cellular protrusions as a result of COBL expression. The above experiments were also attempted in IGFN1 knockout cells, to determine whether IGFN1 was required for COBL to affect the morphology of the myoblast. Unfortunately, these experiments were not successful. Transfection of IGFN1 knockout cells with pDEST47-COBL-tdTomato resulted in cell death or detachment from the growth surface, with very low transfection efficiencies in the cells which remained attached.

A

| | tdTomato | CruzFluor 488 | Merge+DAPI |

COBL-tdTomato + phalloidin green

tdTomato + phalloidin green

B
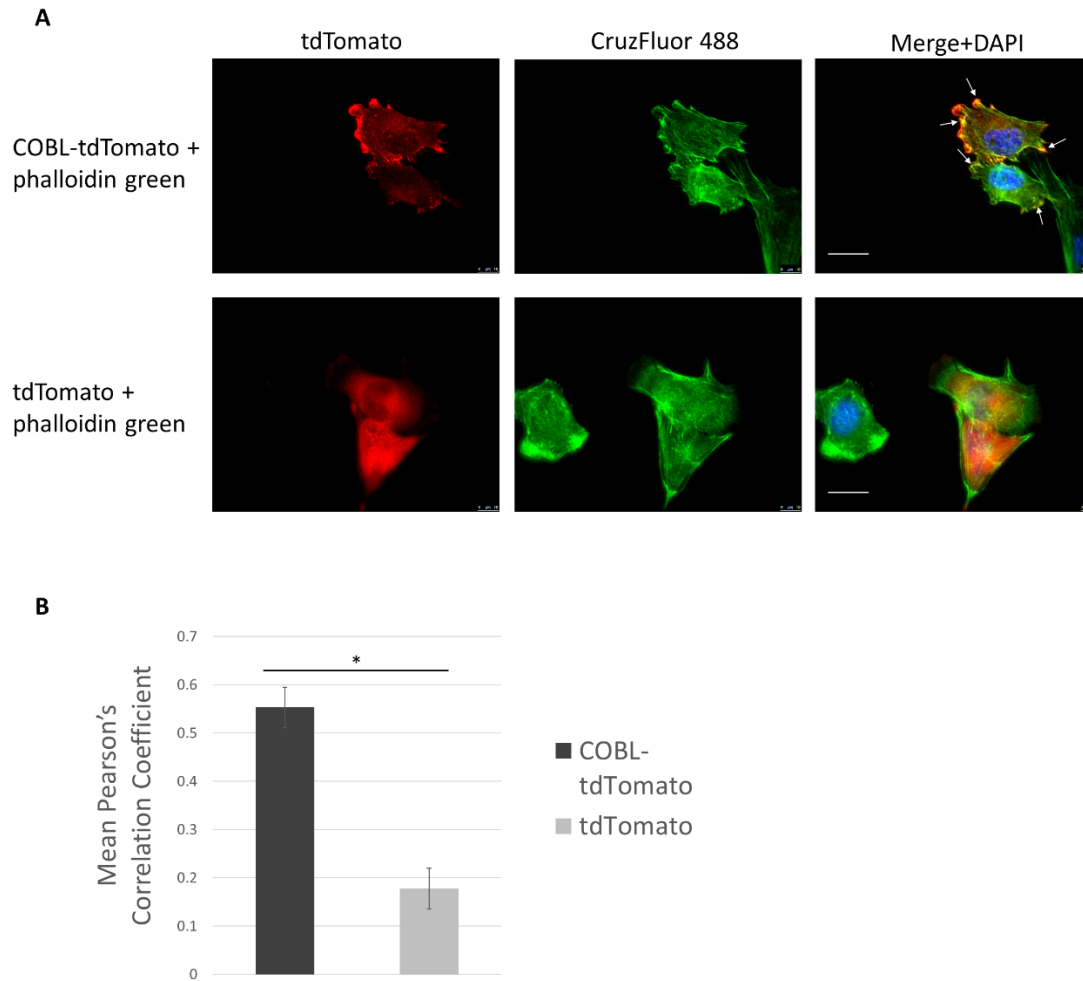
Figure 7.3 COBL colocalises with F-actin in actin-rich cellular protrusions in myoblasts. A) Representative widefield images of C2C12 cells transfected with either pDEST47-COBL-tdTomato or pDEST47-tdTomato, then stained with phalloidin (F-actin) and DAPI (nucleus). Arrows indicate actin and COBL rich protrusions. Scale bar represents 20 microns. B) Mean Pearson's correlation coefficient values for colocalization of COBL and F-actin. Volocity software was used for analysis with the Costes method used to set thresholds. Mean Pearson's correlation coefficient was significantly higher for pDEST47-COBL-tdTomato transfected cells than for pDEST47-tdTomato transfected cells (n=30, p<0.01).
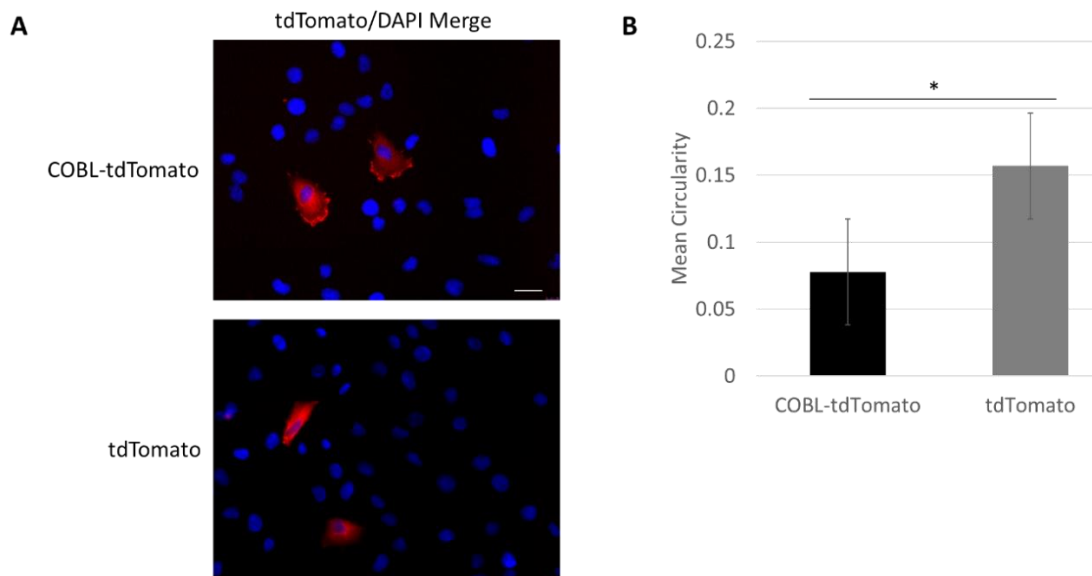
Figure 7.4 COBL overexpression reduces circularity in C2C12 myoblasts. *A) Representative widefield images of C2C12 cells transfected with either pDEST47-COBL-tdTomato or pDEST47-tdTomato. Scale bar 50 microns. B) Mean circularity quantified using ImageJ. Mean circularity was significantly lower for pDEST47-COBL-tdTomato transfected cells than for pDEST47-tdTomato transfected cells (n≥40, p<0.01).*

7.4 COBL Overexpression Increases Myoblast Fusion

To examine the effect of COBL overexpression on the differentiation of myotubes pDEST47-COBL-tdTomato and pDEST47-tdTomato transfected C2C12 cells were differentiated for 7 days. At day 7 cells were fixed and the number of nuclei within a cell expressing either COBL-tdTomato or tdTomato alone was counted. The fusion index of these cultures could not be calculated because not every cell in each frame expressed the transfected constructs. It was observed that pDEST47-COBL-tdTomato expressing myotubes contained significantly more nuclei than pDEST47-tdTomato expressing myotubes, suggesting that COBL induces myoblast fusion (fig 7.5).

A tdTomato/DAPI Merge

COBL-tdTomato

tdTomato

B

Mean Number of Nuclei
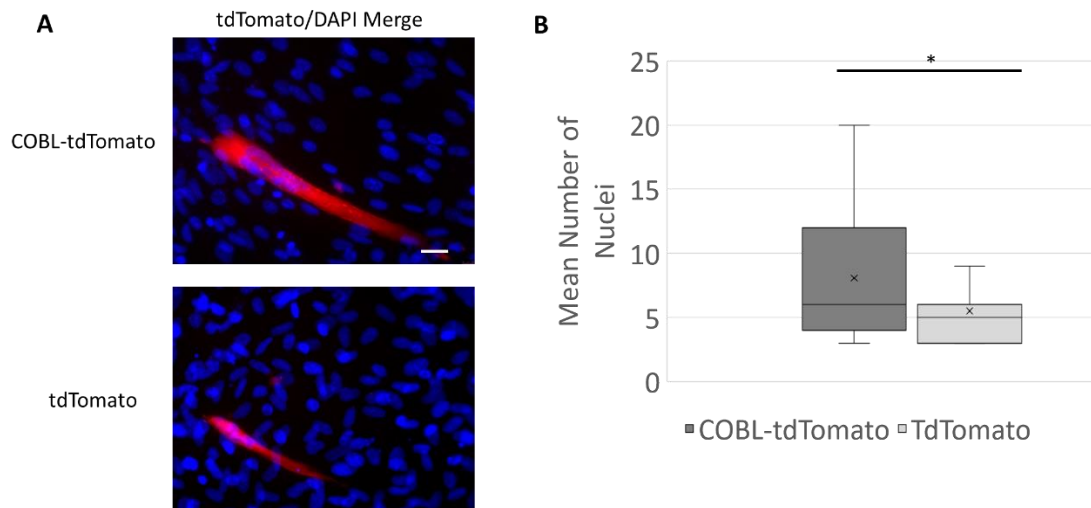
Figure 7.5. COBL overexpression increases myoblast fusion. A)
Representative widefield images of C2C12 cells transfected with either pDEST47-
COBL-tdTomato or pDEST47-tdTomato and differentiated for 7 days. Scale bar
represents 50 microns. B) Mean number of nuclei within a pDEST47-COBL-tdTomato
or pDEST47-tdTomato expressing myotube (minimum of 3 nuclei to exclude non-
fusing cells). The mean number of nuclei (crosses) was significantly higher in
pDEST47-COBL-tdTomato expressing myotubes than in pDEST47-tdTomato
expressing myotubes (n≥50, p<0.01). A minimum of 4 independent transfections were
performed per condition.

Next, the localisation of COBL during myoblast fusion and differentiation was
examined. pDEST47-COBL-tdTomato transfected cells were differentiated for
4 days before being fixed and stained with phalloidin. Figure 7.6 shows an
example of COBL and F-actin accumulation along the membrane of a myotube
with an adjacent myoblast, which may be a precursor to fusion. These events
were relatively rare, probably reflecting their transient nature. However, this
does suggest that COBL is located in the right place at the right time to be
involved in myoblast fusion.
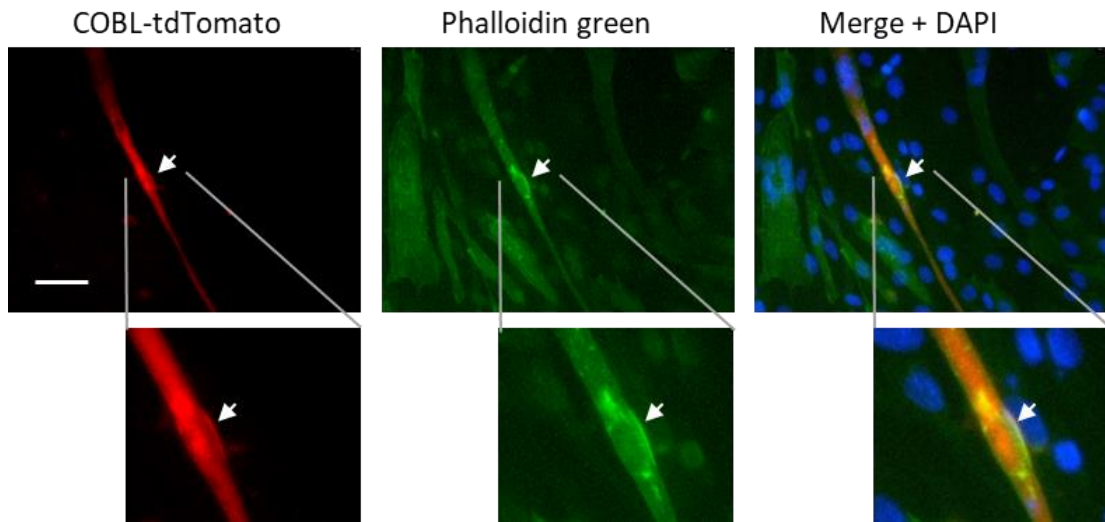
Figure 7.6. COBL and F-actin colocalise along the membrane of myotubes. *pDEST47-COBL-tdTomato transfected cells at 4 days of differentiation stained with phalloidin and DAPI. White arrowheads indicate expression of COBL and F-actin along the cell membrane in close proximity to a myoblast aligned with the myotube. Scale bar represents 100 microns.*

7.5 Generation of a C2C12-derived COBL Knockout Cell Line

A COBL knockout C2C12-derived cell line was generated to examine the effects of COBL deficiency, especially on myoblast fusion, and to determine whether a similar phenotype as in the IGFN1 knockout cells would be observed. To this end, two cocktails of pre-designed plasmids were ordered (sc-419728 and sc-419728-HDR, Santa Cruz). The first cocktail contained three plasmids coding for three unique CRISPR/Cas9 gRNAs (targeting exons 2, 3, and 4), and the Cas9 enzyme. The second cocktail contained three homology-directed repair (HDR) plasmids complementary to the three target sites with a selectable marker, puromycin (fig. 7.7). These, in theory, would cause a frame shift upon integration of the HDR cassette at the target site, resulting in a loss of function of the *cobl* gene.
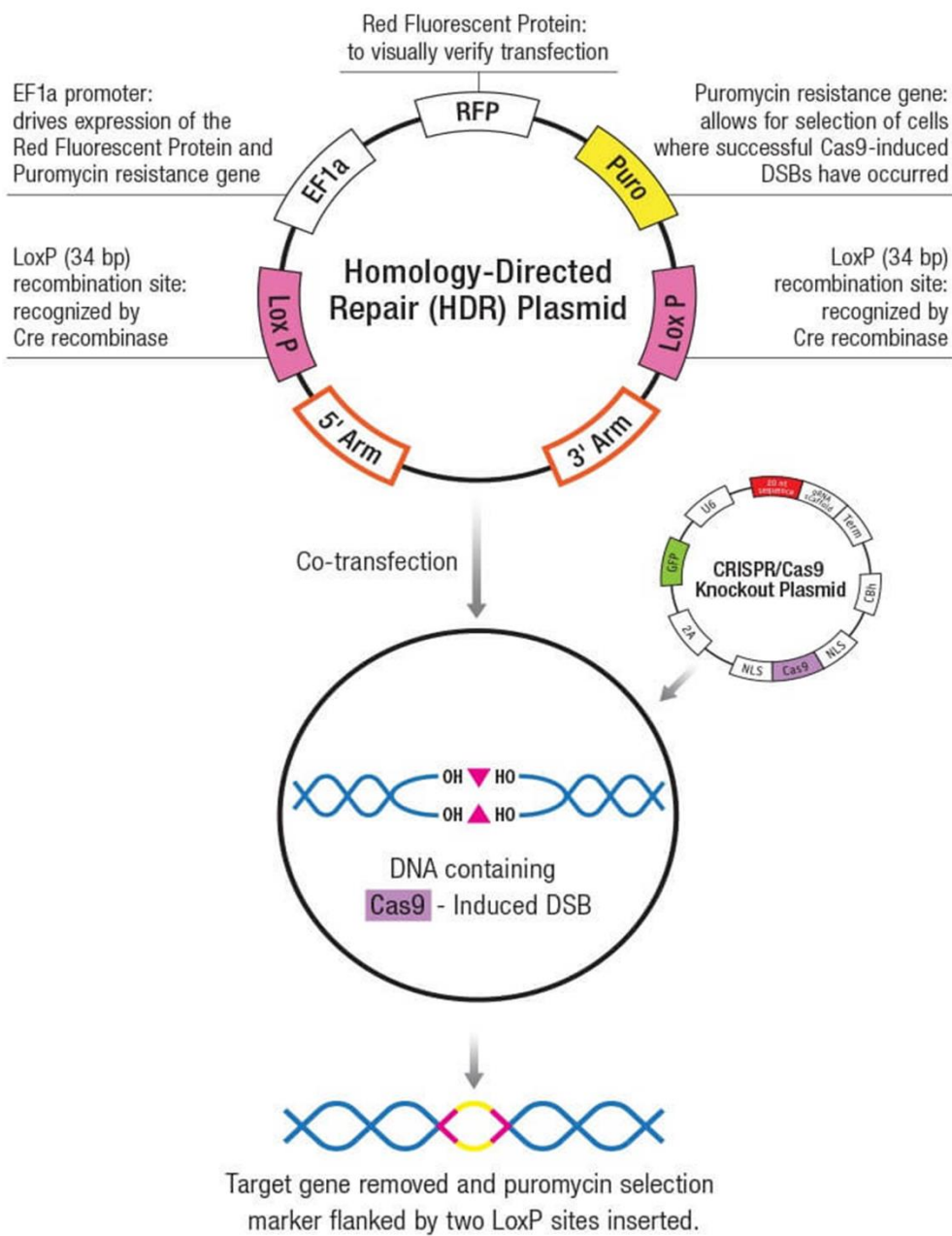
Figure 7.7. CRISPR/Cas9 COBL targeting strategy. *Top: map of CRISPR/Cas9 knockout and homology-directed repair plasmids used to generate COBL knockout cells with schematic of their mechanism of action shown. Three pairs of plasmids were contained within the cocktail, targeting the three independent target sites shown (bottom).*

Wildtype C2C12 cells were co-transfected with both cocktails. 24 hours later, growth media was replaced with growth media containing 4µg/ml puromycin for selection. Cells were then selected *en masse*, or through clonal selection, as outlined in methods. Cells were maintained at less than 60% confluency to minimise the loss of fusion competence caused by cells in contact with one another during expansion. To identify potential COBL knockout clones, PCR spanning each target site was performed, alongside PCR of α-actinin (Actn1) to control for DNA quality (fig. 7.8A). Integration of the HDR cassette at the target site would result in a lack of amplification due to the increased distance between the primers. Target site 3 was focussed on due to specificity and efficiency issues with primers targeting sites 1 and 2 (not shown). Absence of amplification in target site 3 was observed for clones 15, 18, 23, and 24, identifying them as having successful integration of the HDR cassette at target site 3. Interestingly, amplification was observed in cells selected en masse. Upon sequencing a loss of sequence quality was observed at the target site, likely representing a mixed population of cells, some with off-target integration of the HDR plasmid (fig. 7.8B).

SDS-PAGE and western blot detection was used to verify COBL knockout at protein level in the isolated clones. As expected, cells selected *en masse* display similar COBL expression levels to wildtype cells. In contrast, clones 15, 18, and 23 display a complete lack of COBL expression, confirming successful knockout of COBL through CRISPR/Cas9 targeting and HDR cassette integration in exon 4 (fig. 7.8C). Clone 24 was not examined as it was slow to re-establish following freezing. Crucially, COBL knockout revealed the relevant band representing COBL in western blots to be the band at ~170kDa, as no other band is affected by COBL knockout. Thus, full-length COBL does not migrate to its predicted molecular weight of ~144kDa, and the smaller bands detected in chapter 6 figure 6.3A are not COBL isoforms.
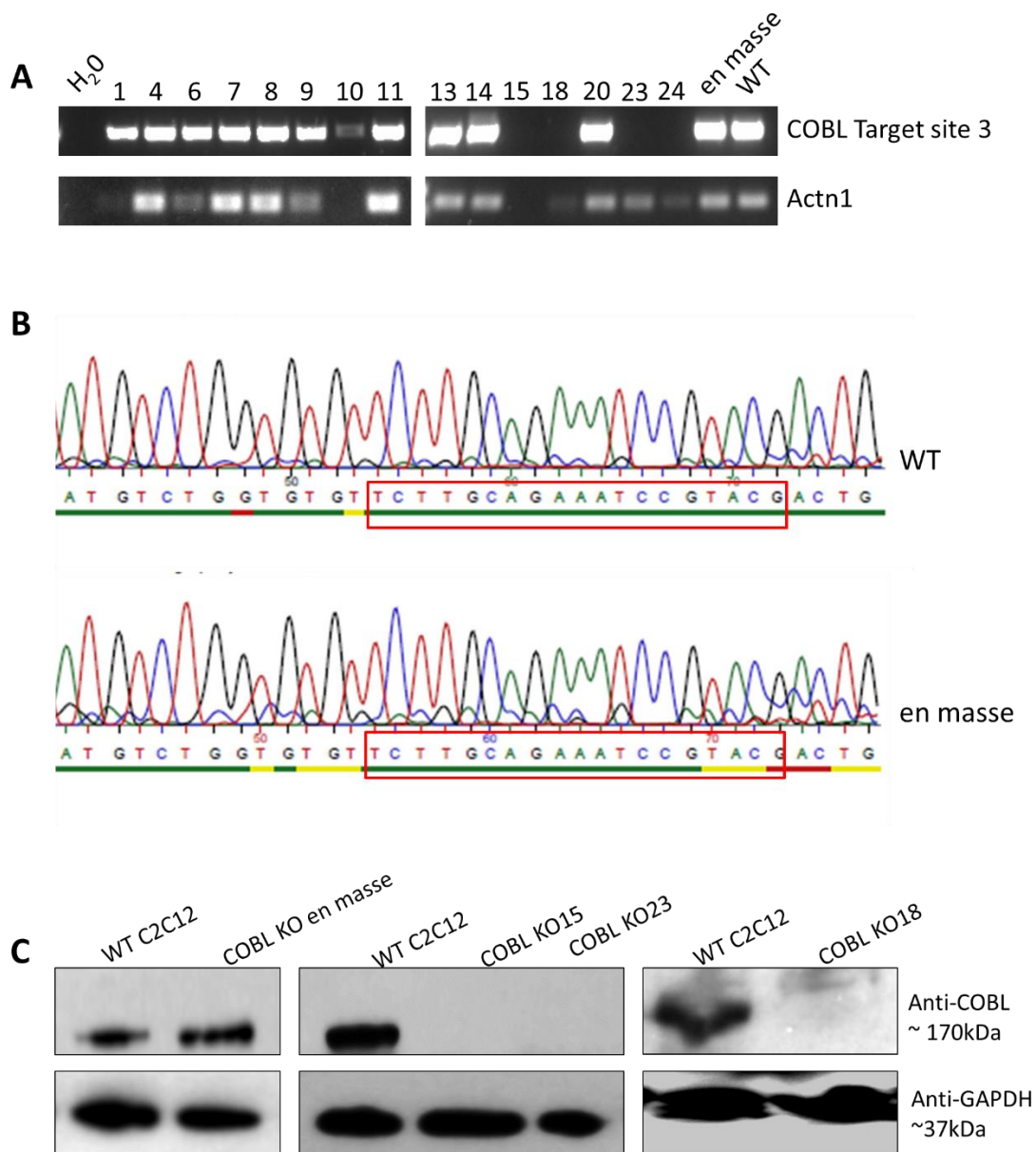
Figure 7.8. Generation of COBL knockout C2C12-derived cell lines. A) *PCR of DNA from wildtype C2C12 cells as well as COBL knockout clones and cells from an en masse selection following knockout. Primers for CRISPR/Cas9 target site 3 and Actn1, to confirm DNA integrity, were used. Primers for target site 1 and 2 were also trialled however these has lower specificity and efficiency so target site 3 was focussed on.* **B)** *Sequencing of target site 3 PCR product from wildtype and cells selected en masse (target site indicated by red box). Note the loss of sequence quality following the target site in the en masse selection cells.* **C)** *Western blot of wildtype C2C12 cells, COBL knockout cells selected en masse, and knockout clones 15, 18, and 23 at full confluency. Loss of COBL in clones 15, 18, and 23 is clearly shown.*

7.6 Characterisation of COBL Knockout Cells

Initial characterisation of the COBL knockout cell lines was performed on single proliferating cells to determine if absence of COBL influenced myoblast morphology. Wildtype C2C12 cells, and COBL knockout clones 15 and 23 (COBL KO15/23) were fixed and stained with crystal violet (fig. 7.9A). Clone 18 was not examined here as it had not yet re-established after freezing. Images were then taken, and ImageJ used to identify individual cells using the threshold tool. The analyse particles tool was then used to measure the area, circularity, and aspect ratio of the cells. Aspect ratio refers to the ratio of the major and minor axes of an ellipse fitted to a cell and is a measure of elongation.

Mean cell area was lower in both COBL knockout clones than in the wildtype. However, this effect was only statistically significant between wildtype cells and COBL KO15, with COBL KO23 cells significantly larger than COBL KO15 (fig. 7.9B). Significant differences in mean circularity and mean aspect ratio between wildtype and COBL knockout cells were also observed, but again these effects were not consistent between both COBL knockout cell lines (fig. 7.9C&D). Thus, the differences observed here at the single cell stage are most likely caused by an artefact of clonal selection, rather than knockout of COBL.

Next, attempts were made to differentiate the COBL knockout clones. Initial attempts failed due to the detachment of the COBL knockout clones during the differentiation process, usually observed shortly after replacing growth media with differentiation media, whereas wildtype cells mostly remained attached (fig.7.10A). To improve the adherence of the cells to the growth surface, 6-well plates were collagen-coated prior to seeding with wildtype and COBL knockout cells. This proved successful with cells remaining attached for at least 7 days in differentiation media. COBL knockout cells appeared to successfully align, but no obvious myotube formation was observed under brightfield microscopy, as was observed in wildtype cells (fig.7.10B).
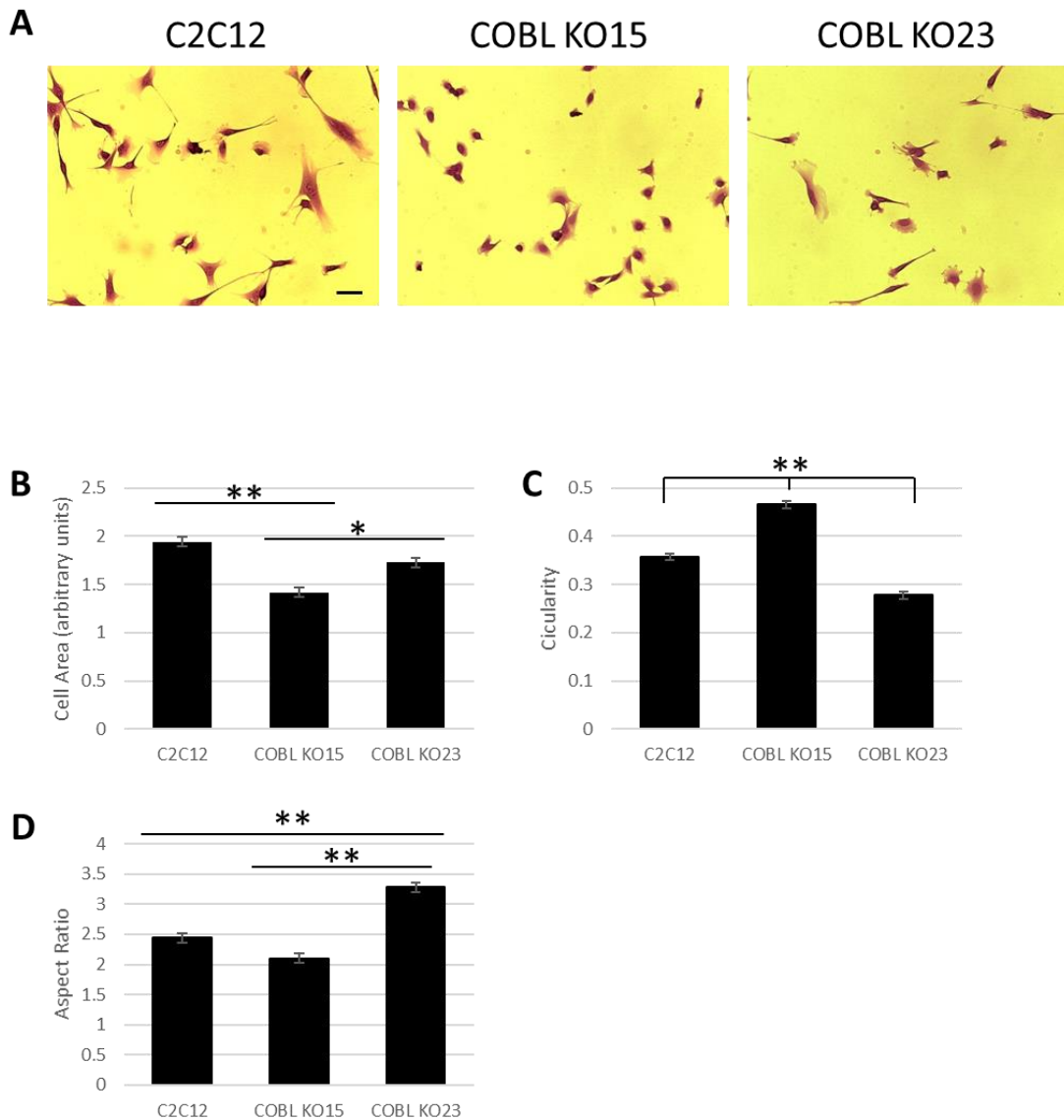
Figure 7.9. No consistent morphological changes are observed in COBL knockout clones. A) *Representative images of wildtype (C2C12), COBL knockout clone 15 (COBL KO15), and COBL knockout clone 23 (COBL KO23) stained with crystal violet. Scale bar represents 50 microns. **B-D)** Mean cell area, circularity, and aspect ratio measured through the ImageJ analyse particles tool. One way ANOVA revealed a significant effect of cell type on mean cell area [$F(6,630)=9.76$ $p<0.001$], circularity [$F(6,630)=78.21$ $p<0.001$], and aspect ratio [$F(6,630)=19.91$ $p<0.001$]. Tukey-HSD post-hoc analysis revealed significant differences as indicated (*$p<0.05$ **$p<0.01$).*

A

C2C12   COBL KO15   COBL KO23

D1 - Plastic

B

C2C12   COBL KO15   COBL KO23

D7– Plastic + collagen
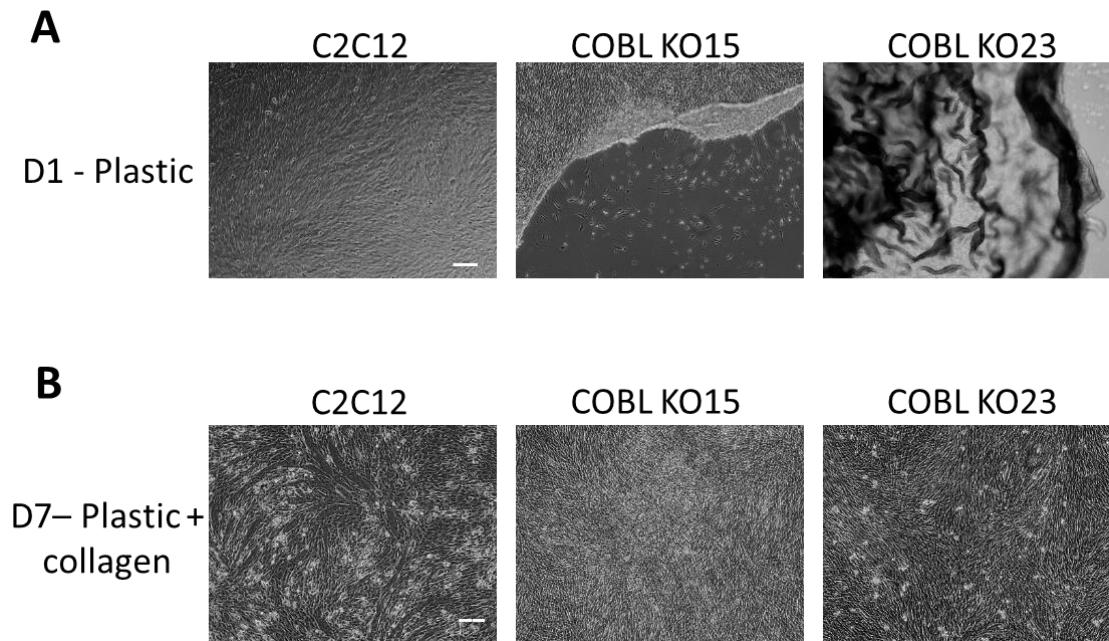
Figure 7.10. COBL knockout cells detach from the growth surface and show an apparent fusion defect. A) Representative brightfield images of wildtype (C2C12), and C2C12-derived COBL knockout clones 15 and 23 (COBL KO15/23) after 1 day in differentiation media (D1), grown on plastic 6-well plates. Detachment of the knockout clones was consistently observed. B) Representative brightfield images of wildtype (WT), and COBL knockout clones 15 and 23 (COBL KO15/23) after 7 days in differentiation media (D7), grown on collagen-coated plastic 6-well plates. Knockout clones remain attached to the growth surface but lack obvious fusion to form myotubes. Scale bars represent 100 microns.

To examine the apparent lack of fusion of COBL knockout cells, cells were grown on collagen coated wells in differentiation media for 7 days, and stained with EA53, against α-actinin. The aim of this experiment was to calculate fusion and differentiation indices of the knockout cells, as in chapter 3. COBL knockout clone 18 had been re-established for these experiments. Fusion was clearly observed in the wildtype C2C12 cells as expected. However, COBL knockout clones 15 and 18 showed very little α-actinin expression with only a few small myotubes forming, while COBL knockout clone 23 did fuse to some extent.

Unfortunately, differentiation indices could not be calculated for the COBL knockout clones. This was because of the extremely high density of nuclei observed in the images of these cells, making counting individual nuclei impossible (fig.7.11A). The high density of nuclei most likely represents cells continuing to proliferate, rather than following the differentiation pathway, after transfer to differentiation media. More evidence for differentiation defects comes from the aberrant expression of α-actinin observed in COBL knockout clone 23. Wildtype cells display striations of α-actinin, representing the formation of z-discs and the development of sarcomeres. This was not observed in COBL knockout clone 23, with α-actinin appearing to aggregate in a punctate pattern, rather than forming striations (fig.7.11A).

Fusion indices were calculated for wildtype cells and COBL knockout clone 23, expressed as the percentage of α-actin positive cells containing three or more nuclei (as in chapter 3 and (Li et al., 2017)) (fig.7.11B). The fusion index of COBL knockout clones 15 and 18 could not be calculated due to the lack of α-actinin expression. It was found that the fusion indices of wildtype cells and COBL KO23 were not significantly different. However, this measure does not consider the number of nuclei per frame, which appears higher for COBL KO23 but cannot be accurately measured due to the high density of the nuclei. It is therefore possible that more fusion events per nucleus are occurring in wildtype cells. As a proxy for this, the mean number of α-actinin positive cells with 3 or more nuclei per frame was calculated (fig.7.11C). This value was significantly higher in the wildtype cells. Therefore, assuming the COBL KO23 cells have more nuclei per frame, there are more fusion events occurring per nucleus in the wildtype cells.
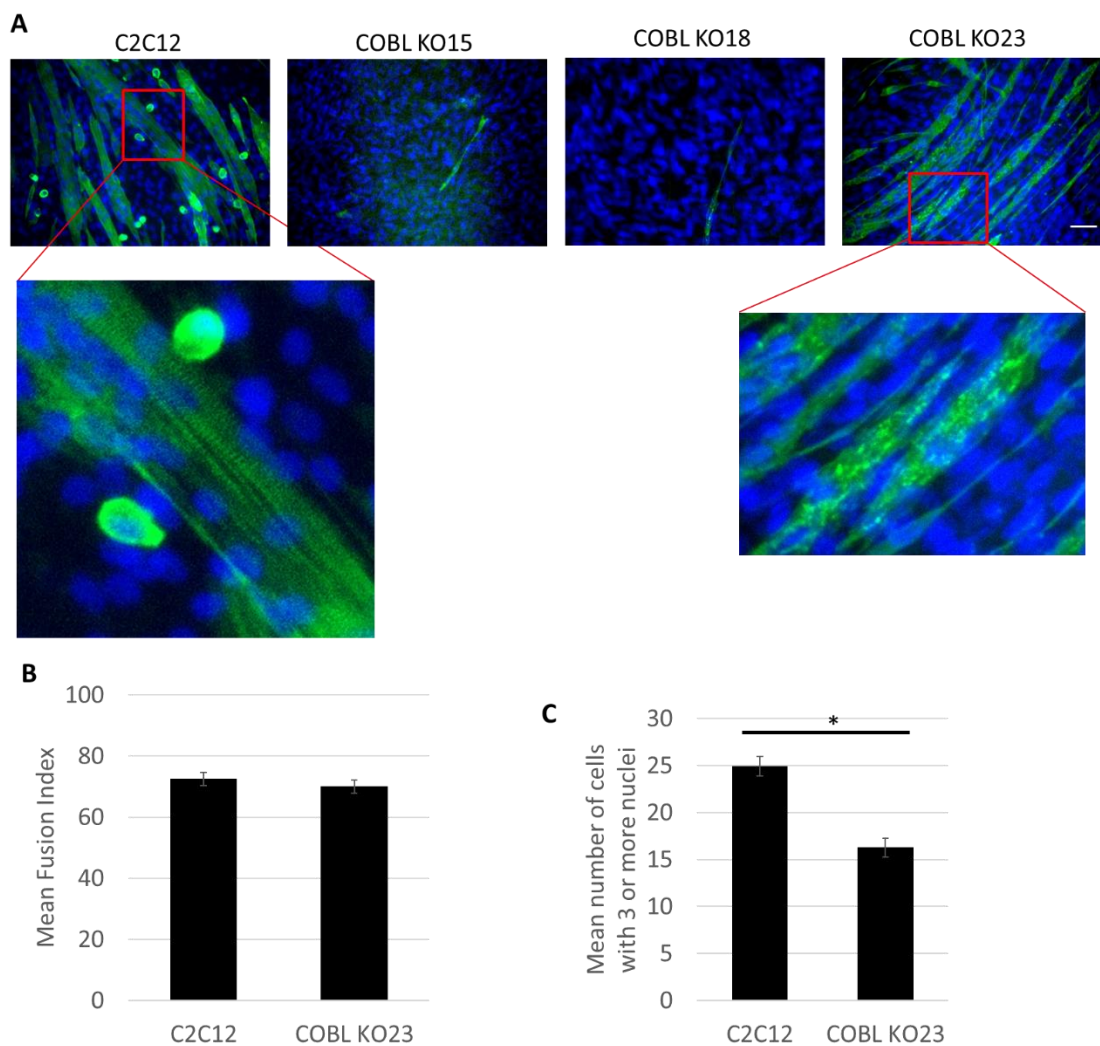
Figure 7.11. Myoblast fusion and differentiation are altered in C2C12-derived COBL knockout cells. A) *Representative widefield images of anti-α-actinin (green) and DAPI (blue) stained cells after 7 days in differentiation media, grown on collagen-coated 6-well plates. Two examples per cell line shown, cell lines shown are: wildtype C2C12 (C2C12), and COBL knockout clones 15 and 23 (COBL KO15/23). Zoomed in panels show α-actinin striations in the wildtype cells, and aberrant α-actinin aggregation in COBL knockout clone 23. Scale bar represents 75 microns.* **B)** *Mean fusion index per frame for wildtype and COBL knockout clone 23 (COBL KO15 could not be measured due to lack of α-actinin expression), expressed as the percentage of α-actin positive cells containing three or more nuclei. Students t-test revealed no significant difference (p=0.212, n>25).* **C)** *Mean number of α-actinin positive cells with 3 or more nuclei per frame. Students t-test revealed a wildtype cells had significantly higher values than COBL knockout clone 23 (*p<0.01, n>25).*

7.7 Conclusions

The expression of COBL at the protein level was found to be similar in both wildtype and IGFN1 knockout cells, with expression apparent when cells are fully confluent, and then throughout differentiation. This demonstrates that COBL is expressed when cells are ready to begin fusion and throughout the fusion process. The expression of COBL at the transcript level did differ between the cell types, with COBL mRNA levels higher than the wildtype at all time points and increasing throughout differentiation. Given the relatively similar protein levels, it is possible that IGFN1 acts to stabilise COBL and protect it from degradation. Therefore, in the absence of IGFN1 COBL transcription is upregulated to maintain COBL protein levels. Numerous IGFN1 isoforms are present throughout myoblast differentiation in vivo (Li et al., 2017), which may help to stabilise COBL at the right time and place to carry out its role.

Next, COBL overexpression in wildtype C2C12 cells was performed. COBL overexpression resulted in an increase in actin-rich protrusions in C2C12 cells, as has been reported in COS7 (Ahuja et al., 2007). Actin-driven protrusions are required for myoblast fusion (Shilagardi et al., 2013). While it cannot be assumed that these protrusions are directly involved in myoblast fusion in this case, it does provide evidence that COBL is able to alter the actin cytoskeleton of myoblast cells.

When COBL overexpressing cells were differentiated more nuclei per cell were observed than in cells expressing the tdTomato control. This result directly implicates COBL in myoblast fusion. This however may be driven by several cells overexpressing COBL with extremely high nuclei counts. The median number of nuclei between the two conditions was relatively similar, whereas the mean values were significantly different. COBL is known to remodel actin in different ways depending on its concentration (Husson et al., 2011). It may be that COBL expression must reach a specific concentration to drive myoblast fusion, something which is difficult to control using basic transfections to induce overexpression. This concentration may have been reached in some COBL overexpressing cells and not others. It should also be

noted that the more fusion events that occur, the more likely one of the nuclei fusing to the myotube is expressing the transfected construct. Therefore, it is more likely that myotubes with more nuclei express the transfected construct, potentially confounding these results. However, this is the case for both constructs.

COBL knockout was used to reveal whether COBL was required for myoblast fusion. CRISPR/Cas9 targeting successfully produced COBL knockout clones. It would have been preferable to use *en masse* selection, to reduce the likelihood of artefacts from clonal selection, but cells selected *en masse* still expressed COBL. However, consistency between clones can also indicate whether an observed phenotype is caused by the loss of COBL. Rescue experiments should be performed in the future to validate the observed phenotypes. It should also be noted that an ideal experimental setup would include a non-targeted control cell line which also underwent clonal selection to allow decoupling of any fusion phenotype observed from the potential effects of clonal selection. Due to time constraints this was not possible but should be addressed in future experiments.

Proliferating COBL knockout myoblasts did not display any consistent morphological changes, with the differences observed likely an artefact of clonal selection. This was expected as COBL expression is not observed at the protein level until confluency is reached in wildtype cells. However, on reaching confluency, where COBL is expressed in wildtype cells, the knockout clones tended to detach from the growth surface. Further, when collagen coating was used to maintain attachment through differentiation, COBL knockout clones did not appear to fuse when examined through brightfield microscopy.

α-actinin staining revealed a lack of fusion in two of the COBL knockout clones, with apparently reduced fusion in another. On top of this, when fusion did occur in COBL knockout clone 23, aberrant α-actinin expression was observed, reflecting an inability of these cells to develop z-discs after 7 days in differentiation media. These findings further implicate COBL in myoblast fusion

and differentiation to some extent. However, because fusion did occur in clone 23, it is clear that COBL is not essential for myoblast fusion. Further work including rescue of wildtype phenotypes in the knockout cell lines, through COBL expression, is required before definitive conclusions can be drawn.

It is noteworthy that the COBL knockout mouse is viable and does not display any overt skeletal muscle phenotype (Haag et al., 2018). However, in depth analysis has not been reported, with no muscle histology shown in the paper characterising the COBL knockout phenotype. Examples of mutations resulting in a myoblast fusion defect *in vitro* which still allow survival *in vivo* have been reported (Schwander et al., 2003). Muscle phenotypes were revealed using histological and ultrastructural analysis. It is likely that the ECM and other structures *in vivo* help to facilitate myoblast fusion where it is disrupted *in vitro*. More stringent examination of the COBL knockout mouse is required to reveal potential defects in their skeletal muscle.

This chapter has outlined the expression pattern of COBL throughout myoblast fusion and differentiation. Phenotypes associated with COBL overexpression were characterised and correlate with COBL being involved in myoblast fusion. Finally, COBL knockout cell lines were developed. Characterisation of these cell lines provided further evidence that COBL is involved in myoblast fusion and differentiation, but these findings should be treated cautiously until more work is completed.

CHAPTER 8:

DISCUSSION AND

FUTURE WORK

Chapter 8: Discussion and Future Work

8.1 Overview

The aim of the research presented in this thesis was to gain insights into the functional role of IGFN1 in skeletal muscle, primarily through the characterisation of a C2C12-derived IGFN1 knockout cell line, and the identification and validation of IGFN1 interaction partners. The hypotheses outlined at the outset of this thesis were as follows:

- Because of its domain composition and localisation, **IGFN1 is a structural protein.**

- **IGFN1 is a scaffold for signalling/effector proteins**, due to its globular domains, its multiple interaction partners, and its lack of catalytic activity.

- **IGFN1 is a mechanosensor**. Unfolding of proteins with similar globular domain compositions has implicated them in mechanotransduction. The interaction with KY and the CASA pathway may provide a mechanism for this.

- Fusion defects in IGFN1 knockdown C2C12 cells suggest **IGFN1 is part of the myoblast fusion machinery.**

- The association between atrophic signalling and IGFN1 expression suggests **IGFN1 is a facilitator of atrophy.**

A direct role for IGFN1 in atrophy could not be determined, however, this may have been a result of the model used. Evidence of IGFN1 performing a role in myoblast fusion through cytoskeletal remodelling was revealed, with IGFN1 potentially acting through the actin nucleator COBL. Finally, progress was made in producing recombinant IGFN1 for biophysical analysis, providing a tool for examining any role for IGFN1 in maintaining sarcomeric structural integrity or in mechanotransduction.

8.2 Discussion

Until recently, many large immunoglobulin and fibronectin domain containing proteins had simply been considered to have structural roles, maintaining the integrity of the sarcomere through contraction and relaxation cycles. However, it is now known that many of these proteins are involved in processes ranging from mechanotransduction to determining sarcomeric length. A similar pattern has emerged here with IGFN1. Based on the domain composition of IGFN1 it would appear that its function is merely structural. However, several potential roles in skeletal muscle have been uncovered for IGFN1 beyond z-disc structural integrity, with the main hypotheses outlined above.

One of the main hypotheses regarding the function of IGFN1 at the outset of this work was that it plays a role in atrophy. Here it was shown that IGFN1 is not able to induce atrophy directly *in vitro*, in concurrence with the lack of atrophy from IGFN1 overexpression *in vivo* (Li et al., 2017). Its upregulation during atrophic processes may be a compensatory mechanism, to protect the structure of the sarcomere even during atrophy. Or, IGFN1 may indirectly facilitate atrophy by providing a scaffold for other proteins to perform their roles at the z-disc, or by blocking the activity of its interaction partners, of which the translational elongation factor eEF1a is an example (Mansilla et al., 2008). Given that several proteasome subunits were identified as potential interaction partners through pull-downs and LS-MS/MS analysis, IGFN1 may also aid in bringing the proteasome subunits to the z-disc and facilitate protein degradation.

Alongside this, IGFN1 interacts with key components of the CASA machinery KY and FLNC. IGFN1 may contribute to the breakdown of damaged proteins through this pathway, but CASA has been demonstrated to be required for muscle mass maintenance (Arndt et al., 2010). Meaning if IGFN1 does play a role in CASA its upregulation during atrophy is likely compensatory, ensuring turnover of damaged proteins at the z-disc. Despite the attempts here it is still unclear whether IGFN1 is a factor in maintaining the balance of muscle mass maintenance and, if it is, which end of the scale it fits on.

Away from atrophy, the most significant finding of the work presented here is of a role for IGFN1 in myoblast fusion and differentiation. Many proteins have been implicated in myoblast fusion in vitro, but the effects of clonal selection often confound these results. Rescue of the phenotypes here, however, clearly demonstrates that IGFN1 is involved in myoblast fusion. As expected, IGFN1 was not demonstrated to be able to induce fusion directly as with the fusogens myomaker and myomerger so its contribution to fusion was likely to be indirect, acting through interacting partners.

Further investigation of the role of IGFN1 in myoblast fusion revealed that it may act asymmetrically, with wildtype and IGFN1 knockout cells able to fuse with one another. This asymmetry is observed with several proteins associated with myoblast fusion, notably myomaker (Millay et al., 2013). Contributing to the idea that mammalian myoblast fusion follows a Drosophila-like model, with a founder cell and a fusion competent myoblast expressing different components of the fusion machinery.

A connected phenotype identified in IGFN1 knockout cells, that was rescuable through IGFN1_V1 expression, was decreased actin polymerisation. It is known that actin dynamics play a crucial role in all stages of myoblast fusion and IGFN1 is known to interact with actin (Baker et al., 2010). The Arp2/3 complex is the main driver of actin nucleation and polymerisation during myoblast fusion, regulated by N-WASP and Rac1 (Berger et al., 2008; Gildor et al., 2009; Richardson et al., 2007). It was therefore surprising that neither Arp2/3 or any of its upstream regulators were identified as interacting partners of IGFN1. It was, however, demonstrated that IGFN1 interacted with the actin nucleator COBL and that COBL localised to the z-disc in vivo.

COBL was subsequently demonstrated to be capable of inducing changes to the actin cytoskeleton in myoblasts, and even increase myoblast fusion when overexpressed. These results raise the possibility that COBL acts as an actin nucleator during myoblast fusion and differentiation, a previously unidentified role. This would also mean that Arp2/3 is not the sole actin nucleator responsible for myoblast fusion. It is possible that IGFN1 acts as a scaffold to

bring together a complex of proteins including COBL during myoblast fusion that is entirely separate from the Arp2/3 complex and is regulated by other upstream factors. It is evident that there is much more research to be done before this conclusion can be drawn, but it remains a possibility.

The research presented here demonstrates IGFN1, and potentially COBL, are involved in myoblast fusion *in vitro.* More widely, *in vivo*, this implicates IGFN1 in either muscle tissue development; or in adult skeletal muscle during the repair of damaged muscle tissue, and in hypertrophy and hyperplasia. In adult skeletal muscle this would mean IGFN1 contributing to the fusion of satellite cells to existing muscle fibres. The robust expression of IGFN1 in adult skeletal muscle does suggest that it plays a role beyond a developmental one. This role may be unrelated to fusion of satellite cells and may be connected to atrophy, or simply maintaining the structure of the z-disc. However, the possibility that IGFN1 is a factor in the fusion of satellite cells to the adult muscle fibre cannot yet be ruled out. *In vivo* studies would be invaluable here, examining the effect of IGFN1 knockout on the repair of damaged muscle tissue.

It is now clear that IGFN1 is involved in a number of processes in the muscle fibre and that more work is required to fully uncover and understand its importance, especially *in vivo.*

8.3 Future Work
8.3.1 *In Vitro* Models
To validate the fusion phenotypes observed in C2C12-derived COBL knockout clones, the phenotype should be rescued through stable expression of COBL. This will result in a return to the wildtype fusion phenotype if COBL deficiency, rather than clonal selection, is indeed causing the fusion defects. Failing this, *en masse* selection of CRISPR/Cas9 targeted cells could be trialled again to remove the confounding effects of clonal selection. It is crucial to validate this phenotype *in vitro* as this may justify *in vivo* experiments investigating the role of COBL in skeletal muscle (as will be discussed below).

One of the most insightful techniques that should be employed in future work examining the role of IGFN1 and COBL in myoblast fusion is live cell imaging. This could not be performed during this project due to equipment and cost limitations. Live cell imaging of both the IGFN1 and COBL knockout myoblast lines and wildtype cells expressing fluorescently tagged IGFN1 and/or COBL could be used to examine different aspects of myoblast fusion. Imaging of the knockout cells would allow the identification of the differences between knockout and wildtype cells during fusion, revealing the precise changes to the morphology of the cell that either protein is responsible for. Live imaging of the actin cytoskeleton in these knockout cells would prove particularly informative. Live Imaging of wildtype cells expressing fluorescently tagged proteins would allow the proteins to be tracked in real-time through fusion both independently and together. This would provide information as to where and when in the process the proteins are required. A proximity ligation assay could also be used to track the interaction through fusion and differentiation. However, this method would require fixation of the cells and not provide real-time information.

To investigate the hypothesis that IGFN1 stabilises COBL, outlined in chapter 7, tracking of COBL protein levels in the presence and absence of IGFN1 should be performed. This experiment would involve co-transfection of a cell type that does not endogenously express either COBL of IGFN1, such as COS7. Cells would be transfected with either; a vector conferring IGFN1(+a tag such as V5) expression, and a vector conferring the expression of COBL in an inducible manner (such as the Tetracycline Off system (Gossen and Bujard, 1992)), or a vector conferring expression of the V5 tag as a control, and a vector conferring the expression of COBL in an inducible manner. After 24hours COBL expression could be inhibited pharmacologically and the protein level of COBL traced through SDS-PAGE western blot analysis. COBL protein levels should be expressed as a proportion of those observed at t=0 to account for different COBL expression levels between samples. If IGFN1 does stabilise COBL and prevent its degradation, COBL protein levels would fall less quickly in the IGFN1 and COBL transfected samples than in the control

samples. Transfections followed by cycloheximide treatment could also be used, however this would rely on IGFN1 remaining stable throughout.

Finally, to further examine the potential role of IGFN1 in atrophy, similar experiments as performed in chapter 4 should be repeated with recombinant myostatin, rather than dexamethasone. Dexamethasone was used to indirectly induce myostatin expression and atrophy (Menconi et al., 2008; Qin et al., 2013). However, dexamethasone has other off target effects and induces different effects based on the differentiation state of the cell (Guerriero and Florini, 1980; Han et al., 2017; Qin et al., 2010), something which may have confounded results in the IGFN1 knockout cell line in which a differentiation defect is observed. The use of recombinant myostatin, while more costly than dexamethasone, may provide a clearer picture as to whether IGFN1 contributes to, and is upregulated in response to, myostatin signalling-induced atrophy *in vitro.*

8.3.2 *In Vivo* Experiments

Previous attempts at determining the effects of loss of IGFN1 function *in vivo* have involved electroporation of adult mice with the same CRISPR/Cas9 constructs used to produce the IGFN1 knockout cell lines used in this work. These electroporations were performed with the goal of examining the role of IGFN1 in atrophy and not myoblast fusion and differentiation (Li et al., 2017). To examine the role of IGFN1 in myoblast fusion and differentiation *in vivo* an IGFN1 knockout mouse line should be generated. It should be noted that the generation of such a mouse line was attempted through an external company. Unfortunately, this work failed and there was a lack of time and budget for another attempt within this project.

The Knockout Mouse Project (KOMP, The Jackson Laboratory) have reported the development of an IGFN1 knockout mouse. Phenotyping of this animal has been limited and did not include any skeletal muscle analysis. The prohibitive cost and time-scale of re-deriving and importing this line meant that this mouse could not be examined within this project. Additionally, the

genotyping of this mouse is not clear, and no western blots were performed. Owing to the complexity of the IGFN1 locus, and the isoforms produced from it, it is possible that this mouse is not a genuine knockout.

The generation, or import following validation, of an IGFN1 knockout mouse line would allow it to be determined whether the fusion and differentiation phenotypes observed *in vitro* are relevant *in vivo.* However, other tissues and structures such as the ECM could aid myoblast fusion in the absence of IGFN1 and result in the formation of muscle which displays other pathologies. In this case analysis should focus on myofiber size and structure, especially at the z-disc, where electron microscopy could reveal z-disc phenotypes if IGFN1 is playing a role in maintaining its structure. In addition to this, the expression of COBL in the muscles of IGFN1 knockout mice should be examined; both on a whole tissue level, through qPCR and western blotting, and in terms of its localisation through immunostaining. It would be expected that COBL would not localise to the z-disc in IGFN1 knockout mice if IGFN1 does act as a scaffold for COBL.

To confirm any role for COBL in skeletal muscle *in vivo* the knockout mouse line generated by Haag *et al* (Haag et al., 2018) should be extensively examined for muscle pathology. While the animals are viable and display no overt muscle phenotypes, there may be some pathology. Often mice with muscle pathologies are overtly unaffected without muscular challenge, or appear even stronger, as is the case with the mdx mouse (Stedman et al., 1991). If COBL KO mice are subjected to a protocol whereby mechanical tension is placed upon the muscle, any underlying pathology may be exacerbated, revealing muscular defects. Even without mechanical tension, histology and electron microscopy may reveal phenotypes associated with COBL loss of function. It is important for this work to be completed as *in vitro* evidence alone is not sufficient to conclusively demonstrate a role for COBL in skeletal muscle.

IGFN1 and COBL may play a role in repairing muscle damage *in vivo,* contributing the fusion of satellite cells to the damaged myofibres to regenerate

the tissue. Upregulation of either protein in response to muscular injury would provide evidence for this and could be examined in the future. Following this, the injury response of the COBL knockout mice and IGFN1 knockout mice, if generated, should be compared to the response in wildtype mice.

8.3.3 Biophysical and Biochemical Experiments

As stated above, the AFM unfolding experiments could not be repeated and refined within the timeframe of this project. Future work should therefore focus on optimising conditions to allow for the collection of high-quality mechanical unfolding/refolding data for the purified IGFN1 fragments. Fresh recombinant His-tagged protein should be purified to ensure that the samples are intact and fully folded prior to surface immobilisation on Ni-NTA-coated glass coverslips for the AFM experiments. In addition, other IGFN1 fragments should be cloned into the pQE2-Im9 vector and purified to allow for a complete characterisation of all the predicted domains inIGFN1.

Further examination of the potential interactions, identified through LC-MS/MS analysis of pull-downs, between IGFN1 and several proteasome subunits should be performed. The association of IGFN1 expression with atrophic signalling raises the possibility that these interactions may be functionally relevant. A similar experimental design to that used to validate the IGFN1-COBL interaction should be used, with immunoprecipitation and colocalization experiments employed. It should be noted that initial analysis of these interactions was performed by another student in our lab, yielding negative results. However, this work relied on the immunoprecipitation of endogenous proteasome subunits, and their identification using antibodies which proved unreliable. More work is required to conclusively prove or disprove these potential interactions.

8.4 Overall Conclusions

This thesis has described the characterisation of a C2C12-derived IGFN1 knockout cell line, revealing a role for IGFN1 in myoblast fusion and differentiation, associated with the remodelling of the actin cytoskeleton. Pull-down analysis revealed the actin nucleator COBL as a potential interacting partner of IGFN1, and this interaction was subsequently validated. The role of COBL in myoblast fusion was investigated through overexpression experiments and the generation of a C2C12-derived knockout cell line. Initial characterisation points towards a role for COBL in myoblast fusion, with more work required to confirm this. It is possible that IGFN1 influences actin remodelling, and therefore myoblast fusion, through its interaction with COBL.

Glossary of Abbreviations

Abbreviation	Name
ActRII	Activin type II receptor
AFM	Atomic Force Microscopy
AKT	Protein Kinase B
Arp2/3	Actin-Related Protein 2/3
ATCN1	Alpha Actin
BAG3	Bcl2 Associated Athanogen 3
BAI1/3	Brain-Specific Angiogenesis Inhibitor 1 /3
BDL	Bile Duct Ligation
BSA	Bovine serum albumin
CASA	Chaperone Assisted Selective Autophagy
COBL	Cordon-Bleu WH2 Repeat Protein
COS7	CV-1 in Origin, carrying the SV40 genetic material
CRISPR	Clustered regularly interspaced short palindromic repeats
CTCF	Corrected total cell fluorescence
DAPI	4′,6-diamidino-2-phenylindole
DM	Differentiation Media
DMD	Duchenne muscular dystrophy
DOCK1	Dedicator of Cytokinesis 1
DUF	Dumbfounded
ECM	Extracellular matrix
EDL	Extensor digitorum
EF-Tu	Elongation Factor Tu
eIF4E	Eukaryotic Translation Initiation Factor 4E
ERK	Extracellular Signal-regulated Kinase
FBS	Foetal bovine serum
FC	Founder Cell
FCM	Fusion Competent Myoblast
FLNC	Filamin C
FOXO	Forkhead Box Transcription Factors
GEF	Guanine nucleotide exchange factors
GH	Growth Hormone
GM	Growth Media
HBS	Hibris
HPRT	Hypoxanthine-guanine phosphoribosyltransferase
IGF1	Insulin-like growth factor 1
IGF-1R	Insulin-like growth factor 1 Receptor
IGFN1	Immunoglobulin-like and fibronectin type III domain containing 1
IgSF	Immunoglobulin superfamily
IRS-1	Insulin Receptor Substrate 1

KY	Kyphoscoliosis peptidase
LC-MS/MS	Liquid Chromatography with tandem mass spectrometry
MAPK	mitogen-activated protein kinase
MBC	Myoblast City
mTOR	Mammalian Target of Rapamycin
MURF1	Muscle Ring Finger1
MYOD	Myogenic Differentiation
NAP1	Nucleosome Assembly Protein 1
Ni-NTA	Nickel-nitrilotriacetic acid
OD	Optical density
p70s6k	Ribosomal protein s6 kinase beta 1
PAGE	Polyacrylamide gel electrophoresis
PBS	Phosphate-buffered saline
PCR	Polymerase Chain Reaction
PI3K	Phosphatidylinositol 3 kinase
qPCR	Quantitative Polymerase Chain Reaction
RAC1	Rac Family Small GTPase 1
RHEB	Ras Homolog Enriched in Brain
RIPA	Radioimmunoprecipitation assay
RST	Roughest
SCAR	Suppressor of cAR
SDS	Sodium dodecyl sulphate
Smad2/3	SMAD Family Member 2/3
SNS	Sticks and Stones
TA	Tibialis anterior
TAZ	Tafazzin
TCS2	Tuberous sclerosis complex 2
TNFα	Tumour Necrosis Factor α
WASP	Wiskott-Aldrich syndrome protein
WAVE	WASP family Verprolin-homologous protein
XIN	Xin Actin Binding Repeat Containing 1
Y2H	Yeast 2 Hybrid
YAP	Yes Associated Protein
ZAK	Leucine Zipper-and Sterile Alpha Motif-Containing Kinase

References

Ahuja, R., R. Pinyol, N. Reichenbach, L. Custer, J. Klingensmith, M. M. Kessels, and B. Qualmann, 2007, Cordon-bleu is an actin nucleation factor and controls neuronal morphology: Cell, v. 131, p. 337-50.

Anantharaman, V., E. V. Koonin, and L. Aravind, 2001, Peptide-N-glycanases and DNA repair proteins, Xp-C/Rad4, are, respectively, active and inactivated enzymes sharing a common transglutaminase fold: Hum Mol Genet, v. 10, p. 1627-30.

Arndt, V., N. Dick, R. Tawo, M. Dreiseidler, D. Wenzel, M. Hesse, D. O. Furst, P. Saftig, R. Saint, B. K. Fleischmann, M. Hoch, and J. Hohfeld, 2010, Chaperone-assisted selective autophagy is essential for muscle maintenance: Curr Biol, v. 20, p. 143-8.

Artero, R. D., I. Castanon, and M. K. Baylies, 2001, The immunoglobulin-like protein Hibris functions as a dose-dependent regulator of myoblast fusion and is differentially controlled by Ras and Notch signaling: Development, v. 128, p. 4251-64.

Atkinson, R. A., C. Joseph, G. Kelly, F. W. Muskett, T. A. Frenkiel, D. Nietlispach, and A. Pastore, 2001, Ca2+-independent binding of an EF-hand domain to a novel motif in the alpha-actinin-titin complex: Nat Struct Biol, v. 8, p. 853-7.

Baker, J., G. Riley, M. R. Romero, A. R. Haynes, H. Hilton, M. Simon, J. Hancock, H. Tateossian, V. M. Ripoll, and G. Blanco, 2010, Identification of a Z-band associated protein complex involving KY, FLNC and IGFN1: Exp Cell Res, v. 316, p. 1856-70.

Banes, A. J., J. Gilbert, D. Taylor, and O. Monbureau, 1985, A new vacuum-operated stress-providing instrument that applies static or variable duration cyclic tension or compression to cells in vitro: J Cell Sci, v. 75, p. 35-42.

Baneyx, F., and M. Mujacic, 2004, Recombinant protein folding and misfolding in Escherichia coli: Nature Biotechnology, v. 22, p. 1399-408.

Bang, M. L., X. Li, R. Littlefield, S. Bremner, A. Thor, K. U. Knowlton, R. L. Lieber, and J. Chen, 2006, Nebulin-deficient mice exhibit shorter thin filament lengths and reduced contractile function in skeletal muscle, J Cell Biol, v. 173, p. 905-16.

Baulieu, E.-E. K., Paul A., 1990, Hormones - From molecules to disease, Springer Netherlands.

Beatham, J., K. Gehmlich, P. F. van der Ven, J. Sarparanta, D. Williams, P. Underhill, C. Geier, D. O. Furst, B. Udd, and G. Blanco, 2006, Constitutive upregulations of titin-based signalling proteins in KY deficient muscles: Neuromuscul Disord, v. 16, p. 437-45.

Beatham, J., R. Romero, S. K. Townsend, T. Hacker, P. F. van der Ven, and G. Blanco, 2004a, Filamin C interacts with the muscular dystrophy KY protein and is abnormally distributed in mouse KY deficient muscle fibres: Hum Mol Genet, v. 13, p. 2863-74.

Beatham, J., R. Romero, S. K. M. Townsend, T. Hacker, P. F. M. v. d. Ven, and G. Blanco, 2004b, Filamin C interacts with the muscular dystrophy

KY protein and is abnormally distributed in mouse KY deficient muscle fibres: Human Molecular Genetics, v. 18, p. 4731-4740.

Berger, S., G. Schafer, D. A. Kesper, A. Holz, T. Eriksson, R. H. Palmer, L. Beck, C. Klambt, R. Renkawitz-Pohl, and S. F. Onel, 2008, WASP and SCAR have distinct roles in activating the Arp2/3 complex during myoblast fusion: J Cell Sci, v. 121, p. 1303-13.

Bi, P., A. Ramirez-Martinez, H. Li, J. Cannavino, J. R. McAnally, J. M. Shelton, E. Sanchez-Ortiz, R. Bassel-Duby, and E. N. Olson, 2017, Control of muscle formation by the fusogenic micropeptide myomixer: Science, v. 356, p. 323-327.

Blanco, G., G. R. Coulton, A. Biggin, C. Grainge, J. Moss, M. Barrett, A. Berquin, G. Marechal, M. Skynner, P. van Mier, A. Nikitopoulou, M. Kraus, C. P. Ponting, R. M. Mason, and S. D. Brown, 2001, The kyphoscoliosis (ky) mouse is deficient in hypertrophic responses and is caused by a mutation in a novel muscle-specific protein: Hum Mol Genet, v. 10, p. 9-16.

Blanco, G., C. Pritchard, P. Underhill, S. Breeds, K. M. Townsend, A. Greenfield, and S. D. Brown, 2004, Molecular phenotyping of the mouse ky mutant reveals UCP1 upregulation at the neuromuscular junctions of dystrophic soleus muscle: Neuromuscul Disord, v. 14, p. 217-28.

Blau, H. M., C. P. Chiu, and C. Webster, 1983, Cytoplasmic activation of human nuclear genes in stable heterocaryons: Cell, v. 32, p. 1171-80.

Boateng, S. Y., S. E. Senyo, L. Qi, P. H. Goldspink, and B. Russell, 2009, Myocyte remodeling in response to hypertrophic stimuli requires nucleocytoplasmic shuttling of muscle LIM protein: J Mol Cell Cardiol, v. 47, p. 426-35.

Bodine, S. C., E. Latres, S. Baumhueter, V. K. Lai, L. Nunez, B. A. Clarke, W. T. Poueymirou, F. J. Panaro, E. Na, K. Dharmarajan, Z. Q. Pan, D. M. Valenzuela, T. M. DeChiara, T. N. Stitt, G. D. Yancopoulos, and D. J. Glass, 2001, Identification of ubiquitin ligases required for skeletal muscle atrophy: Science, v. 294, p. 1704-8.

Boppart, M. D., M. F. Hirshman, K. Sakamoto, R. A. Fielding, and L. J. Goodyear, 2001, Static stretch increases c-Jun NH2-terminal kinase activity and p38 phosphorylation in rat skeletal muscle: Am J Physiol Cell Physiol, v. 280, p. C352-8.

Bour, B. A., M. Chakravarti, J. M. West, and S. M. Abmayr, 2000, Drosophila SNS, a member of the immunoglobulin superfamily that is essential for myoblast fusion: Genes Dev, v. 14, p. 1498-511.

Bourdel-Marchasson, I., A. Diallo, C. Bellera, C. Blanc-Bisson, J. Durrieu, C. Germain, S. Mathoulin-Pelissier, P. Soubeyran, M. Rainfray, M. Fonck, and A. Doussau, 2016, One-Year Mortality in Older Patients with Cancer: Development and External Validation of an MNA-Based Prognostic Score: PLoS One, v. 11, p. e0148523.

Bradford, M. M., 1976, A Rapid and Sensitive Method for the Quantification of Microgram Quantities of Protein Utilizing the Principle of Protein-Dye Binding: Analytical Biochemistry, v. 72.

Bridges, L. R., G. R. Coulton, G. Howard, J. Moss, and R. M. Mason, 1992, The neuromuscular basis of hereditary kyphoscoliosis in the mouse: Muscle Nerve, v. 15, p. 172-9.

Burnett, P. E., R. K. Barrow, N. A. Cohen, S. H. Snyder, and D. M. Sabatini, 1998, RAFT1 phosphorylation of the translational regulators p70 S6 kinase and 4E-BP1: Proc Natl Acad Sci U S A, v. 95, p. 1432-7.

Cai, D., J. D. Frantz, N. E. Tawa, Jr., P. A. Melendez, B. C. Oh, H. G. Lidov, P. O. Hasselgren, W. R. Frontera, J. Lee, D. J. Glass, and S. E. Shoelson, 2004, IKKbeta/NF-kappaB activation causes severe muscle wasting in mice: Cell, v. 119, p. 285-98.

Capani, F., T. J. Deerinck, M. H. Ellisman, E. Bushong, M. Bobik, and M. E. Martone, 2001, Phalloidin-eosin followed by photo-oxidation: a novel method for localizing F-actin at the light and electron microscopic levels: J Histochem Cytochem, v. 49, p. 1351-61.

Carlson, C. J., Z. Fan, S. E. Gordon, and F. W. Booth, 2001, Time course of the MAPK and PI3-kinase response within 24 h of skeletal muscle overload: J Appl Physiol (1985), v. 91, p. 2079-87.

Carroll, E. A., D. Gerrelli, S. Gasca, E. Berg, D. R. Beier, A. J. Copp, and J. Klingensmith, 2003, Cordon-bleu is a conserved gene involved in neural tube formation: Developmental Biology, v. 262, p. 16-31.

Chen, J. L., K. L. Walton, C. E. Winbanks, K. T. Murphy, R. E. Thomson, Y. Makanji, H. Qian, G. S. Lynch, C. A. Harrison, and P. Gregorevic, 2014, Elevated expression of activins promotes muscle wasting and cachexia: Faseb j, v. 28, p. 1711-23.

Christe, M., N. Jin, X. Wang, K. E. Gould, P. W. Iversen, X. Yu, J. N. Lorenz, V. Kadambi, S. H. Zuckerman, and L. J. Bloem, 2004, Transgenic mice with cardiac-specific over-expression of MLK7 have increased mortality when exposed to chronic beta-adrenergic stimulation: J Mol Cell Cardiol, v. 37, p. 705-15.

Chu, M., C. C. Gregorio, and C. T. Pappas, 2016, Nebulin, a multi-functional giant: J Exp Biol, v. 219, p. 146-52.

Cieplak, M., and J. I. Sulkowska, 2005, Thermal unfolding of proteins: J Chem Phys, v. 123, p. 194908.

Constantin, B., N. Imbert, C. Besse, C. Cognard, and G. Raymond, 1995, Cultured rat skeletal muscle cells treated with cytochalasin exhibit normal dystrophin expression and intracellular free calcium control: Biol Cell, v. 85, p. 125-35.

Costes, S. V., D. Daelemans, E. H. Cho, Z. Dobbin, G. Pavlakis, and S. Lockett, 2004, Automatic and quantitative measurement of protein-protein colocalization in live cells: Biophys J, v. 86, p. 3993-4003.

Cuenda, A., and S. Rousseau, 2007, p38 MAP-kinases pathway regulation, function and role in human diseases: Biochim Biophys Acta, v. 1773, p. 1358-75.

Deng, S., M. Azevedo, and M. Baylies, 2017, Acting on identity: Myoblast fusion and the formation of the syncytial muscle fiber: Semin Cell Dev Biol, v. 72, p. 45-55.

Desler, M. M., S. J. Jones, C. W. Smith, and T. L. Woods, 1996, Effects of dexamethasone and anabolic agents on proliferation and protein

synthesis and degradation in C2C12 myogenic cells: J Anim Sci, v. 74, p. 1265-73.

Dhawan, J., and D. M. Helfman, 2004, Modulation of acto-myosin contractility in skeletal muscle myoblasts uncouples growth arrest from differentiation: Journal of Cell Science, v. 117, p. 3735-3748.

Dickinson, A. G., and V. M. Meikle, 1973, Genetic kyphoscoliosis in mice: Lancet, v. 1, p. 1186.

Duan, R., and P. J. Gallagher, 2009, Dependence of myoblast fusion on a cortical actin wall and nonmuscle myosin IIA: Developmental biology, v. 325, p. 374-385.

Dworak, H. A., M. A. Charles, L. B. Pellerano, and H. Sink, 2001, Characterization of Drosophila hibris, a gene related to human nephrin: Development, v. 128, p. 4265-76.

Dyson, H. J., and P. E. Wright, 2005, Intrinsically unstructured proteins and their functions: Nature Reviews Molecular Cell Biology, v. 6, p. 197-208.

Elkina, Y., S. von Haehling, S. D. Anker, and J. Springer, 2011, The role of myostatin in muscle wasting: an overview: J Cachexia Sarcopenia Muscle, v. 2, p. 143-151.

Evans, W. J., 1999, Exercise training guidelines for the elderly: Med Sci Sports Exerc, v. 31, p. 12-7.

Faggioni, R., A. Moser, K. R. Feingold, and C. Grunfeld, 2000, Reduced leptin levels in starvation increase susceptibility to endotoxic shock: Am J Pathol, v. 156, p. 1781-7.

Fisher, T. E., A. F. Oberhauser, M. Carrion-Vazquez, P. E. Marszalek, and J. M. Fernandez, 1999, The study of protein mechanics with the atomic force microscope: Trends Biochem Sci, v. 24, p. 379-84.

Froger, A., and J. E. Hall, 2007, Transformation of plasmid DNA into E. coli using the heat shock method: J Vis Exp, p. 253.

Gautel, M., 2011, The sarcomeric cytoskeleton: who picks up the strain?: Current Opinion in Cell Biology, v. 23, p. 39-46.

Gildor, B., R. Massarwa, B. Z. Shilo, and E. D. Schejter, 2009, The SCAR and WASp nucleation-promoting factors act sequentially to mediate Drosophila myoblast fusion: EMBO Rep, v. 10, p. 1043-50.

Goodman, C. A., M. H. Miu, J. W. Frey, D. M. Mabrey, H. C. Lincoln, Y. Ge, J. Chen, and T. A. Hornberger, 2010, A phosphatidylinositol 3-kinase/protein kinase B-independent activation of mammalian target of rapamycin signaling is sufficient to induce skeletal muscle hypertrophy: Mol Biol Cell, v. 21, p. 3258-68.

Gossen, M., and H. Bujard, 1992, Tight control of gene expression in mammalian cells by tetracycline-responsive promoters: Proc Natl Acad Sci U S A, v. 89, p. 5547-51.

Gotoh, I., M. Adachi, and E. Nishida, 2001, Identification and characterization of a novel MAP kinase kinase kinase, MLTK: J Biol Chem, v. 276, p. 4276-86.

Grega-Larson, N. E., S. W. Crawley, A. L. Erwin, and M. J. Tyska, 2015, Cordon bleu promotes the assembly of brush border microvilli: American Society for Cell Biology, v. 26, p. 3803-3815.

Guerriero, V., Jr., and J. R. Florini, 1980, Dexamethasone effects on myoblast proliferation and differentiation: Endocrinology, v. 106, p. 1198-202.

Haag, N., S. Schuler, S. Nietzsche, C. A. Hubner, N. Strenzke, B. Qualmann, and M. M. Kessels, 2018, The Actin Nucleator Cobl Is Critical for Centriolar Positioning, Postnatal Planar Cell Polarity Refinement, and Function of the Cochlea: Cell Rep, v. 24, p. 2418-2431.e6.

Haag, N., L. Schwintzer, R. Ahuja, N. Koch, J. Grimm, H. Heuer, B. Qualmann, and M. M. Kessels, 2012, The actin nucleator Cobl is crucial for Purkinje cell development and works in close conjunction with the F-actin binding protein Abp1: J Neurosci, v. 32, p. 17842-56.

Hamoud, N., V. Tran, L. P. Croteau, A. Kania, and J. F. Cote, 2014, G-protein coupled receptor BAI3 promotes myoblast fusion in vertebrates: Proc Natl Acad Sci U S A, v. 111, p. 3745-50.

Han, D. S., W. S. Yang, and T. W. Kao, 2017, Dexamethasone Treatment at the Myoblast Stage Enhanced C2C12 Myocyte Differentiation, Int J Med Sci, v. 14, p. 434-43.

Hara, K., K. Yonezawa, M. T. Kozlowski, T. Sugimoto, K. Andrabi, Q. P. Weng, M. Kasuga, I. Nishimoto, and J. Avruch, 1997, Regulation of eIF-4E BP1 phosphorylation by mTOR: J Biol Chem, v. 272, p. 26457-63.

Hara, K., K. Yonezawa, Q. P. Weng, M. T. Kozlowski, C. Belham, and J. Avruch, 1998, Amino acid sufficiency and mTOR regulate p70 S6 kinase and eIF-4E BP1 through a common effector mechanism: J Biol Chem, v. 273, p. 14484-94.

Hedberg-Oldfors, C., N. Darin, M. Olsson Engman, Z. Orfanos, C. Thomsen, P. F. van der Ven, and A. Oldfors, 2016, A new early-onset neuromuscular disorder associated with kyphoscoliosis peptidase (KY) deficiency: Eur J Hum Genet, v. 24, p. 1771-1777.

Hershko, A., and A. Ciechanover, 1998, The ubiquitin system: Annu Rev Biochem, v. 67, p. 425-79.

Hochreiter-Hufford, A. E., C. S. Lee, J. M. Kinchen, J. D. Sokolowski, S. Arandjelovic, J. A. Call, A. L. Klibanov, Z. Yan, J. W. Mandell, and K. S. Ravichandran, 2013, Phosphatidylserine receptor BAI1 and apoptotic cells as new promoters of myoblast fusion: Nature, v. 497, p. 263-7.

Hoffman, E. P., R. H. Brown, Jr., and L. M. Kunkel, 1987, Dystrophin: the protein product of the Duchenne muscular dystrophy locus: Cell, v. 51, p. 919-28.

Hollnagel, A., C. Grund, W. W. Franke, and H.-H. Arnold, 2002, The Cell Adhesion Molecule M-Cadherin Is Not Essential for Muscle Development and Regeneration: Molecular and Cellular Biology, v. 22, p. 4760-4770.

Hornberger, T. A., R. Stuppard, K. E. Conley, M. J. Fedele, M. L. Fiorotto, E. R. Chin, and K. A. Esser, 2004, Mechanical stimuli regulate rapamycin-sensitive signalling by a phosphoinositide 3-kinase-, protein kinase B- and growth factor-independent mechanism: Biochem J, v. 380, p. 795-804.

Huang, C. Y., P. J. Chueh, C. T. Tseng, K. Y. Liu, H. Y. Tsai, W. W. Kuo, M. Y. Chou, and J. J. Yang, 2004, ZAK re-programs atrial natriuretic factor

expression and induces hypertrophic growth in H9c2 cardiomyoblast cells: Biochem Biophys Res Commun, v. 324, p. 973-80.

Husson, C., L. Renault, D. Didry, D. Pantaloni, and M. F. Carlier, 2011, Cordon-Bleu uses WH2 domains as multifunctional dynamizers of actin filament assembly: Mol Cell, v. 43, p. 464-77.

Huxley, A. F., 1957, Muscle structure and theories of contraction: Prog Biophys Biophys Chem, v. 7, p. 255-318.

Ibarra, N., A. Pollitt, and R. H. Insall, 2005, Regulation of actin assembly by SCAR/WAVE proteins: Biochem Soc Trans, v. 33, p. 1243-6.

Inoki, K., Y. Li, T. Zhu, J. Wu, and K. L. Guan, 2002, TSC2 is phosphorylated and inhibited by Akt and suppresses mTOR signalling: Nat Cell Biol, v. 4, p. 648-57.

Jagoe, R. T., S. H. Lecker, M. Gomes, and A. L. Goldberg, 2002, Patterns of gene expression in atrophying skeletal muscles: response to food deprivation: Faseb j, v. 16, p. 1697-712.

Jokl, E. J., G. L. Hughes, T. Cracknell, M. E. Pownall, and G. Blanco, 2018, Transcriptional upregulation of Bag3, a chaperone-assisted selective autophagy factor, in animal models of KY-deficient hereditary myopathy: Dis Model Mech, v. 11.

Keren, A., Y. Tamir, and E. Bengal, 2006, The p38 MAPK signaling pathway: a major regulator of skeletal muscle development: Mol Cell Endocrinol, v. 252, p. 224-30.

Kesper, D. A., C. Stute, D. Buttgereit, N. Kreisköther, S. Vishnu, K.-F. Fischbach, and R. Renkawitz-Pohl, 2007, Myoblast fusion in Drosophila melanogaster is mediated through a fusion-restricted myogenic-adhesive structure (FuRMAS): Developmental Dynamics, v. 236, p. 404-415.

Kim, J., K. J. Won, H. M. Lee, B. Y. Hwang, Y. M. Bae, W. S. Choi, H. Song, K. W. Lim, C. K. Lee, and B. Kim, 2009, p38 MAPK Participates in Muscle-Specific RING Finger 1-Mediated Atrophy in Cast-Immobilized Rat Gastrocnemius Muscle: Korean J Physiol Pharmacol, v. 13, p. 491-6.

Kim, S., K. Shilagardi, S. Zhang, S. N. Hong, K. L. Sens, J. Bo, G. A. Gonzalez, and E. H. Chen, 2007, A Critical Function for the Actin Cytoskeleton in Targeted Exocytosis of Prefusion Vesicles during Myoblast Fusion: Developmental Cell, v. 12, p. 571-586.

Kimball, S. R., L. M. Shantz, R. L. Horetsky, and L. S. Jefferson, 1999, Leucine regulates translation of specific mRNAs in L6 myoblasts through mTOR-mediated changes in availability of eIF4E and phosphorylation of ribosomal protein S6: J Biol Chem, v. 274, p. 11647-52.

Ko, G. J., Y. Obi, A. R. Tortoricci, and K. Kalantar-Zadeh, 2017, Dietary Protein Intake and Chronic Kidney Disease: Curr Opin Clin Nutr Metab Care, v. 20, p. 77-85.

Kruger, M., and S. Kotter, 2016, Titin, a Central Mediator for Hypertrophic Signaling, Exercise-Induced Mechanosignaling and Skeletal Muscle Remodeling: Front Physiol, v. 7, p. 76.

Laemmli, U. K., 1970, Cleavage of structural proteins during the assembly of the head of bacteriophage T4: Nature, v. 227, p. 680-5.

Lange, S., M. Himmel, D. Auerbach, I. Agarkova, K. Hayess, D. O. Furst, J. C. Perriard, and E. Ehler, 2005, Dimerisation of myomesin: implications for the structure of the sarcomeric M-band: J Mol Biol, v. 345, p. 289-98.

Laurin, M., N. Fradet, A. Blangy, A. Hall, K. Vuori, and J. F. Cote, 2008, The atypical Rac activator Dock180 (Dock1) regulates myoblast fusion in vivo: Proc Natl Acad Sci U S A, v. 105, p. 15446-51.

Lee, S. W., G. Dai, Z. Hu, X. Wang, J. Du, and W. E. Mitch, 2004, Regulation of muscle protein degradation: coordinated control of apoptotic and ubiquitin-proteasome systems by phosphatidylinositol 3 kinase: J Am Soc Nephrol, v. 15, p. 1537-45.

Li, X., 2016, Exploring the function of IGFN1 and MLTK in skeletal muscle, University of York.

Li, X., J. Baker, T. Cracknell, A. R. Haynes, and G. Blanco, 2017, IGFN1_v1 is required for myoblast fusion and differentiation: PLOS ONE.

Li, Y. P., Y. Chen, J. John, J. Moylan, B. Jin, D. L. Mann, and M. B. Reid, 2005, TNF-alpha acts via p38 MAPK to stimulate expression of the ubiquitin ligase atrogin1/MAFbx in skeletal muscle: Faseb j, v. 19, p. 362-70.

Liu, P., Q. Hao, S. Hai, H. Wang, L. Cao, and B. Dong, 2017, Sarcopenia as a predictor of all-cause mortality among community-dwelling older people: A systematic review and meta-analysis: Maturitas, v. 103, p. 16-22.

Livak, K. J., and T. D. Schmittgen, 2001, Analysis of relative gene expression data using real-time quantitative PCR and the 2(-Delta Delta C(T)) Method: Methods, v. 25, p. 402-8.

Malhotra, A., 2009, Tagging for protein expression: Methods Enzymol, v. 463, p. 239-58.

Mansilla, F., C. A. G. Dominguez, J. E. Yeadon, T. J. Corydon, S. J. Burden, and C. R. Knudsen, 2008, Translation Elongation Factor eEF1A Binds to a Novel Myosin Binding Protein-C-Like Protein: Journal of cellular biochemistry, v. 105, p. 847-858.

Marechal, G., G. R. Coulton, and G. Beckers-Bleukx, 1995, Mechanical power and myosin composition of soleus and extensor digitorum longus muscles of ky mice: Am J Physiol, v. 268, p. C513-9.

Mathews, L. S., G. Norstedt, and R. D. Palmiter, 1986, Regulation of insulin-like growth factor I gene expression by growth hormone: Proc Natl Acad Sci U S A, v. 83, p. 9343-7.

McPherron, A. C., A. M. Lawler, and S. J. Lee, 1997, Regulation of skeletal muscle mass in mice by a new TGF-beta superfamily member: Nature, v. 387, p. 83-90.

McPherron, A. C., and S.-J. Lee, 1997, Double muscling in cattle due to mutations in the myostatin gene: Proceedings of the National Academy of Sciences, v. 94, p. 12457-12461.

Menconi, M., P. Gonnella, V. Petkova, S. Lecker, and P. O. Hasselgren, 2008, Dexamethasone and corticosterone induce similar, but not identical, muscle wasting responses in cultured L6 and C2C12 myotubes: J Cell Biochem, v. 105, p. 353-64.

Merlie, J. P., and J. R. Sanes, 1985, Concentration of acetylcholine receptor mRNA in synaptic regions of adult muscle fibres: Nature, v. 317, p. 66-8.

Meyer, T. S., and B. L. Lamberts, 1965, Use of coomassie brilliant blue R250 for the electrophoresis of microgram quantities of parotid saliva proteins on acrylamide-gel strips: Biochim Biophys Acta, v. 107, p. 144-5.

Millay, D. P., D. G. Gamage, M. E. Quinn, Y.-L. Min, Y. Mitani, R. Bassel-Duby, and E. N. Olson, 2016, Structure–function analysis of myomaker domains required for myoblast fusion: Proceedings of the National Academy of Sciences, v. 113, p. 2116-2121.

Millay, D. P., J. R. O/'Rourke, L. B. Sutherland, S. Bezprozvannaya, J. M. Shelton, R. Bassel-Duby, and E. N. Olson, 2013, Myomaker is a membrane activator of myoblast fusion and muscle formation: Nature, v. 499, p. 301-305.

Miyazaki, M., J. J. McCarthy, M. J. Fedele, and K. A. Esser, 2011, Early activation of mTORC1 signalling in response to mechanical overload is independent of phosphoinositide 3-kinase/Akt signalling: J Physiol, v. 589, p. 1831-46.

Morgan, J. E., and T. A. Partridge, 2003, Muscle satellite cells: Int J Biochem Cell Biol, v. 35, p. 1151-6.

Murach, K. A., D. A. Englund, E. E. Dupont-Versteegden, J. J. McCarthy, and C. A. Peterson, 2018, Myonuclear Domain Flexibility Challenges Rigid Assumptions on Satellite Cell Contribution to Skeletal Muscle Fiber Hypertrophy: Front Physiol, v. 9, p. 635.

Negrutskii, B. S., and A. V. El'skaya, 1998, Eukaryotic translation elongation factor 1 alpha: structure, expression, functions, and possible role in aminoacyl-tRNA channeling: Prog Nucleic Acid Res Mol Biol, v. 60, p. 47-78.

Nowak, S. J., P. C. Nahirney, A.-K. Hadjantonakis, and M. K. Baylies, 2009, Nap1-mediated actin remodeling is essential for mammalian myoblast fusion: Journal of Cell Science, v. 122, p. 3282-3293.

Ono, S., 2010, Dynamic Regulation of Sarcomeric Actin Filaments in Striated Muscle: Cytoskeleton (Hoboken), v. 67, p. 677-92.

Otey, C. A., R. Dixon, C. Stack, and S. M. Goicoechea, 2009, Cytoplasmic Ig-Domain Proteins: Cytoskeletal Regulators with a Role in Human Disease: Cell Motil Cytoskeleton, v. 66, p. 618-34.

Ott, W., M. A. Jobst, C. Schoeler, H. E. Gaub, and M. A. Nash, 2017, Single-molecule force spectroscopy on polyproteins and receptor-ligand complexes: The current toolbox: J Struct Biol, v. 197, p. 3-12.

Parry, D. A., and J. M. Squire, 1973, Structural role of tropomyosin in muscle regulation: analysis of the x-ray diffraction patterns from relaxed and contracting muscles: J Mol Biol, v. 75, p. 33-55.

Paul, P. K., S. K. Gupta, S. Bhatnagar, S. K. Panguluri, B. G. Darnay, Y. Choi, and A. Kumar, 2010, Targeted ablation of TRAF6 inhibits skeletal muscle wasting in mice: J Cell Biol, v. 191, p. 1395-411.

Pavlath, G. K., K. Rich, S. G. Webster, and H. M. Blau, 1989, Localization of muscle gene products in nuclear domains: Nature, v. 337, p. 570-3.

Pedersen, B. K., 2013, Muscle as a secretory organ: Compr Physiol, v. 3, p. 1337-62.

Pellegrino, C., and C. Franzini, 1963, AN ELECTRON MICROSCOPE STUDY OF DENERVATION ATROPHY IN RED AND WHITE SKELETAL MUSCLE FIBERS: The Journal of Cell Biology, v. 17, p. 327-349.

Politou, A. S., D. J. Thomas, and A. Pastore, 1995, The folding and stability of titin immunoglobulin-like modules, with implications for the mechanism of elasticity: Biophys J, v. 69, p. 2601-10.

Qin, J., R. Du, Y.-Q. Yang, H.-Q. Zhang, Q. Li, L. Liu, H. Guan, J. Hou, and X.-R. An, 2013, Dexamethasone-induced skeletal muscle atrophy was associated with upregulation of myostatin promoter activity: Research in Veterinary Science, v. 94, p. 84-89.

Qin, W., J. Pan, Y. Wu, W. A. Bauman, and C. Cardozo, 2010, Protection against dexamethasone-induced muscle atrophy is related to modulation by testosterone of FOXO1 and PGC-1alpha: Biochem Biophys Res Commun, v. 403, p. 473-8.

Quinn, M. E., Q. Goh, M. Kurosaka, D. G. Gamage, M. J. Petrany, V. Prasad, and D. P. Millay, 2017, Myomerger induces fusion of non-fusogenic cells and is required for skeletal muscle development: Nature Communications, v. 8, p. 15665.

Radice, G. L., H. Rayburn, H. Matsunami, K. A. Knudsen, M. Takeichi, and R. O. Hynes, 1997, Developmental Defects in Mouse Embryos Lacking N-Cadherin: Developmental Biology, v. 181, p. 64-78.

Raffaello, A., G. Milan, E. Masiero, S. Carnio, D. Lee, G. Lanfranchi, A. L. Goldberg, and M. Sandri, 2010, JunB transcription factor maintains skeletal muscle mass and promotes hypertrophy: J Cell Biol, v. 191, p. 101-13.

Rahimov, F., O. D. King, L. C. Warsing, R. E. Powell, C. P. Emerson, Jr., L. M. Kunkel, and K. R. Wagner, 2011, Gene expression profiling of skeletal muscles treated with a soluble activin type IIB receptor: Physiol Genomics, v. 43, p. 398-407.

Ravenscroft, G., R. J. Bryson-Richardson, K. J. Nowak, and N. G. Laing, 2018, Recent advances in understanding congenital myopathies: F1000Res, v. 7.

Rebbapragada, A., H. Benchabane, J. L. Wrana, A. J. Celeste, and L. Attisano, 2003, Myostatin Signals through a Transforming Growth Factor β-Like Signaling Pathway To Block Adipogenesis: Molecular and Cellular Biology, v. 23, p. 7230-7242.

Renshaw, S., 2016, Immunohistochemistry and Immunocytochemistry: Essential Methods.

Richardson, B. E., K. Beckett, S. J. Nowak, and M. K. Baylies, 2007, SCAR/WAVE and Arp2/3 are crucial for cytoskeletal remodeling at the site of myoblast fusion: Development, v. 134, p. 4357-67.

Rief, M., M. Gautel, F. Oesterhelt, J. M. Fernandez, and H. E. Gaub, 1997, Reversible Unfolding of Individual Titin Immunoglobulin Domains by AFM.

Rio, D. C., M. Ares, Jr., G. J. Hannon, and T. W. Nilsen, 2010, Purification of RNA using TRIzol (TRI reagent): Cold Spring Harb Protoc, v. 2010, p. pdb.prot5439.

Rochlin, K., S. Yu, S. Roy, and M. K. Baylies, 2010, Myoblast fusion: when it takes more to make one: Dev Biol, v. 341, p. 66-83.

Rodriguez, L. G., X. Wu, and J. L. Guan, 2005, Wound-healing assay: Methods Mol Biol, v. 294, p. 23-9.

Rommel, C., S. C. Bodine, B. A. Clarke, R. Rossman, L. Nunez, T. N. Stitt, G. D. Yancopoulos, and D. J. Glass, 2001, Mediation of IGF-1-induced skeletal myotube hypertrophy by PI(3)K/Akt/mTOR and PI(3)K/Akt/GSK3 pathways: Nat Cell Biol, v. 3, p. 1009-13.

Ruiz-Gomez, M., N. Coutts, A. Price, M. V. Taylor, and M. Bate, 2000, Drosophila dumbfounded: a myoblast attractant essential for fusion: Cell, v. 102, p. 189-98.

Sanderova, H., M. Hulkova, P. Malon, M. Kepkova, and J. Jonak, 2004, Thermostability of multidomain proteins: elongation factors EF-Tu from Escherichia coli and Bacillus stearothermophilus and their chimeric forms: Protein Sci, v. 13, p. 89-99.

Sandri, M., C. Sandri, A. Gilbert, C. Skurk, E. Calabria, A. Picard, K. Walsh, S. Schiaffino, S. H. Lecker, and A. L. Goldberg, 2004, Foxo transcription factors induce the atrophy-related ubiquitin ligase atrogin-1 and cause skeletal muscle atrophy: Cell, v. 117, p. 399-412.

Sanger, J. W., and H. Holtzer, 1972, Cytochalasin B: effects on cell morphology, cell adhesion, and mucopolysaccharide synthesis (cultured cells-contractile microfilaments-glycoproteins-embryonic cells-sorting-out): Proc Natl Acad Sci U S A, v. 69, p. 253-7.

Schoenauer, R., P. Bertoncini, G. Machaidze, U. Aebi, J.-C. Perriard, M. Hegner, and I. Agarkova, 2005, Myomesin is a Molecular Spring with Adaptable Elasticity: Journal of Molecular Biology, v. 349, p. 367-379.

Schuelke, M., K. R. Wagner, L. E. Stolz, C. Hubner, T. Riebel, W. Komen, T. Braun, J. F. Tobin, and S. J. Lee, 2004, Myostatin mutation associated with gross muscle hypertrophy in a child: N Engl J Med, v. 350, p. 2682-8.

Schuler, S., J. Hauptmann, B. Perner, M. M. Kessels, C. Englert, and B. Qualmann, 2013, Ciliated sensory hair cell formation and function require the F-BAR protein syndapin I and the WH2 domain-based actin nucleator Cobl: J Cell Sci, v. 126, p. 196-208.

Schwander, M., M. Leu, M. Stumm, O. M. Dorchies, U. T. Ruegg, J. Schittny, and U. Muller, 2003, Beta1 integrins regulate myoblast fusion and sarcomere assembly: Dev Cell, v. 4, p. 673-85.

Segalés, J., E. Perdiguero, and P. Muñoz-Cánoves, 2016, Regulation of Muscle Stem Cell Functions: A Focus on the p38 MAPK Signaling Pathway: Front Cell Dev Biol, v. 4.

Shi, J., P. Bi, J. Pei, H. Li, N. V. Grishin, R. Bassel-Duby, E. H. Chen, and E. N. Olson, 2017, Requirement of the fusogenic micropeptide myomixer for muscle formation in zebrafish: Proc Natl Acad Sci U S A, v. 114, p. 11950-11955.

Shilagardi, K., S. Li, F. Luo, F. Marikar, R. Duan, P. Jin, J. H. Kim, K. Murnen, and E. H. Chen, 2013, Actin-propelled invasive membrane protrusions promote fusogenic protein engagement during cell-cell fusion: Science, v. 340, p. 359-63.

Sohn, R. L., P. Huang, G. Kawahara, M. Mitchell, J. Guyon, R. Kalluri, L. M. Kunkel, and E. Gussoni, 2009, A role for nephrin, a renal protein, in vertebrate skeletal muscle cell fusion: Proceedings of the National Academy of Sciences of the United States of America, v. 106, p. 9274-9279.

Spangenburg, E. E., D. Le Roith, C. W. Ward, and S. C. Bodine, 2008, A functional insulin-like growth factor receptor is not necessary for load-induced skeletal muscle hypertrophy: J Physiol, v. 586, p. 283-91.

Spielmann, M., N. Kakar, N. Tayebi, C. Leettola, G. Nurnberg, N. Sowada, D. G. Lupianez, I. Harabula, R. Flottmann, D. Horn, W. L. Chan, L. Wittler, R. Yilmaz, J. Altmuller, H. Thiele, H. van Bokhoven, C. E. Schwartz, P. Nurnberg, J. U. Bowie, J. Ahmad, C. Kubisch, S. Mundlos, and G. Borck, 2016, Exome sequencing and CRISPR/Cas genome editing identify mutations of ZAK as a cause of limb defects in humans and mice: Genome Res, v. 26, p. 183-91.

Stedman, H. H., H. L. Sweeney, J. B. Shrager, H. C. Maguire, R. A. Panettieri, B. Petrof, M. Narusawa, J. M. Leferovich, J. T. Sladky, and A. M. Kelly, 1991, The mdx mouse diaphragm reproduces the degenerative changes of Duchenne muscular dystrophy: Nature, v. 352, p. 536-9.

Stitt, T. N., D. Drujan, B. A. Clarke, F. Panaro, Y. Timofeyva, W. O. Kline, M. Gonzalez, G. D. Yancopoulos, and D. J. Glass, 2004, The IGF-1/PI3K/Akt Pathway Prevents Expression of Muscle Atrophy-Induced Ubiquitin Ligases by Inhibiting FOXO Transcription Factors: Molecular Cell, v. 14, p. 395-403.

Straussberg, R., G. Schottmann, M. Sadeh, E. Gill, F. Seifert, A. Halevy, K. Qassem, J. Rendu, P. F. van der Ven, W. Stenzel, and M. Schuelke, 2016, Kyphoscoliosis peptidase (KY) mutation causes a novel congenital myopathy with core targetoid defects, Acta Neuropathol, v. 132: Germany, p. 475-8.

Strunkelnberg, M., B. Bonengel, L. M. Moda, A. Hertenstein, H. G. de Couet, R. G. Ramos, and K. F. Fischbach, 2001, rst and its paralogue kirre act redundantly during embryonic muscle development in Drosophila: Development, v. 128, p. 4229-39.

Szklarczyk, D., A. Franceschini, S. Wyder, K. Forslund, D. Heller, J. Huerta-Cepas, M. Simonovic, A. Roth, A. Santos, K. P. Tsafou, M. Kuhn, P. Bork, L. J. Jensen, and C. von Mering, 2015, STRING v10: protein-protein interaction networks, integrated over the tree of life: Nucleic Acids Res, v. 43, p. D447-52.

Tawa, N. E., Jr., R. Odessey, and A. L. Goldberg, 1997, Inhibitors of the proteasome reduce the accelerated proteolysis in atrophying rat skeletal muscles: J Clin Invest, v. 100, p. 197-203.

Titomirov, A. V., S. Sukharev, and E. Kistanova, 1991, In vivo electroporation and stable transformation of skin cells of newborn mice by plasmid DNA: Biochim Biophys Acta, v. 1088, p. 131-4.

Towbin, H., T. Staehelin, and J. Gordon, 1979, Electrophoretic transfer of proteins from polyacrylamide gels to nitrocellulose sheets: procedure and some applications: Proc Natl Acad Sci U S A, v. 76, p. 4350-4.

Tsekoura, M., A. Kastrinis, M. Katsoulaki, E. Billis, and J. Gliatis, 2017, Sarcopenia and Its Impact on Quality of Life: Adv Exp Med Biol, v. 987, p. 213-218.

Tskhovrebova, L., and J. Trinick, 2003, Titin: properties and family relationships: Nat Rev Mol Cell Biol, v. 4, p. 679-89.

Tsuchida, K., 2008, Targeting myostatin for therapies against muscle-wasting disorders: Curr Opin Drug Discov Devel, v. 11, p. 487-94.

Ulbricht, A., Felix J. Eppler, Victor E. Tapia, Peter F. M. van der Ven, N. Hampe, N. Hersch, P. Vakeel, D. Stadel, A. Haas, P. Saftig, C. Behrends, Dieter O. Fürst, R. Volkmer, B. Hoffmann, W. Kolanus, and J. Höhfeld, 2013, Cellular Mechanotransduction Relies on Tension-Induced and Chaperone-Assisted Autophagy: Current Biology, v. 23, p. 430-435.

Ulbricht, A., S. Gehlert, B. Leciejewski, T. Schiffer, W. Bloch, and J. Hohfeld, 2015, Induction and adaptation of chaperone-assisted selective autophagy CASA in response to resistance exercise in human skeletal muscle: Autophagy, v. 11, p. 538-46.

van der Pijl, R., J. Strom, S. Conijn, J. Lindqvist, S. Labeit, H. Granzier, and C. Ottenheijm, 2018, Titin-based mechanosensing modulates muscle hypertrophy: J Cachexia Sarcopenia Muscle, v. 9, p. 947-961.

Vasli, N., E. Harris, J. Karamchandani, E. Bareke, J. Majewski, N. B. Romero, T. Stojkovic, R. Barresi, H. Tasfaout, R. Charlton, E. Malfatti, J. Bohm, C. Marini-Bettolo, K. Choquet, M. J. Dicaire, Y. H. Shao, A. Topf, E. O'Ferrall, B. Eymard, V. Straub, G. Blanco, H. Lochmüller, B. Brais, J. Laporte, and M. Tétreault, 2017, Recessive mutations in the kinase ZAK cause a congenital myopathy with fibre type disproportion, Brain, v. 140, p. 37-48.

Vasyutina, E., B. Martarelli, C. Brakebusch, H. Wende, and C. Birchmeier, 2009, The small G-proteins Rac1 and Cdc42 are essential for myoblast fusion in the mouse: Proc Natl Acad Sci U S A, v. 106, p. 8935-40.

Velloso, C. P., 2008, Regulation of muscle mass by growth hormone and IGF-I: Br J Pharmacol, v. 154, p. 557-68.

Wayt, J., and A. Bretscher, 2014, Cordon Bleu serves as a platform at the basal region of microvilli, where it regulates microvillar length through its WH2 domains: Mol Biol Cell, v. 25, p. 2817-27.

Weinberg, E. S., M. L. Allende, C. S. Kelly, A. Abdelhamid, T. Murakami, P. Andermann, O. G. Doerre, D. J. Grunwald, and B. Riggleman, 1996, Developmental regulation of zebrafish MyoD in wild-type, no tail and spadetail embryos: Development, v. 122, p. 271-80.

Wilkins, J. T., L. S. Krivickas, R. Goldstein, D. Suh, and W. R. Frontera, 2001, Contractile properties of adjacent segments of single human muscle fibers: Muscle and Nerve, v. 24, p. 1319-1326.

Witt, C. C., C. Burkart, D. Labeit, M. McNabb, Y. Wu, H. Granzier, and S. Labeit, 2006, Nebulin regulates thin filament length, contractility, and Z-disk structure in vivo, EMBO J, v. 25, p. 3843-55.

Xu, L., P. Zhao, A. Mariano, and R. Han, 2013, Targeted Myostatin Gene Editing in Multiple Mammalian Species Directed by a Single Pair of TALE Nucleases: Mol Ther Nucleic Acids, v. 2, p. e112.

Yaffe, D., and O. Saxel, 1977, Serial passaging and differentiation of myogenic cells isolated from dystrophic mouse muscle: Nature, v. 270, p. 725-7.

Yogev, Y., Y. Perez, I. Noyman, A. A. Madegem, H. Flusser, Z. Shorer, E. Cohen, L. Kachko, A. Michaelovsky, R. Birk, A. Koifman, M. Drabkin, O. Wormser, D. Halperin, R. Kadir, and O. S. Birk, 2017, Progressive hereditary spastic paraplegia caused by a homozygous KY mutation: Eur J Hum Genet, v. 25, p. 966-972.

Zhang, Q., A. A. Vashisht, J. O'Rourke, S. Y. Corbel, R. Moran, A. Romero, L. Miraglia, J. Zhang, E. Durrant, C. Schmedt, and S. C. Sampath, 2017, The microprotein Minion controls cell fusion and muscle formation: Nat Commun, v. 8, p. 15664.